Waveguide approach to plasmonic antennas

Dissertation

zur Erlangung des akademischen Grades

doctor rerum naturalium (Dr. rer. nat.)

vorgelegt dem Rat der Physikalisch-Astronomischen Fakultät

der Friedrich-Schiller-Universität Jena

von Msc. Applied Physics Shakeeb Bin Hasan
geboren am 04.08.1983 in Karachi, Pakistan

1. Gutachter: Prof. Dr. rer. nat. habil. Falk Lederer, Friedrich-Schiller-Universität Jena, Germany

2. Gutachter: Prof. Dr. rer. nat. Stefan Linden, Universität Bonn, Germany

3. Gutachter: Prof. Dr. Jari Turunen, University of Eastern Finland, Finland

Tag der Disputation: 10. 06. 2014

Contents

1 Introduction **3**

2 Analytical framework **6**

2.1 Maxwell's equations 6
2.2 Reciprocity relations 8
2.3 Mode orthogonality 10
2.4 Modal impedance 12
2.5 Coupled mode theory 17
2.6 Surface Plasmon Polaritons 26
  2.6.1 Propagating SPP 26
  2.6.2 Localized SPP 31
2.7 Concluding remarks 35

3 Antenna description of localized plasmonic resonances **36**

3.1 Introduction 36
3.2 Fabry-Perot model 38
3.3 Sphere 39
3.4 Core-shell 44
3.5 Ellipsoid 47
3.6 Cylinder 48
3.7 Composite particle 51
3.8 Concluding remarks 54

4 Nonlinear response of cylindrical antennas **56**

4.1 Introduction 56
4.2 Antenna design consideration 58
4.3 Linear response 59
4.4 Tuning the resonances 62
4.5 Nonlinear response 64

4.6 Other example: Core-shell antenna 69
4.7 Concluding remarks 71

5 Nonlinear interaction in slot waveguides 72
5.1 Introduction 72
5.2 Modes in slot waveguides 74
5.3 Coupled mode theory 79
5.4 Numerical results 81
5.4.1 Phase-mismatch 82
5.4.2 Mode overlap 82
5.4.3 Parametric Amplification 88
5.5 Concluding remarks 91

6 Summary and outlook 92

Zusammenfassung i

Publications iii
Peer-reviewed Journals iii
Conference Papers iv
Invited Talks iv
Conference Contributions iv

Bibliography vi

Acknowledgments xxi

Short Curriculum Vitae xxiii
Personal Data xxiii
Academic Career xxiii
Lectures Conducted xxiii
Education xxiii

Ehrenwörtliche Erklärung xxiv

1 Introduction

The quest to realize functional optical elements at ever decreasing length scales and a parallel development of advanced fabrication techniques have resurrected surface plasmon polaritons (SPP) from the archives of research literature. SPP, in short, refers to the coupled oscillation of electrons with the incoming radiation at a metal-dielectric interface [1,2]. Although the principles of waveguiding and focusing are well-established in dielectric systems, they invariably suffer from the problem of diffraction limit which forbids the localization of light to a scale smaller than half-wavelength in the medium [3]. With metallic structures exhibiting SPP, however, it is possible to go far beyond that limit to truly localize light at sub-wavelength scales [4–6]. As waveguiding geometries, they support guided surface waves which evanescently decay across the metal-dielectric interface [1, 2]. This allows them to propagate while being confined at a scale much smaller than the wavelength of light in dielectric medium. Likewise, plasmonic particles such as spheres act as light localizing antennas at resonance [6–9]. Within the realms of classical electrodynamics, their size can be shrunk to as low as tens of nano meters thereby providing plasmonic focusing elements which converge light to spot size much smaller than what can ordinarily be achieved by diffraction limited microscopes. Furthermore, the high near fields necessarily associated with plasmonic resonances and modes serve additional purpose of enhancing nonlinearities that exist in metal and dielectric media [10–12].

This has stimulated an ever-increasing quest into discovering novel plasmonic systems and characterizing their response. Plasmonic waveguides, for instance, have been subjected to intensive theoretical and experimental studies (for instance Refs. [13–18]). Departing from the simplest single metal-dielectric interface, SPPs guided by thin metallic (dielectric) films sandwiched between dielectric (metallic) media have been extensively explored for their linear and nonlinear response [19–25]. This involves constructing more complicated and versatile structures for confining light in plasmonic waveguides [17, 26–30], identifying efficient coupling schemes [31–37], directional couplers for integrated plasmonics [38–41], nano-focusing the guided light to achieve high intensities at the focus [39, 42–46], and even materializing effects such as negative mode index in plasmonic waveguides [47–51].

As to the resonant focusing of light by plasmonic particles, this goes even further back to 1908 when Gustav Mie proposed a rigorous solution to the problem of scattering of light by spheres [7]. Mie solution is further adapted to account for other geometries like ellipsoids and cylinders [8]. The scattering properties of these structures have now been further customized by arranging them in the form of dimers [52, 53], trimers [54, 55] and so on and so forth [56, 57]. Besides plasmonic particles, extended metallic antennas constructed on the scale of tens to hundreds of nano-meters also exhibit localized plasmonic resonances. Their working principle is phenomenologically understood, much like antennas in radio frequency, as the interference effects of propagating SPP modes in the antenna cavity [58–61]. Both plasmonic particles and antennas form a rich set of tools for manipulating focused light at nano-scale.

In addition to light guiding and focusing, systems based on plasmonic structures have also opened gates to observing a whole new set of sophisticated phenomena. Famous examples include extraordinary optical transmission [62–65], induced magnetic response in metals [66–70], asymmetric transmission [71–75], plasmon induced transparency [76–79], and perfect absorption of light [38, 80–82] to name only a few. Many of these areas have grown into separate topic in their own right.

In this thesis, we present select contributions of our own to the stream of research going on in plasmonics. The work is divided into six chapters including the present one. As necessary introduction is included at the beginning of each chapter, it suffices here to give only a brief mention of what is to follow in the upcoming chapters.

Chapter 2 is dedicated to setting down theoretical constructs and notations which will be required in understanding the contents presented in later chapters. The only exception is the discussion of mode impedance in waveguides which does not constitute the foundation of any further study.

Beginning from Ch. 3, we consider the well-known problem of scattering of light by spheres and other analytical understood particles [8]. However, we cast the geometry now into a new light altogether by visualizing the particles as a special case of extended antennas with terminations drawn from half of the particles under consideration. This naturally brings up the question about the existence of a single physical explanation that accounts for the resonances sustained by such systems. We try to find answer to this question in terms of widely employed phenomenological model for antenna resonances.

Chapter 4 is dedicated to enhancing the nonlinear response of extended plasmonic antennas. The recent trend indicates a growing interest in structures that sustain resonances at multiple or ideally all the frequencies participating in the nonlinear process. This has already led to a few reports proposing sophisticated geometries with unique features that allow their resonances to be desirably engineered to overlap with multiple frequencies involved in the nonlinear interaction [83–86]. Here we consider a rather simple and unsuspected geometry of cylindrical antennas to investigate their potential for achieving the same end without introducing any conceptual design complexity.

In Ch. 5 we present our results for the problem of nonlinear phase mismatch in degenerate second harmonic generation (SHG) [87] in plasmonic slot waveguides. Like any frequency conversion process in waveguides, it is essential to alleviate the phase mismatch that exists between guided modes at fundamental and second harmonics. As an application, we also consider the problem of parametric amplification of a guided SPP mode in slot waveguide. This should be an interesting case because any scheme for compensating plasmonic dissipation can have an enabling effect for further applications involving plasmonic waveguides in integrated optics.

In Ch. 6, we finally summarize all the results and further discuss the possibilities for taking forward the work presented in preceding chapters.

Lastly, it is apt to note here that the title of this treatise derives primarily from the fact that waveguide approach has been adopted in solving all the problems presented in this work, majority of which appertains to plasmonic antennas. The case of slot waveguides considered at in Ch. 5 obviously does not fall into the category of antennas. However, it is included because it carries forward the theme of preceding chapter by exploring the waveguide analogue of multiply-resonant antennas for efficient nonlinear conversion of energy.

2 Analytical framework

Over the course of this treatise, we will be dealing with various forms of modal dynamics in the plasmonic waveguides coming under consideration. In this context, it is instructive to lay down at the very outset the theoretical formalism that shall be employed, at times repeatedly, to both qualitatively and quantitatively understand the evolution of guided modes in waveguiding systems. This would allow an uninhibited flow of ideas in later chapters where we would be able to remain focused on the physical aspects of the problems rather than detouring into the derivation of mathematical formalisms. With this in mind, we lay down the Maxwell's equations in the beginning and derive some necessary relations that will be of use later. Next we derive the reciprocity relation leading to modal orthogonality which constitutes the foundation upon which we can build the more involved treatment of modal dynamics in waveguides. Thereafter we will consider the description of impedance concept in complex waveguides which would be followed with a rigorous formalism to describe the nonlinear interaction of modes in the waveguides. In the end, we will derive equations to describe surface plasmon polaritons (SPP) in the most basic forms i.e. as a wave guided at the interface between metal and dielectric and secondly as a localized resonance of a metallic sphere embedded in a dielectric medium.

2.1 Maxwell's equations

It is pertinent to lay down succinctly at the onset equations governing the behavior of electromagnetic fields in classical electrodynamics. This will serve as a convenient reference point for the derivations to follow in later sections. Given the immense breadth of phenomena that can be described by these equations, we will limit our description only to the point where it remains relevant to the ideas going to be discussed later in this treatise.

We begin with Maxwell's curl and divergence equations which are defined in the absence of source electric charges and currents as [88]

$$\nabla \times \tilde{\mathbf{E}}\left(\mathbf{r},t\right) = -\mu_0 \frac{\partial \tilde{\mathbf{H}}\left(\mathbf{r},t\right)}{\partial t}, \qquad \nabla \times \tilde{\mathbf{H}}\left(\mathbf{r},t\right) = \frac{\partial \tilde{\mathbf{D}}\left(\mathbf{r},t\right)}{\partial t}, \tag{2.1.1}$$

$$\nabla \cdot \tilde{\mathbf{D}}\left(\mathbf{r},t\right) = 0, \qquad \nabla \cdot \tilde{\mathbf{H}}\left(r,t\right) = 0. \tag{2.1.2}$$

In Eqs. (2.1.1) and (2.1.2), $\tilde{\mathbf{E}}\left(\mathbf{r},t\right)$ stands for the electric field, $\tilde{\mathbf{D}}\left(\mathbf{r},t\right)$ the electric displacement and $\tilde{\mathbf{H}}\left(\mathbf{r},t\right)$ the magnetic field. Time dependence of the fields in Eqs. (2.1.1) and (2.1.2) has been signified by means of tilde. It will be dropped for quantities that are time independent (depending solely on spatial domain parameters) or transformed to frequency domain, as we will see later in the chapter. Since we are exclusively concerned with the electromagnetic effects in the visible and infra-red regime, we have ignored any intrinsic magnetic effects in the medium and therefore described the magnetic flux density $\tilde{\mathbf{B}}\left(\mathbf{r},t\right)$ as

$$\tilde{\mathbf{B}}\left(\mathbf{r},t\right) = \mu_0 \tilde{\mathbf{H}}\left(\mathbf{r},t\right).$$

The electric displacement $\tilde{\mathbf{D}}\left(\mathbf{r},t\right)$ depends upon material parameters and the electric field in the medium. In linear regime, it is related to the electric field through its causal dielectric response tensor $\overline{\overline{\tilde{R}}}^{(1)}\left(\mathbf{r},t\right)$ in the following form:

$$\tilde{\mathbf{D}}\left(\mathbf{r},t\right) = \varepsilon_0 \int_{-\infty}^{t} \overline{\overline{\tilde{R}}}^{(1)}\left(\mathbf{r},t-\tau\right) \mathbf{E}\left(\mathbf{r},\tau\right) d\tau. \tag{2.1.3}$$

Taking Fourier transform of Eqs. (2.1.1) and (2.1.2), we get

$$\nabla \times \mathbf{E}\left(\mathbf{r},\nu\right) = \iota 2\pi\nu\mu_0 \mathbf{H}\left(\mathbf{r},\nu\right), \qquad \nabla \times \mathbf{H}\left(\mathbf{r},\nu\right) = -\iota 2\pi\nu \mathbf{D}\left(\mathbf{r},\nu\right) \tag{2.1.4}$$

for the curl equations and

$$\nabla \cdot \mathbf{D}\left(\mathbf{r},\nu\right) = 0, \qquad \nabla \cdot \mathbf{H}\left(\mathbf{r},\nu\right) = 0, \tag{2.1.5}$$

for divergence Equations The Fourier integral and synthesis equations are defined as

$$A\left(\nu\right) = \int_{-\infty}^{\infty} \tilde{A}\left(t\right) \exp\left(\iota 2\pi\nu t\right) dt, \tag{2.1.6}$$

$$\tilde{A}\left(t\right) = \int_{-\infty}^{\infty} A\left(\nu\right) \exp\left(-\iota 2\pi\nu t\right) d\nu. \tag{2.1.7}$$

By means of Fourier convolution theorem [89], the corresponding definition of electric displacement field $\mathbf{D}\left(\mathbf{r},\nu\right)$ now becomes

$$\mathbf{D}\left(\mathbf{r},\nu\right)=\varepsilon_0\overline{\overline{\varepsilon}}_{\mathrm{r}}\left(\mathbf{r},\nu\right)\mathbf{E}\left(\mathbf{r},\nu\right), \tag{2.1.8}$$

where the complex dielectric permittivity tensor of the medium $\overline{\overline{\varepsilon}}_{\mathrm{r}}\left(\mathbf{r},\nu\right)$ is the Fourier domain counterpart of the time domain response of the medium. It is defined as

$$\overline{\overline{\varepsilon}}_{\mathrm{r}}\left(\mathbf{r},\nu\right)=\int_{-\infty}^{\infty}\overline{\overline{\tilde{R}}}^{(1)}\left(\mathbf{r},t\right)\exp\left(\imath 2\pi\nu t\right)dt. \tag{2.1.9}$$

At the interface between two media described by permittivities $\overline{\overline{\varepsilon}}_1\left(\nu\right)$ and $\overline{\overline{\varepsilon}}_2\left(\nu\right)$, it can be shown that Eqs. (2.1.4) and (2.1.5) lead to the following boundary conditions [88]:

$$\left(\mathbf{E}_1-\mathbf{E}_2\right)\times\hat{\mathbf{n}}=0,\qquad\left(\mathbf{D}_1-\mathbf{D}_2\right)\cdot\hat{\mathbf{n}}=0 \tag{2.1.10}$$

for the electric and displacement fields and

$$\left(\mathbf{H}_1-\mathbf{H}_2\right)\times\hat{\mathbf{n}}=0,\qquad\left(\mathbf{B}_1-\mathbf{B}_2\right)\cdot\hat{\mathbf{n}}=0 \tag{2.1.11}$$

for the magnetic and flux fields. In Eqs. (2.1.10) and (2.1.11) above, $\hat{\mathbf{n}}$ is the unit vector normal to the interface between the two media.

2.2 Reciprocity relations

As mentioned above, reciprocity relation serves to be the foundation on which a detailed account of the electromagnetic field dynamics in waveguides can be based. In a general sense, the reciprocity relations are used to establish relationship between a current source and the field it generates at the observation point to the case when the positions of source and observation points are interchanged. A more precise interpretation depends upon the specific formulation of reciprocity relation under consideration (see for instance Ref. [90] for a detailed account). But for our purpose, we will restrict our attention to the application of reciprocity relations in solving the problems of mode orthogonality and nonlinear coupling in waveguides.

Let us consider two sets of electromagnetic fields $\{\mathbf{E}_1\left(\mathbf{r},\nu\right),\mathbf{H}_1\left(\mathbf{r},\nu\right)\}$ and $\{\mathbf{E}_2\left(\mathbf{r},\nu\right),$ $\mathbf{H}_2\left(\mathbf{r},\nu\right)\}$ defined in a medium with complex permittivity $\overline{\overline{\varepsilon}}_{\mathrm{r}}\left(\mathbf{r},\nu\right)$. Each set of fields is subjected to a perturbative polarization $\mathbf{P}_1\left(\mathbf{r},\nu\right)$ and $\mathbf{P}_2\left(\mathbf{r},\nu\right)$ respectively. Accordingly, the electric displacement field in Eq. (2.1.4) becomes

$$\mathbf{D}_{\{1,2\}}\left(\mathbf{r},\nu\right)=\mathbf{D}^{(1)}_{\{1,2\}}\left(\mathbf{r},\nu\right)+\mathbf{P}_{\{1,2\}}\left(\mathbf{r},\nu\right). \tag{2.2.1}$$

The non-perturbative part $\mathbf{D}^{(1)}_{\{1,2\}}(\mathbf{r},\nu)$ of the electric displacement field is defined according to Eq. (2.1.8). For our purpose, the exact nature of the perturbative polarization does not need to be specified here. At this point, it is now possible to obtain two different kinds of results that are usually found in standard literature [91]. These two forms are known as conjugated and unconjugated reciprocity theorem [91]. Although we will need only one, as it shall soon become clear, for the sake of completeness we would consider both here.

Unconjugated reciprocity relation

We begin with deriving the form of reciprocity relation which is going to be relied upon later in the chapter for the analysis of waveguiding systems. We note that our derivation closely follows the one presented earlier but for isotropic media [91]. By using the vector identity

$$\nabla\cdot(\mathbf{A}\times\mathbf{B})=\mathbf{B}\cdot(\nabla\times\mathbf{A})-\mathbf{A}\cdot(\nabla\times\mathbf{B})\,, \tag{2.2.2}$$

we easily obtain the following expression relating the two sets of electromagnetic fields:

$$\begin{aligned}\nabla\cdot\left[\mathbf{E}_1(\mathbf{r},\nu)\times\mathbf{H}_2(\mathbf{r},\nu)-\mathbf{E}_2(\mathbf{r},\nu)\times\mathbf{H}_1(\mathbf{r},\nu)\right]=\;&\iota 2\pi\nu\varepsilon_0\left[\mathbf{E}_1(\mathbf{r},\nu)\cdot\left\{\overline{\overline{\varepsilon}}_\mathrm{r}(\mathbf{r},\nu)\,\mathbf{E}_2(\mathbf{r},\nu)\right\}\right.\\&-\left.\left\{\overline{\overline{\varepsilon}}_\mathrm{r}(\mathbf{r},\nu)\,\mathbf{E}_1(\mathbf{r},\nu)\right\}\cdot\mathbf{E}_2(\mathbf{r},\nu)\right]\\&+\iota 2\pi\nu\left[\mathbf{P}_2(\mathbf{r},\nu)\cdot\mathbf{E}_1(\mathbf{r},\nu)\right.\\&-\left.\mathbf{P}_1(\mathbf{r},\nu)\cdot\mathbf{E}_2(\mathbf{r},\nu)\right].\end{aligned} \tag{2.2.3}$$

Equation (2.2.3) can be further simplified by noting that $\overline{\overline{\varepsilon}}_\mathrm{r}(\mathbf{r},\nu)$ is always symmetric (see Ref. [92] and further references therein) and

$$\mathbf{A}\cdot\left(\overline{\overline{\varepsilon}}\mathbf{B}\right)=\left(\overline{\overline{\varepsilon}}^{\mathrm{T}}\mathbf{A}\right)\cdot\mathbf{B}, \tag{2.2.4}$$

where $\overline{\overline{\varepsilon}}^{\mathrm{T}}$ is the transpose of $\overline{\overline{\varepsilon}}$. Therefore, we can write Eq. (2.2.3) as

$$\begin{aligned}\nabla\cdot\left[\mathbf{E}_1(\mathbf{r},\nu)\times\mathbf{H}_2(\mathbf{r},\nu)-\mathbf{E}_2(\mathbf{r},\nu)\times\mathbf{H}_1(\mathbf{r},\nu)\right]=\;&\iota 2\pi\nu\left[\mathbf{P}_2(\mathbf{r},\nu)\cdot\mathbf{E}_1(\mathbf{r},\nu)\right.\\&-\left.\mathbf{P}_1(\mathbf{r},\nu)\cdot\mathbf{E}_2(\mathbf{r},\nu)\right].\end{aligned} \tag{2.2.5}$$

Equation (2.2.5) is known as the unconjugated form of reciprocity relation. Together with Eq. (2.1.4), it provides all the ground work required to establish modal orthogonality that is necessary to describe the mode propagation in waveguiding systems as well as the interaction of modes in the presence of a perturbation. The perturbation term, in principle, can be both linear and nonlinear in nature.

Conjugated reciprocity relation

We now turn our attention to the conjugated form of reciprocity relation. Beginning once again with Eq. (2.2.2), we now relate the two sets of electromagnetic fields as follows:

$$\begin{aligned}\nabla \cdot \left[\mathbf{E}_1(\mathbf{r},\nu)\times\mathbf{H}_2^\star(\mathbf{r},\nu)+\mathbf{E}_2^\star(\mathbf{r},\nu)\times\mathbf{H}_1(\mathbf{r},\nu)\right] = {}& \imath 2\pi\nu\varepsilon_0\left[\left\{\bar{\bar{\varepsilon}}_\mathrm{r}(\mathbf{r},\nu)\,\mathbf{E}_1(\mathbf{r},\nu)\right\}\cdot\mathbf{E}_2^\star(\mathbf{r},\nu)\right.\\ &\left. -\,\mathbf{E}_1(\mathbf{r},\nu)\cdot\left\{\bar{\bar{\varepsilon}}_\mathrm{r}^\star(\mathbf{r},\nu)\,\mathbf{E}_2^\star(\mathbf{r},\nu)\right\}\right]\\ &-\imath 2\pi\nu\left[\mathbf{P}_1(\mathbf{r},\nu)\cdot\mathbf{E}_2^\star(\mathbf{r},\nu)\right.\\ &\left.-\,\mathbf{P}_2^\star(\mathbf{r},\nu)\cdot\mathbf{E}_1(\mathbf{r},\nu)\right]. \qquad (2.2.6)\end{aligned}$$

Simplifying Eq. (2.2.6) in the same way Eq. (2.2.3) was simplified, we arrive at

$$\begin{aligned}\nabla \cdot \left[\mathbf{E}_1(\mathbf{r},\nu)\times\mathbf{H}_2^\star(\mathbf{r},\nu)+\mathbf{E}_2^\star(\mathbf{r},\nu)\times\mathbf{H}_1(\mathbf{r},\nu)\right] = {}& \imath 4\pi\nu\varepsilon_0\left[\Im\left\{\bar{\bar{\varepsilon}}_\mathrm{r}(\mathbf{r},\nu)\right\}\mathbf{E}_1(\mathbf{r},\nu)\right]\cdot\mathbf{E}_2^\star(\mathbf{r},\nu)\\ &+\imath 2\pi\nu\left[\mathbf{P}_1(\mathbf{r},\nu)\cdot\mathbf{E}_2^\star(\mathbf{r},\nu)\right.\\ &\left.-\,\mathbf{P}_2^\star(\mathbf{r},\nu)\cdot\mathbf{E}_1(\mathbf{r},\nu)\right], \qquad (2.2.7)\end{aligned}$$

where $\Im\left\{\bar{\bar{\varepsilon}}_\mathrm{r}(\mathbf{r},\nu)\right\}$ is the imaginary part of $\bar{\bar{\varepsilon}}_\mathrm{r}(\mathbf{r},\nu)$. Equation (2.2.7) is known as the conjugated form of reciprocity relation. We note that Eq. (2.2.7) is rather similar in appearance to its unconjugated counterpart in Eq. (2.2.5) except for the presence of a term depending upon the imaginary part of $\bar{\bar{\varepsilon}}_\mathrm{r}(\mathbf{r},\nu)$ on the right hand side. Due to this factor, it becomes impossible to derive generalized results of mode orthogonality in dissipative media. The details will become apparent in the following section.

2.3 Mode orthogonality

Any treatment of the evolution of electromagnetic field in waveguides necessarily begins with the relations establishing orthogonality between guided modes. This is all the more necessary since the oft-employed framework of conjugated reciprocity theorem

[Eq. (2.2.7)], essentially derived for lossless media [91], is no longer applicable to metallic waveguides which always exhibit significant dissipation at optical frequencies. Therefore, a platform is required which dictates the orthogonality between modes while handling losses in dissipative systems.

Let us consider a waveguide with a cross-section area defined on the xy-plane and extending uniformly along the z-axis which is the direction of mode propagation. According to the definition of Fourier integral in Eq. (2.1.7), we can define the evolution of a waveguide mode propagating along positive z-axis as $\mathbf{E}_i\left(\mathbf{r},\nu\right)=\mathbf{e}_i\left(\mathbf{r}_\perp,\nu\right)\exp\left(\iota\beta_i\left(\nu\right)z\right)$; where the subscript index i denotes the mode order, $\mathbf{e}_i\left(\mathbf{r}_\perp,\nu\right)$ is the vectorial field distribution of the mode over the cross-section, $\mathbf{r}_\perp\epsilon\left\{x,y\right\}$ and $\beta_i\left(\nu\right)$ is the complex mode wave number. Assuming a uniform, unperturbed waveguide such that there are no polarization sources $\mathbf{P}_{\{1,2\}}\left(\mathbf{r},\nu\right)$ in Eq. (2.2.5), we consider two distinct modes of order i and j respectively. Substituting the corresponding fields $\left\{\mathbf{E}_{\{i,j\}}\left(\mathbf{r},\nu\right),\mathbf{H}_{\{i,j\}}\left(\mathbf{r},\nu\right)\right\}$ in Eq. (2.2.5) and employing divergence theorem we obtain [91]:

$$\left[\beta_i\left(\nu\right)+\beta_j\left(\nu\right)\right]\iint\left[\mathbf{e}_i\left(\mathbf{r}_\perp,\nu\right)\times\mathbf{h}_j\left(\mathbf{r}_\perp,\nu\right)-\mathbf{e}_j\left(\mathbf{r}_\perp,\nu\right)\times\mathbf{h}_i\left(\mathbf{r}_\perp,\nu\right)\right]_z dA=0. \tag{2.3.1}$$

In the absence of degenerate modes, the factor $\left[\beta_i\left(\nu\right)+\beta_j\left(\nu\right)\right]$ in Eq. (2.3.1) can be zero only if $\beta_i\left(\nu\right)=-\beta_j\left(\nu\right)$ i.e. $i=-j$. Therefore, we can derive the following orthogonality relation for modes as:

$$\iint\left[\mathbf{e}_i\left(\mathbf{r}_\perp,\nu\right)\times\mathbf{h}_j\left(\mathbf{r}_\perp,\nu\right)-\mathbf{e}_j\left(\mathbf{r}_\perp,\nu\right)\times\mathbf{h}_i\left(\mathbf{r}_\perp,\nu\right)\right]_z dA=K_i\delta_{i,-j}, \tag{2.3.2}$$

where K_i is a constant that depends upon the normalization of modes. Equation (2.3.2) establishes mode orthogonality between all modes except of the same order but propagating in opposite directions ($i=-j$). It is instructive to point out that in deriving Eqs. (2.2.5) and (2.3.1), we did not impose any condition that prohibits the dielectric permittivity $\varepsilon\left(\mathbf{r},\nu\right)$, wave number of the mode $\beta\left(\nu\right)$ or the fields from being complex. Therefore, the results presented here are perfectly valid for both lossless and lossy waveguides. This sets Eq. (2.3.2) apart from the more widely-used orthogonality relations obtained through the framework of conjugated reciprocity relations [91]. In latter, the structure is assumed to be lossless and material dissipation is included as another perturbative polarization source in Eq. (2.2.7). While the approach works to great accuracy for weakly absorbing structures, metallic waveguides at optical frequencies generally become too damped to include mode attenuation perturbatively. Therefore, we shall rely on exact treatment of these systems based on Eqs. (2.2.5) and (2.3.2).

Before proceeding to the next section, we shall take a moment to introduce a simplified notation for Eq. (2.3.2). We use the braket notation for donating the transverse electric and magnetic field components of a mode $\left|\phi_i^{\pm}\right\rangle$ as

$$\left|\phi_i^{\pm}\right\rangle = \left(E_{i,x}^{\pm}, E_{i,y}^{\pm}, H_{i,x}^{\pm}, H_{i,y}^{\pm}\right)^{\mathrm{T}},$$

where the superscript denotes the direction of propagation along $\pm z$-axis. Following the convention introduced in Ref. [93, 94], the integral in Eq. (2.3.2) can thus be rewritten as

$$\left\langle \phi_j^{\pm} \middle| \, \phi_i^{\pm} \right\rangle = \iint \left[\mathbf{e}_{\pm i}\left(\mathbf{r}_{\perp}, \nu\right) \times \mathbf{h}_{\pm j}\left(\mathbf{r}_{\perp}, \nu\right) - \mathbf{e}_{\pm j}\left(\mathbf{r}_{\perp}, \nu\right) \times \mathbf{h}_{\pm i}\left(\mathbf{r}_{\perp}, \nu\right)\right]_z dA. \tag{2.3.3}$$

With above notation, the result of various permutations of mode indices and their signs in Eq. (2.3.3) can be compactly written down as:

$$\begin{aligned} \left\langle \phi_i^{\mp} \middle| \, \phi_j^{\pm} \right\rangle &= \pm K_{\mathrm{i}} \delta_{ij}, \\ \left\langle \phi_i^{\pm} \middle| \, \phi_j^{\pm} \right\rangle &= 0. \end{aligned} \tag{2.3.4}$$

2.4 Modal impedance

Having established the orthogonality of modes in Eq. (2.3.2), we employ it to the problem of impedance of modes in waveguides. The concept of impedance has always been an extremely successful tool in understanding the propagation of electromagnetic waves across the interfaces. It is defined as the ratio between the magnetic and electric field amplitudes of a plane wave in a homogeneous medium [88]:

$$Z = \frac{E}{H} = \sqrt{\frac{\mu}{\epsilon}}, \tag{2.4.1}$$

where E and H are the electric and magnetic field amplitudes respectively. As an instance of the application of wave impedance in the simplest case of a plane wave normally incident on a dielectric interface, the Fresnel reflection and transmission coefficients describing wave reflection and transmission can be described in terms of plane wave impedances as [88]:

$$
\begin{aligned}
r &= \frac{Z_{\mathrm{t}} - Z_{\mathrm{i}}}{Z_{\mathrm{i}} + Z_{\mathrm{t}}}, \\
t &= \frac{2Z_{\mathrm{t}}}{Z_{\mathrm{i}} + Z_{\mathrm{t}}},
\end{aligned} \tag{2.4.2}
$$

where Z_{i} and Z_{t} are the impedances according to Eq. (2.4.1) of the incident and transmitted media denoted by the subscripts i and t respectively. Apart from plane waves in homogeneous media, the impedance concept is also extensively employed in transmission line theory where it encapsulates both the resistive and capacitive effects of the line [61]. In the same vein, the definition of Eq. (2.4.1) remains useful in specific waveguide geometries where the ratio of transverse electric and magnetic field components of the modes remains constant across the waveguide cross-section. Rectangular waveguides made up of perfect electric conductors (PEC) are one famous example in the micro-wave regime [61, 88].

Nevertheless, the concept fails despite its versatility in complex waveguide geometries. The complexity could arise due to both the shape and physical properties of the medium. In these cases, the ratio of the transverse electric and magnetic field components no longer remains constant over the entire cross-section of the geometry, giving rise to the problem of any unique definition of impedance according to Eq. (2.4.1). Over the years, a lot of alternative definitions and averaging techniques have been suggested. For instance, in photonic crystals, some examples can be found in Refs. [95–97]. In the limit when photonic crystals support only single mode, a more analytically exact solution was presented in the form of Bloch mode impedances [98, 99].

Hereby, we present one such attempt which aims to restore the Fresnel formulation of Eq. (2.4.2) for the interfaces involving lossy waveguides in which it is generally not possible to define impedance of the modes through Eq. (2.4.1) due to the problems already indicated. As it turns out, the implication of our results for the impedance definition turns out to be completely different from what is familiarly known.

Let us consider an interface between any two waveguides where the transverse components of the modes supported by the incident and transmitted waveguides are denoted by $\left|\phi_i^{\pm}\right\rangle$and $\left|\psi_j^{\pm}\right\rangle$ respectively. The subscript $\{i, j\}$ denotes order of the mode in each waveguide whereas the plus and minus signs in the superscript signify propagation in positive or negative propagation direction which we shall take to be along z-axis for our discussion. The interface between the waveguides is assumed to be formed at $z = 0$ such that the incident waveguide is placed in $z < 0$ and transmitted for $z > 0$ (Fig. 2.4.1).

The modes in the respective media are normalized such that Eq. (2.3.4) becomes

$$\begin{aligned} \left\langle \phi_i^{\mp} \middle| \phi_j^{\pm} \right\rangle &= \left\langle \psi_i^{\mp} \middle| \psi_j^{\pm} \right\rangle = \pm\delta_{ij}, \\ \left\langle \phi_i^{\pm} \middle| \phi_j^{\pm} \right\rangle &= \left\langle \psi_i^{\pm} \middle| \psi_j^{\pm} \right\rangle = 0. \end{aligned} \tag{2.4.3}$$

At the interface, the continuity of the transverse components requires

$$\left|\phi_n^{+}\right\rangle + \sum_l r_{ln} \left|\phi_l^{-}\right\rangle = \sum_l t_{ln} \left|\psi_l^{+}\right\rangle, \tag{2.4.4}$$

where r_{ln} denotes reflection into mode order l due to incident mode order n, t_{ln} similarly defines transmission into mode order l due to incident mode order n. Any arbitrary incident illumination $|\phi^{+}\rangle$ can be decomposed into waveguide modes as

$$\left|\phi^{+}\right\rangle = \sum_n c_n \left|\phi_n^{+}\right\rangle,$$

where the coefficients c_n are obtained by projecting the mode $|\phi_n^{+}\rangle$ on the total incident field $|\phi^{+}\rangle$ which is defined using Eq. (2.4.3) as

$$c_n = \left\langle \phi_n^{-} \middle| \phi^{+} \right\rangle. \tag{2.4.5}$$

In order to derive intuitively meaningful results, we consider a system in which the incident and transmitted waveguides support only a single propagating mode at the frequency of operation. This is true, for instance, in rectangular waveguides made with PEC boundaries in microwave regime for the right combination of core dimensions and operating frequency [61]. Although coupling to radiating and evanescent modes usually have to be taken into account, here we consider a case where it can be approximated to be negligible. With this, Eq. (2.4.4) reduces to

$$\left|\phi_0^{+}\right\rangle + r_0 \left|\phi_0^{-}\right\rangle = t_0 \left|\psi_0^{+}\right\rangle. \tag{2.4.6}$$

A straightforward application of Eq. (2.4.3) yields:

$$
\begin{aligned}
r_0 &= -\frac{\left\langle \phi_0^+ \middle| \psi_0^+ \right\rangle}{\left\langle \phi_0^- \middle| \psi_0^+ \right\rangle}, \\
t_0 &= \frac{1}{\left\langle \phi_0^- \middle| \psi_0^+ \right\rangle}.
\end{aligned}
\tag{2.4.7}
$$

It is obvious that unlike r_0, t_0 is dependent upon the normalization of modes propagating in the two interfacing waveguides. We will come back to resolve this apparent inconsistency later. For now, we attempt to solve the problem of modal impedance which in the special case of relative impedance fortunately does not depend upon the modal transmission t_0. The formula of Fresnel reflection coefficient in Eq. (2.4.2) can be inverted to obtain:

$$
z_\mathrm{r} = \frac{Z_\psi}{Z_\phi} = \frac{1+r_0}{1-r_0}, \tag{2.4.8}
$$

where z_r is the relative impedance of the mode defined as the ratio of the impedance of transmitted mode with respect to the incident. Substituting the formula of r_0 from Eq. (2.4.7) in the above equation, we find the relative impedance to be

$$
z_\mathrm{r} = \frac{\left\langle \phi_0^- - \phi_0^+ \middle| \psi_0^+ \right\rangle}{\left\langle \phi_0^- + \phi_0^+ \middle| \psi_0^+ \right\rangle}. \tag{2.4.9}
$$

It is instructive to take a pause here and reflect upon the significance of the result obtained in Eq. (2.4.9). It is well understood that the coupling of modes between the two interfacing waveguides or media is determined by the overlap between the incident and transmitted modes. Less expected, however, is the fact that relative impedance between the two waveguides can be similarly defined as a function of the overlap between modes supported by the respective waveguides. While it does not seem possible in our formulation to assign any unique modal impedance to an individual waveguide, having relative value at hand is still useful in solving problems where the major concern is to minimize reflection from the interface. Compared to the field averaging techniques usually employed, it provides a theoretically exact definition of the modal reflection and transmission at the interface between waveguides.

With the reflection coefficient and relative impedance well defined, we can return to the issue of mode normalization suitable for defining the transmission of mode across the interface. Without any loss of generality, we normalize the mode propagating in the transmitted waveguide $\left|\psi_i^\pm\right\rangle$ with factor N_i such that Eq. (2.4.3) now becomes

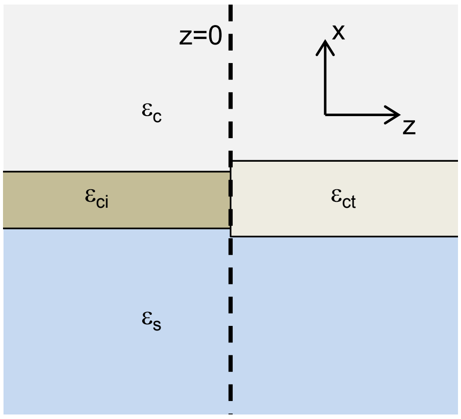

Figure 2.4.1: Schematic sketch showing the interface between two dielectric waveguides having a geometrical as well as material disparity (core permittivities $\varepsilon_{\mathrm{ci}}$ and $\varepsilon_{\mathrm{ct}}$). Substrate and cladding have been shown to be the same (ε_{c} and ε_{s}) across the interface without any loss of generality.

$$\begin{aligned} \left\langle \phi_i^{\mp} \middle| \phi_j^{\pm} \right\rangle &= \pm\delta_{ij}, \\ \left\langle \psi_i^{\mp} \middle| \psi_j^{\pm} \right\rangle &= \pm\frac{\delta_{ij}}{N_{\mathrm{i}}^2}. \end{aligned} \tag{2.4.10}$$

Likewise, the Eq. (2.4.7) for transmission coefficient thus reads as

$$t_0 = \frac{N_0}{\left\langle \phi_0^{-} \middle| \psi_0^{+} \right\rangle}. \tag{2.4.11}$$

For the correct normalization of modes, the formula for t_0 in Eq. (2.4.2) should hold good. Substituting the values of relative impedance z_{r} and t_0 in Eq. (2.4.2) gives:

$$N_0 = \left\langle \phi_0^{-} - \phi_0^{+} \middle| \psi_0^{+} \right\rangle. \tag{2.4.12}$$

Equation (2.4.12) provides us the normalization of modes in transmitted waveguide for restoring the meaning of mode transmission coefficient t_0.

Multimode

In waveguides supporting multiple modes it is still possible to obtain the reflection coefficient and associate relative impedance for the system. By successively projecting $|\psi_n^{+}\rangle$ for each mode order n on Eq. (2.4.4) and introducing a matrix notation, we can straightforwardly obtain the reflection matrix:

$$\hat{r} = -\hat{P}^{-1}\hat{Q}, \tag{2.4.13}$$

where $\hat{P}$ and $\hat{Q}$ are matrices defined as

$$\hat{P}_{mn} = \left\langle \psi_m^+ \middle| \phi_n^- \right\rangle, \quad \hat{Q}_{mn} = \left\langle \psi_m^+ \middle| \phi_n^+ \right\rangle. \tag{2.4.14}$$

The resultant formula for the matrix elements of relative impedance $\hat{z}$ is written as:

$$\hat{z}_{mn} = \frac{1 - \Sigma_k \left(\hat{P}^{-1}\right)_{mk} Q_{kn}}{1 + \Sigma_k \left(\hat{P}^{-1}\right)_{mk} Q_{kn}}. \tag{2.4.15}$$

The results derived in this section have been included as an application of the mode orthogonality relations to the problem of impedance definition in dissipative waveguides. Due to space constraints, we will not present any application of these results in the remainder of this treatise. Interested reader may refer to Ref. [100] where we discuss further details and applications.

2.5 Coupled mode theory

Another interesting application of Eq. (2.3.2) is to the problem of mode propagation in waveguides subject to a nonlinear perturbation term $\mathbf{P}(\mathbf{r}, \nu)$. The general form of the nonlinear polarization can become very complex to describe if we take into account the full-breadth of the nonlinear response that may arise in a medium. We shall, therefore, restrict our attention to non-centrosymmetric media whose second order $\chi^{(2)}$ tensor dominates over all possible nonlinear responses. In the following, we adapt existing coupled mode formulation for describing nonlinear interaction according to our requirement (see, for instance, Ref. [101] and further references therein).

In case of nonlinear perturbation, the total field in the waveguide has to be represented as the linear superposition of modes. Having said that, it helps taking note of the fact that in the cases we are going to study, the waveguide is mono-mode at fundamental harmonic (FH). Although, this is something usually true in a lot of waveguides of practical interest. Therefore, it suffices to consider the multi-mode dynamics only at higher frequencies i.e. SH. As we shall be exclusively interested in the nonlinear second harmonic generation (SHG) in the presence of $\chi^{(2)}$ nonlinearity, the total field ansatz in the waveguide can be written as

$$\begin{aligned}
\tilde{\mathbf{E}}_1(\mathbf{r},t) &= \tilde{u}_0^{\mathrm{F}}(z,t)\,\mathbf{e}_0^{\mathrm{F}}(\mathbf{r}_\perp)\exp\left[\iota\left(\beta_0^{\mathrm{F}}z-2\pi\nu^{\mathrm{F}}t\right)\right]\\
&\quad+\sum_m \tilde{u}_m^{\mathrm{S}}(z,t)\,\mathbf{e}_m^{\mathrm{S}}(\mathbf{r}_\perp)\exp\left[\iota\left(\beta_m^{\mathrm{S}}z-2\pi\nu^{\mathrm{S}}t\right)\right]+c.c.,\\
\tilde{\mathbf{H}}_1(\mathbf{r},t) &= \tilde{u}_0^{\mathrm{F}}(z,t)\,\mathbf{h}_0^{\mathrm{F}}(\mathbf{r}_\perp)\exp\left[\iota\left(\beta_0^{\mathrm{F}}z-2\pi\nu^{\mathrm{F}}t\right)\right]\\
&\quad+\sum_m \tilde{u}_m^{\mathrm{S}}(z,t)\,\mathbf{h}_m^{\mathrm{S}}(\mathbf{r}_\perp)\exp\left[\iota\left(\beta_m^{\mathrm{S}}z-2\pi\nu^{\mathrm{S}}t\right)\right]+c.c..
\end{aligned}\tag{2.5.1}$$

The subscript m in Eqs. (2.5.1) is the mode order, the superscript F and S denote the fundamental harmonic (FH) and second harmonic (SH) respectively ($\nu^{\mathrm{S}} = 2\nu^{\mathrm{F}}$) while $\beta_m^{\{\mathrm{F,S}\}}$ is the complex modal wave number. Perturbative effect on the evolution of modes due to nonlinearity is expressed through slowly varying envelope $\tilde{u}_m^{\{\mathrm{F,S}\}}(z,t)$. Performing Fourier transformation of Eq. (2.5.1), we obtain

$$\begin{aligned}
\mathbf{E}_1(\mathbf{r},\nu) &= u_0^{\mathrm{F}}\left(z,\nu-\nu^{\mathrm{F}}\right)\mathbf{e}_0^{\mathrm{F}}(\mathbf{r}_\perp)\exp\left(\iota\beta_0^{\mathrm{F}}z\right)+\left\{u_0^{\mathrm{F}}\left(z,\nu+\nu^{\mathrm{F}}\right)\mathbf{e}_0^{\mathrm{F}}(\mathbf{r}_\perp)\right\}^\star\exp\left(-\iota\beta_0^{\mathrm{F}}z\right)\\
&+\sum_m\left[u_m^{\mathrm{S}}\left(z,\nu-\nu^{\mathrm{S}}\right)\mathbf{e}_m^{\mathrm{S}}(\mathbf{r}_\perp)\exp\left(\iota\beta_m^{\mathrm{S}}z\right)+\left\{u_m^{\mathrm{S}}\left(z,\nu+\nu^{\mathrm{S}}\right)\mathbf{e}_m^{\mathrm{S}}(\mathbf{r}_\perp)\right\}^\star\exp\left(-\iota\beta_m^{\mathrm{S}}z\right)\right],\\
\mathbf{H}_1(\mathbf{r},\nu) &= u_0^{\mathrm{F}}\left(z,\nu-\nu^{\mathrm{F}}\right)\mathbf{h}_0^{\mathrm{F}}(\mathbf{r}_\perp)\exp\left(\iota\beta_0^{\mathrm{F}}z\right)+\left\{u_0^{\mathrm{F}}\left(z,\nu+\nu^{\mathrm{F}}\right)\mathbf{h}_0^{\mathrm{F}}(\mathbf{r}_\perp)\right\}^\star\exp\left(-\iota\beta_0^{\mathrm{F}}z\right)\\
&+\sum_m\left[u_m^{\mathrm{S}}\left(z,\nu-\nu^{\mathrm{S}}\right)\mathbf{h}_m^{\mathrm{S}}(\mathbf{r}_\perp)\exp\left(\iota\beta_m^{\mathrm{S}}z\right)+\left\{u_m^{\mathrm{S}}\left(z,\nu+\nu^{\mathrm{S}}\right)\mathbf{h}_m^{\mathrm{S}}(\mathbf{r}_\perp)\right\}^\star\exp\left(-\iota\beta_m^{\mathrm{S}}z\right)\right].
\end{aligned}\tag{2.5.2}$$

Utilizing the fact that $u_m^{\{\mathrm{F,S}\}}(z,t)$ is a slowly varying envelope in time, we can simplify Eqs. (2.5.2) above for cases when the carrier frequency $\nu^{\{\mathrm{F,S}\}}$ is much higher compared to the bandwidth of $u_m(z,\nu)$ as it should be at optical frequencies. Therefore, we can ignore the terms depending upon $\left\{u_m^{\{\mathrm{F,S}\}}\left(z,\nu+\nu^{\{\mathrm{F,S}\}}\right)\right\}^\star$ to write

$$\begin{aligned}
\mathbf{E}_1(\mathbf{r},\nu) &\approx u_0^{\mathrm{F}}\left(z,\nu-\nu^{\mathrm{F}}\right)\mathbf{e}_0^{\mathrm{F}}(\mathbf{r}_\perp)\exp\left(\iota\beta_0^{\mathrm{F}}z\right)+\sum_m u_m^{\mathrm{S}}\left(z,\nu-\nu^{\mathrm{S}}\right)\mathbf{e}_m^{\mathrm{S}}(\mathbf{r}_\perp)\exp\left(\iota\beta_m^{\mathrm{S}}z\right),\\
\mathbf{H}_1(\mathbf{r},\nu) &\approx u_0^{\mathrm{F}}\left(z,\nu-\nu^{\mathrm{F}}\right)\mathbf{h}_0^{\mathrm{F}}(\mathbf{r}_\perp)\exp\left(\iota\beta_0^{\mathrm{F}}z\right)+\sum_m u_m^{\mathrm{S}}\left(z,\nu-\nu^{\mathrm{S}}\right)\mathbf{h}_m^{\mathrm{S}}(\mathbf{r}_\perp)\exp\left(\iota\beta_m^{\mathrm{S}}z\right).
\end{aligned}\tag{2.5.3}$$

The perturbative polarization associated with the quadratic nonlinear interaction is defined as

$$\tilde{\mathbf{P}}_1(\mathbf{r},t)=\sum_m\left\{\tilde{\mathbf{p}}_m^{\mathrm{F}}(\mathbf{r},t)\exp\left[\iota\left(\beta_0^{\mathrm{F}}z-\nu^{\mathrm{F}}t\right)\right]+\tilde{\mathbf{p}}_m^{\mathrm{S}}(\mathbf{r},t)\exp\left[\iota\left(\beta_m^{\mathrm{S}}z-2\pi\nu^{\mathrm{S}}t\right)\right]\right\}+c.c., \tag{2.5.4}$$

where $\tilde{\mathbf{p}}_m^{\{\mathrm{F,S}\}}(\mathbf{r},t)$ is once again a slowly varying polarization envelope owing to the mode of order m at SH whose exact expression shall be described later. Taking Fourier transform of Eq. (2.5.4), we write

$$\mathbf{P}_1(\mathbf{r},\nu)\approx\sum_m\left\{\mathbf{p}_m^{\mathrm{F}}\left(\mathbf{r},\nu-\nu^{\mathrm{F}}\right)\exp\left(\iota\beta_0^{\mathrm{F}}z\right)+\mathbf{p}_m^{\mathrm{S}}\left(\mathbf{r},\nu-\nu^{\mathrm{S}}\right)\exp\left(\iota\beta_m^{\mathrm{S}}z\right)\right\}, \tag{2.5.5}$$

where $\tilde{\mathbf{p}}_{0m}^{\{\mathrm{F,S}\}}(\mathbf{r},t)$ is treated as a narrow band signal in the way explained before. In order to apply the reciprocity relations [Eq. (2.2.5)], we define another set of fields $\{\mathbf{E}_2(\mathbf{r},\nu),\mathbf{H}_2(\mathbf{r},\nu)\}$ but this time in the absence of any perturbation $[\mathbf{P}_2(\mathbf{r},\nu)=0]$. To be able to exploit the mode orthogonality defined in Eq. (2.3.2), we choose a back propagating mode of order M. Exploiting the vectorial symmetry between the forward and backward propagating modes and noting that

$$\beta_{\mathrm{M}}(\nu)=-\beta_{-\mathrm{M}}(\nu), \tag{2.5.6}$$

the electromagnetic fields can be defined as:

$$\begin{aligned}\mathbf{E}_2(\mathbf{r},\nu)&=\left[\mathbf{e}_{\mathrm{M}\perp}(\mathbf{r}_\perp,\nu)-\mathbf{e}_{\mathrm{M}z}(\mathbf{r}_\perp,\nu)\right]\exp\left(-\iota\beta_{\mathrm{M}}(\nu)z\right),\\ \mathbf{H}_2(\mathbf{r},\nu)&=\left[-\mathbf{h}_{\mathrm{M}\perp}(\mathbf{r}_\perp,\nu)+\mathbf{h}_{\mathrm{M}z}(\mathbf{r}_\perp,\nu)\right]\exp\left(-\iota\beta_{\mathrm{M}}(\nu)z\right),\end{aligned} \tag{2.5.7}$$

where $\mathbf{e}_{\mathrm{M}\perp}(\mathbf{r}_\perp,\nu)$ and $\mathbf{h}_{\mathrm{M}\perp}(\mathbf{r}_\perp,\nu)$ are the transverse modal field components with respect to the direction of propagation (z-axis). Inserting Eqs. (2.5.1) and (2.5.7) into Eq. (2.2.5) and applying the mode orthogonality condition [Eq. (2.2.5)], we obtain the following set of coupled differential equations:

$$\begin{aligned}
&\hat{N}_{0\mathrm{M}}^{\mathrm{F}}(\nu)\left\{\frac{\partial u_0^{\mathrm{F}}\left(z,\nu-\nu^{\mathrm{F}}\right)}{\partial z}+\iota\left\{\beta_0^{\mathrm{F}}-\beta_{\mathrm{M}}(\nu)\right\}u_0^{\mathrm{F}}\left(z,\nu-\nu^{\mathrm{F}}\right)\right\}\exp\left[\iota\left\{\beta_0^{\mathrm{F}}-\beta_{\mathrm{M}}(\nu)\right\}z\right]\\
&+\sum_m \hat{N}_{m\mathrm{M}}^{S}(\nu)\left\{\frac{\partial u_m^{\mathrm{S}}\left(z,\nu-\nu^{\mathrm{S}}\right)}{\partial z}+\iota\left\{\beta_m^{\mathrm{S}}-\beta_{\mathrm{M}}(\nu)\right\}u_m^{\mathrm{S}}\left(z,\nu-\nu^{\mathrm{S}}\right)\right\}\exp\left[\iota\left\{\beta_m^{\mathrm{S}}-\beta_{\mathrm{M}}(\nu)\right\}z\right]=\\
&\iota\nu\sum_m\iint d\mathbf{r}_\perp\left\{\mathbf{p}_m^{\mathrm{F}}\left(\mathbf{r},\nu-\nu^{\mathrm{F}}\right)\exp\left(\iota\beta_0^{\mathrm{F}}z\right)+\mathbf{p}_m^{\mathrm{S}}\left(\mathbf{r},\nu-\nu^{\mathrm{S}}\right)\exp\left(\iota\beta_m^{\mathrm{S}}z\right)\right\}.\mathbf{E}_2(\mathbf{r},\nu),
\end{aligned} \tag{2.5.8}$$

where $\hat{N}_{m\mathrm{M}}^{\{F,S\}}(\nu)$ is defined as

$$\hat{N}_{m\mathrm{M}}^{\{\mathrm{F,S}\}}(\nu)=\frac{1}{2\pi}\iint_{-\infty}^{\infty}d\mathbf{r}_\perp\left[\mathbf{e}_{m\perp}^{\{\mathrm{F,S}\}}(\mathbf{r}_\perp)\times\mathbf{h}_{\mathrm{M}\perp}(\mathbf{r}_\perp,\nu)+\mathbf{e}_{\mathrm{M}\perp}(\mathbf{r}_\perp,\nu)\times\mathbf{h}_{m\perp}^{\{\mathrm{F,S}\}}(\mathbf{r}_\perp)\right]. \tag{2.5.9}$$

At this stage, we shall now utilize the fact that $u_m^{\{\mathrm{F,S}\}}\left(z,\nu-\nu^{\{\mathrm{F,S}\}}\right)$ is narrowly centered around $\nu^{\{\mathrm{F,S}\}}$. Therefore, we can approximate the coefficients of $u_m^{\{\mathrm{F,S}\}}\left(z,\nu-\nu^{\{\mathrm{F,S}\}}\right)$ appearing in Eq. (2.5.8) by dropping the frequency dependance:

$$\hat{N}_{m\mathrm{M}}^{\{\mathrm{F,S}\}}(\nu)\approx\hat{N}_{\mathrm{mM}}^{\{\mathrm{F,S}\}}=\frac{1}{\pi}\iint d\mathbf{r}_\perp\mathbf{e}_{m\perp}^{\{\mathrm{F,S}\}}(\mathbf{r}_\perp)\times\mathbf{h}_{\mathrm{M}\perp}^{\{\mathrm{F,S}\}}. \tag{2.5.10}$$

Similarly, the mode vector $\beta_{\mathrm{M}}(\nu)$ is approximated to first order Taylor expansion around the center frequency $\nu^{\{\mathrm{F,S}\}}$ when being a coefficient of $u_m^{\{\mathrm{F,S}\}}\left(z,\nu-\nu^{\{\mathrm{F,S}\}}\right)$. Applying mode orthogonality in Eq. (2.5.10) allows us to rewrite Eq. (2.5.8) as

$$\begin{aligned}
&N_{\mathrm{M}}^{\mathrm{F}}\left\{\frac{\partial u_{\mathrm{M}}^{\mathrm{F}}\left(z,\nu-\nu^{\mathrm{F}}\right)}{\partial z}-\frac{\iota}{v_{\mathrm{M}}^{\mathrm{F}}}u_{\mathrm{M}}^{\mathrm{F}}\left(z,\nu-\nu^{\mathrm{F}}\right)\left(\nu-\nu^{\mathrm{F}}\right)\right\}\exp\left(\iota\beta_{\mathrm{M}}^{\mathrm{F}}z\right)\\
&+N_{\mathrm{M}}^{\mathrm{S}}\left\{\frac{\partial u_{\mathrm{M}}^{\mathrm{S}}\left(z,\nu-\nu^{\mathrm{S}}\right)}{\partial z}-\iota\frac{\iota}{v_{\mathrm{M}}^{\mathrm{S}}}u_{\mathrm{M}}^{\mathrm{S}}\left(z,\nu-\nu^{\mathrm{S}}\right)\left(\nu-\nu^{\mathrm{S}}\right)\right\}\exp\left(\iota\beta_{\mathrm{M}}^{\mathrm{S}}z\right)=\\
&\iota\nu\sum_m\iint d\mathbf{r}_\perp\left\{\mathbf{p}_m^{\mathrm{F}}\left(\mathbf{r},\nu-\nu^{\mathrm{F}}\right)\exp\left(\iota\beta_0^{\mathrm{F}}z\right)\right.\\
&\left.+\mathbf{p}_m^{\mathrm{S}}\left(\mathbf{r},\nu-\nu^{\mathrm{S}}\right)\exp\left(\iota\beta_m^{\mathrm{S}}z\right)\right\}\cdot\mathbf{E}_2(\mathbf{r},\nu)\exp\left(\iota\beta_{\mathrm{M}}(\nu)z\right),
\end{aligned} \tag{2.5.11}$$

where $N_{\mathrm{M}}^{\{\mathrm{F,S}\}}$is finally defined as

$$N_{\mathrm{M}}^{\{\mathrm{F,S}\}} = \frac{1}{\pi} \iint d\mathbf{r}_{\perp} \mathbf{e}_{\mathrm{M}\perp}^{\{\mathrm{F,S}\}} \left(\mathbf{r}_{\perp}\right) \times \mathbf{h}_{\mathrm{M}\perp}^{\{\mathrm{F,S}\}} \left(\mathbf{r}_{\perp}\right) \tag{2.5.12}$$

and the group velocity $v_{\mathrm{M}}^{\{\mathrm{F,S}\}}$ of the mode comes from the first order term in Taylor expansion which is given as

$$v_{\mathrm{M}}^{\{\mathrm{F,S}\}} = \left[\left. \frac{\partial \beta_{\mathrm{M}} \left(\nu\right)}{\partial \nu} \right|_{\nu^{\{\mathrm{F,S}\}}} \right]^{-1} . \tag{2.5.13}$$

We can provide similar treatment to the right hand side of Eq. (2.5.11) as well. The product $\mathbf{p}_{m}^{\{\mathrm{F,S}\}} \left(\mathbf{r}, \nu - \nu^{\{\mathrm{F,S}\}}\right) \cdot \mathbf{E}_{2} \left(\mathbf{r}, \nu\right)$ appearing in Eq. (2.5.11) can also be simplified considering that $\mathbf{p}_{m}^{\{\mathrm{F,S}\}} \left(\mathbf{r}, \nu - \nu^{\{\mathrm{F,S}\}}\right)$ is likewise narrowly centered around $\nu = \nu^{\{\mathrm{F,S}\}}$. Therefore, it can be rewritten as

$$\mathbf{p}_{m}^{\{\mathrm{F,S}\}} \left(\mathbf{r}, \nu - \nu^{\{\mathrm{F,S}\}}\right) . \mathbf{E}_{2} \left(\mathbf{r}, \nu\right) \approx \mathbf{p}_{m}^{\{\mathrm{F,S}\}} \left(\mathbf{r}, \nu - \nu^{\{\mathrm{F,S}\}}\right) . \left[\mathbf{e}_{\mathrm{M}\perp}^{\{\mathrm{F,S}\}} \left(\mathbf{r}_{\perp}\right) - \mathbf{e}_{\mathrm{M}z}^{\{\mathrm{F,S}\}} \left(\mathbf{r}_{\perp}\right) \right] \exp \left(-\iota \beta_{\mathrm{M}} \left(\nu\right) z\right) . \tag{2.5.14}$$

Inserting the above definition of $\mathbf{p}_{m}^{\{\mathrm{F,S}\}} \left(\mathbf{r}, \nu - \nu^{\{\mathrm{F,S}\}}\right) \cdot \mathbf{E}_{2} \left(\mathbf{r}, \nu\right)$ from the equation above in Eq. (2.5.11) and performing the inverse Fourier transform yields:

$$\begin{aligned} N_{0}^{\mathrm{F}} & \left\{ \frac{\partial \tilde{u}_{0}^{\mathrm{F}} \left(z, t\right)}{\partial z} + \frac{1}{v_{0}^{\mathrm{F}}} \frac{\partial \tilde{u}_{0}^{\mathrm{F}} \left(z, t\right)}{\partial t} \right\} \exp \left[\iota \left(\beta_{0}^{\mathrm{F}} z - \nu^{\mathrm{F}} t \right) \right] \\ + N_{\mathrm{M}}^{\mathrm{S}} & \left\{ \frac{\partial \tilde{u}_{\mathrm{M}}^{\mathrm{S}} \left(z, t\right)}{\partial z} + \frac{1}{v_{\mathrm{M}}^{\mathrm{S}}} \frac{\partial \tilde{u}_{\mathrm{M}}^{\mathrm{S}} \left(z, t\right)}{\partial t} \right\} \exp \left[\iota \left(\beta_{\mathrm{M}}^{\mathrm{S}} z - \nu^{\mathrm{S}} t \right) \right] = \\ \sum_{m} \iint d\mathbf{r}_{\perp} & \left\{ \tilde{\mathbf{p}}_{m}^{\mathrm{F}} \left(\mathbf{r}, t\right) . \left[\mathbf{e}_{0\perp}^{\mathrm{F}} \left(\mathbf{r}_{\perp}\right) - \mathbf{e}_{0z}^{\mathrm{F}} \left(\mathbf{r}_{\perp}\right) \right] \exp \left[\iota \left(\beta_{0}^{\mathrm{F}} z - \nu^{\mathrm{F}} t \right) \right] \right. \\ & \left. + \tilde{\mathbf{p}}_{m}^{\mathrm{S}} \left(\mathbf{r}, t\right) . \left[\mathbf{e}_{\mathrm{M}\perp}^{\mathrm{S}} \left(\mathbf{r}_{\perp}\right) - \mathbf{e}_{\mathrm{M}z}^{\mathrm{S}} \left(\mathbf{r}_{\perp}\right) \right] \exp \left[\iota \left(\beta_{m}^{\mathrm{S}} z - \nu^{\mathrm{S}} t \right) \right] \right\} . \end{aligned} \tag{2.5.15}$$

By comparing the coefficients of $\exp \left[\iota \left(\beta_{m}^{\{\mathrm{F,S}\}} z - \nu^{\{\mathrm{F,S}\}} t \right) \right]$ we easily obtain the following set of equations for the mode envelope $\tilde{u}_{\mathrm{M}}^{\mathrm{F,S}} \left(z, t\right)$:

$$\begin{aligned} \frac{\partial \tilde{u}_{0}^{\mathrm{F}} \left(z, t\right)}{\partial z} + \frac{1}{v_{0}^{\mathrm{F}}} \frac{\partial \tilde{u}_{0}^{\mathrm{F}} \left(z, t\right)}{\partial t} &= \frac{1}{N_{0}^{\mathrm{F}}} \sum_{m} \iint d\mathbf{r}_{\perp} \tilde{\mathbf{p}}_{m}^{\mathrm{F}} \left(\mathbf{r}, t\right) . \left[\mathbf{e}_{0\perp}^{\mathrm{F}} \left(\mathbf{r}_{\perp}\right) - \mathbf{e}_{0z}^{\mathrm{F}} \left(\mathbf{r}_{\perp}\right) \right] , \\ \frac{\partial \tilde{u}_{\mathrm{M}}^{\mathrm{S}} \left(z, t\right)}{\partial z} + \frac{1}{v_{\mathrm{M}}^{\mathrm{S}}} \frac{\partial \tilde{u}_{\mathrm{M}}^{\mathrm{S}} \left(z, t\right)}{\partial t} &= \frac{1}{N_{\mathrm{M}}^{\mathrm{S}}} \iint d\mathbf{r}_{\perp} \tilde{\mathbf{p}}_{\mathrm{M}}^{\mathrm{S}} \left(\mathbf{r}, t\right) . \left[\mathbf{e}_{\mathrm{M}\perp}^{\mathrm{S}} \left(\mathbf{r}_{\perp}\right) - \mathbf{e}_{\mathrm{M}z}^{\mathrm{S}} \left(\mathbf{r}_{\perp}\right) \right] . \end{aligned} \tag{2.5.16}$$

We can now finally address the nonlinear polarization $\mathbf{p}_m^{\{\mathrm{F},\mathrm{S}\}}(\mathbf{r},t)$. As is often the case, for a narrow-band pulse with a carrier frequency $\nu^{\{\mathrm{F},\mathrm{S}\}}$ much away from material resonance, the nonlinear response can be approximated to be instantaneous and Kleinman symmetry holds good [87]. The nonlinear polarization at each harmonic is then defined as

$$\tilde{\mathbf{p}}_m^{\mathrm{F}}(\mathbf{r},t) = \chi^{(2)}\left(\mathbf{r}_\perp, -\nu^{\mathrm{F}}; -\nu^{\mathrm{F}}, \nu^{\mathrm{S}}\right)\left\{\tilde{u}_0^{\mathrm{F}}(z,t)\right\}^\star \tilde{u}_m^{\mathrm{S}}(z,t)\exp\left(\iota\left(\beta_m^{\mathrm{S}} - 2\beta_0^{\mathrm{F}}\right)z\right) \tag{2.5.17}$$

and

$$\tilde{\mathbf{p}}_m^{\mathrm{S}}(\mathbf{r},t) = \chi^{(2)}\left(\mathbf{r}_\perp, -2\nu^{\mathrm{F}}; \nu^{\mathrm{F}}, \nu^{\mathrm{F}}\right)\left\{u_0^{\mathrm{F}}(z,t)\right\}^2 \exp\left(-\iota\left(\beta_m^{\mathrm{S}} - 2\beta_0^{\mathrm{F}}\right)z\right), \tag{2.5.18}$$

where $\chi^{(2)}\left(\mathbf{r}_\perp, -\nu^{\mathrm{F}}; -\nu^{\mathrm{F}}, \nu^{\mathrm{S}}\right)$ and $\chi^{(2)}\left(\mathbf{r}_\perp, -2\nu^{\mathrm{F}}; \nu^{\mathrm{F}}, \nu^{\mathrm{F}}\right)$ are the nonlinear susceptibility tensors defined for the polarizations at FH and SH respectively according to terminology defined in Ref. [101].

We can further incorporate the effect of linear damping of the mode explicitly through the transformation

$$\tilde{a}_m^{\{\mathrm{F},\mathrm{S}\}}(z,t) = \tilde{u}_m^{\{\mathrm{F},\mathrm{S}\}}(z,t)\exp\left(\beta_m''^{\{\mathrm{F},\mathrm{S}\}} z\right), \tag{2.5.19}$$

where $\beta_m''^{\{\mathrm{F},\mathrm{S}\}} = \Im\left\{\beta_m^{\{\mathrm{F},\mathrm{S}\}}\right\}$. Defining the momentum mismatch in Eqs. (2.5.17) and (2.5.18) as

$$\Delta\beta_m = \Re\left\{\beta_m^{\mathrm{S}} - 2\beta_0^{\mathrm{F}}\right\} \tag{2.5.20}$$

and substituting Eqs. (2.5.17) and (2.5.18) into Eqs. (2.5.16), we arrive at the final form of temporal coupled mode equations:

$$\begin{aligned}
\frac{\partial \tilde{a}_0^{\mathrm{F}}(z,t)}{\partial z} + \frac{1}{v_{\mathrm{M}}^{\mathrm{F}}}\frac{\partial \tilde{a}_0^{\mathrm{F}}(z,t)}{\partial t} + \beta_0''^{\mathrm{F}}\tilde{a}_0^{\mathrm{F}}(z,t) &= \iota\sum_m \gamma_m^{\mathrm{F}}\left\{\tilde{a}_0^{\mathrm{F}}(z,t)\right\}^\star \tilde{a}_m^{\mathrm{S}}(z,t)\exp\left(\iota\Delta\beta_m z\right),\\
\frac{\partial \tilde{a}_{\mathrm{M}}^{\mathrm{S}}(z,t)}{\partial z} + \frac{1}{v_{\mathrm{M}}^{\mathrm{S}}}\frac{\partial \tilde{a}_{\mathrm{M}}^{\mathrm{S}}(z,t)}{\partial t} + \beta_{\mathrm{M}}''^{\mathrm{S}}\tilde{a}_{\mathrm{M}}^{\mathrm{S}}(z,t) &= \iota\gamma_{\mathrm{M}}^{\mathrm{S}}\left\{\tilde{a}_0^{\mathrm{F}}(z,t)\right\}^2\exp\left(-\iota\Delta\beta_{\mathrm{M}} z\right),
\end{aligned} \tag{2.5.21}$$

The complex mode overlap coefficient $\gamma_{\mathrm{m}}^{\{\mathrm{F},\mathrm{S}\}}$ in Eqs. (2.5.21) is defined as

$$\gamma_m^{\mathrm{F}} = \frac{\nu^{\mathrm{F}}}{N_0^{\mathrm{F}}} \iint d\mathbf{r}_\perp \chi^{(2)} \left(\mathbf{r}_\perp, -\nu^{\mathrm{F}}; -\nu^{\mathrm{F}}, \nu^{\mathrm{S}}\right) . \left[\mathbf{e}_{0\perp}^{\mathrm{F}} \left(\mathbf{r}_\perp\right) - \mathbf{e}_{0z}^{\mathrm{F}} \left(\mathbf{r}_\perp\right)\right],$$
$$\gamma_m^{\mathrm{S}} = \frac{\nu^{\mathrm{S}}}{N_m^{\mathrm{S}}} \iint d\mathbf{r}_\perp \chi^{(2)} \left(\mathbf{r}_\perp, -2\nu^{\mathrm{F}}; \nu^{\mathrm{F}}, \nu^{\mathrm{F}}\right) . \left[\mathbf{e}_{m\perp}^{\mathrm{S}} \left(\mathbf{r}_\perp\right) - \mathbf{e}_{mz}^{\mathrm{S}} \left(\mathbf{r}_\perp\right)\right]. \tag{2.5.22}$$

On the left hand side of Eq. (2.5.21), spatial partial derivative indicates propagation in space, temporal derivative denotes the same in time while the last term denotes modal damping along propagation direction. The right hand side of the equation contains terms that couple the modes at FH and SH. Equation (2.5.21) can be easily adapted to continuous wave (CW) case by dropping the temporal dependance of the mode envelopes $\tilde{a}_m^{\{\mathrm{F,S}\}}(z,t)$. This gives us:

$$\frac{da_0^{\mathrm{F}}(z)}{dz} + \beta_0''^{\mathrm{F}} a_0^{\mathrm{F}}(z) = \iota \sum_m \gamma_m^{\mathrm{F}} \left\{a_0^{\mathrm{F}}(z)\right\}^\star a_m^{\mathrm{S}}(z) \exp\left(\iota \Delta\beta_m z\right),$$
$$\frac{da_{\mathrm{M}}^{\mathrm{S}}(z)}{dz} + \beta_{\mathrm{M}}''^{\mathrm{S}} a_{\mathrm{M}}^{\mathrm{S}}(z) = \iota \gamma_{\mathrm{M}}^{\mathrm{S}} \left\{a_0^{\mathrm{F}}(z)\right\}^2 \exp\left(-\iota \Delta\beta_{\mathrm{M}} z\right). \tag{2.5.23}$$

We would like to point out that in deriving the results expressed in Eqs. (2.5.21), we had approximated the mode envelope $\tilde{u}_m^{\{\mathrm{F,S}\}}(z,t)$ to be narrow band i.e. slowly varying in time [see Eq. (2.5.3)]. However, no such restriction was imposed upon the spatial evolution of $\tilde{u}_m^{\{\mathrm{F,S}\}}(z,t)$. Therefore, the mode envelope $a_m^{\{\mathrm{F,S}\}}(z)$ in Eqs. (2.5.23) does not suffer from any similar limitation in spatial domain

Another aspect worth pointing out in Eqs. (2.5.23) is that in lossless regime $\left(\beta_m''^{\{\mathrm{F,S}\}} = 0\right)$, the efficiency of interaction is determined by the amplitude of $\left|\gamma_m^{\{\mathrm{F,S}\}}\right|$ and $|\Delta\beta_m|$. While the former determines the strength with which the modes interact nonlinearly, the latter represents the momentum mismatch whose effect is to reverse the conversion cycle from one harmonic to another. In the latter case, the distance after which the energy conversion process reverses is known as coherence length which is defined as

$$\kappa_m = \frac{\pi}{|\Delta\beta_m|}. \tag{2.5.24}$$

Therefore, $\Delta\beta_m$ is a delimiting factor that restricts the nonlinearly interacting harmonics from full energy exchange. The effect of modal damping can be seen to reduce the interaction strength as it attenuates the mode along the propagation path until it negligibly reduces the overall effect of nonlinear interaction.

Analytical solution

The analytical solution of Eq. (2.5.23) can be obtained if the partial differential equations (PDE) could be decoupled. Most of the text books treat the coupled mode interaction presented in the foregoing section considering lossless structures wherein it is possible to arrive at simplified energy conservation relations known as Manley-Rowe relations [87, 102]. This allows Eqs. (2.5.23) to be decoupled and solved analytically. What is less talked about, however, is the existence of an analogous result in damped systems. In the following we explore the possibility of applying the same idea to the simplified CW system formulated in Eq. (2.5.23).

Without any loss of generality, we can simplify the analysis by assuming there exists only a single mode of order M at SH. Beginning from Eqs. (2.5.23), we can then arrive at the following relation by means of straightforward algebraic manipulations:

$$\begin{aligned}\frac{\partial}{\partial z}\left(\alpha^{\star}\left|a_0^{\mathrm{F}}(z)\right|^2+\left|a_{\mathrm{M}}^{\mathrm{S}}(z)\right|^2\right) &= -2\left(\alpha^{\star}\beta_0^{\prime\prime\mathrm{F}}\left|a_0^{\mathrm{F}}(z)\right|^2+\beta_{\mathrm{M}}^{\text{''}\mathrm{S}}\left|a_{\mathrm{M}}^{\mathrm{S}}(z)\right|^2\right)\\ &\quad -2\Im\{\alpha\}\,\gamma^{\star}\left\{a_0^{\mathrm{F}}(z)\right\}^2\left\{a_{\mathrm{M}}^{\mathrm{S}}(z)\right\}^{\star}\exp(\iota\Delta\beta_{\mathrm{M}}z), \end{aligned} \quad (2.5.25)$$

where the mode overlap coefficients at FH and SH [Eq. (2.5.22)] are related by the complex constant α as

$$\alpha=\frac{\gamma_{\mathrm{M}}^{\mathrm{S}}}{\gamma_0^{\mathrm{F}}}. \quad (2.5.26)$$

We can now attempt to understand the ramifications of Eq. (2.5.25). In lossless case, both the mode vector $\beta_m^{\{\mathrm{F,S}\}}$ and constant α are real, making the right hand side of Eq. (2.5.25) vanish. This leaves us with the well-known Manley-Rowe relations [87] which establish the conservation of total power in the waveguide at any point z along the propagation direction. The existence of losses, however, does not allow the derivation of a similar identity that could be then used to decouple the set of Eqs. (2.5.23). To the best of our knowledge, the analytical solution for the lossy media is known to exist only in a special case when $\beta_0^{\prime\prime\mathrm{F}}=\beta_m^{\prime\prime\mathrm{S}}$ [103]. However, it is too restrictive an assumption to rely on in dissipative systems which we are going to consider. Therefore, an analytical solution to Eq. (2.5.23) will not be sought and we will be relying on numerical techniques for solutions.

Figures (2.5.1) plot some examples of the solution of Eqs. (2.5.23) for select values of $\Delta\beta$, $\gamma^{\{\mathrm{S}\}}$ and $\beta^{\prime\prime\mathrm{S}}$ when there is no incident SH at the input. In Fig. (2.5.1)(a), we find

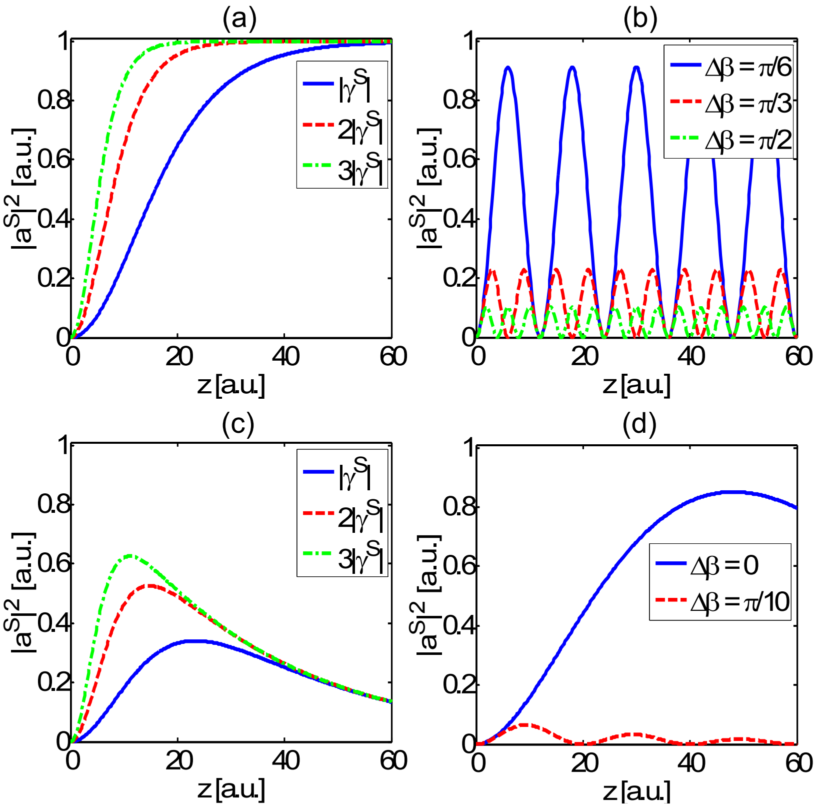

Figure 2.5.1: Evolution of SH power $\left|a^{\mathrm{S}}(z)\right|^2$ in various cases. (a) Varying $\left|\gamma^{\mathrm{S}}\right|$ and fixed $\Delta\beta = \beta''^{\mathrm{S}} = 0$. (b) Varying $\Delta\beta$ and fixed γ^{S}, $\beta''^{\mathrm{S}} = 0$. (c) Varying γ^{S} and fixed $\Delta\beta = 0$, $\beta''^{\mathrm{S}} = 15$. (c) Varying $\Delta\beta$ and fixed γ^{S}, $\beta''^{\mathrm{S}} = 15$. β''^{S} is defined on the same unit scale as the propagation axis z in Figures

]

SH to asymptotically achieve all the input pump power thanks to an absence of phase-mismatch and propagation loss. However, the relative amplitude of γ^{S} determines how quickly the total energy transfer takes place. Next we highlight the influence of phase mismatch on maximum power converted and oscillation of energy in Fig. 2.5.1(b). The last two cases are similar except that losses are now present which further deteriorate the efficiency of nonlinear energy conversion in Figs. 2.5.1(c) and (d).

In Ch. 5, we will consider the problem of SH generation in plasmonic slot waveguides where the results derived in this section would be extensively put to use.

2.6 Surface Plasmon Polaritons

Surface plasmon polaritons (SPP) are the surface charge oscillations coupled to the incident electromagnetic field at the interface between metallic and dielectric media. Depending upon the broad categorization of geometry of the metal-dielectric structure into a planar interface and a closed form object, such as a spherical particle, SPP acquire peculiar features adapting to each of the two scenarios. The SPP supported by the former structure is guided along the interface and referred generally in the literature and specifically in this treatise as the propagating SPP (PSPP). Whereas in the latter case, SPP appear in the form of static charge oscillations and shall be distinguished henceforth as the localized SPP (LSPP). In the following subsections we present necessary derivations and discussions on the essential properties of each of the two to an extent that is necessary to understand the work presented in the following chapters.

2.6.1 Propagating SPP

In media that can be defined over a 2D plane, it is known that the electromagnetic waves can be decomposed into TM and TE polarizations whereby the electric field components are parallel and perpendicular to the plane of propagation respectively [88,104]. Henceforth we will investigate both TM and TE polarizations to find the electromagnetic mode guided along the interface between metal ($\Re\left\{\varepsilon_{\mathrm{r}}(\nu)\right\} < 0$) and dielectric ($\Re\left\{\varepsilon_{\mathrm{r}}(\nu)\right\} > 1$), both of which are considered isotropic here. Beginning with the former, we define the following ansatz for the out of plane component of the magnetic field (Fig. 2.6.1):

$$H_y(x,z,\nu) = \begin{cases} H_0 \exp\left(-k_{\mathrm{d}}(\nu)\,x\right) \exp\left(\iota\beta(\nu)\,z\right), & x > 0 \\ H_0 \exp\left(k_{\mathrm{m}}(\nu)\,x\right) \exp\left(\iota\beta(\nu)\,z\right), & x < 0 \end{cases}, \tag{2.6.1}$$

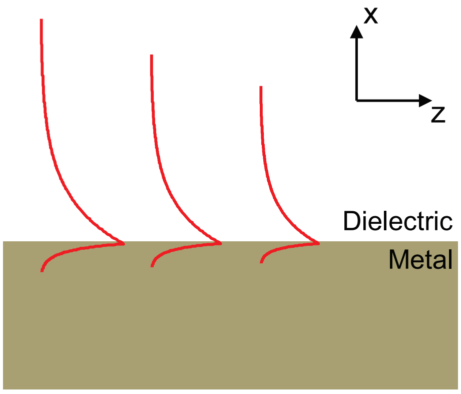

Figure 2.6.1: Schematic sketch showing the propagation of a PSPP mode along the interface between metal and dielectric.

where H_0 is some constant, $\beta\left(\nu\right)$ is the complex wave number of the mode and $k_{\mathrm{d}}\left(\nu\right)$ in dielectric $\left(x>0\right)$ and $k_{\mathrm{m}}\left(\nu\right)$ in metal $\left(x<0\right)$ is related to $\beta\left(\nu\right)$, vacuum wave number $k_0\left(\nu\right)=2\pi\nu/c$ and material parameters $\varepsilon_{\mathrm{d}}\left(\nu\right)$ and $\varepsilon_{\mathrm{m}}\left(\nu\right)$ for dielectric and metal respectively as

$$k_{\{\mathrm{d,m}\}}\left(\nu\right)=\sqrt{\beta^2\left(\nu\right)-k_0^2\left(\nu\right)\varepsilon_{\{\mathrm{d,m}\}}\left(\nu\right)}. \tag{2.6.2}$$

Since we are seeking a mode that decays evanescently in both media across the interface, $\Re\left\{k_{\{\mathrm{d,m}\}}\left(\nu\right)\right\}$ should be positive in Eq. (2.6.1). The electric field components of the mode can easily be obtained through the Maxwell's curl equation for the magnetic field [Eq. (2.1.4)] as

$$E_x\left(x,z,\nu\right)=\frac{H_0\beta\left(\nu\right)}{\nu\varepsilon_0}\exp\left(\iota\beta\left(\nu\right)z\right)\begin{cases}\frac{1}{\varepsilon_{\mathrm{d}}\left(\nu\right)}\exp\left(-k_{\mathrm{d}}\left(\nu\right)x\right), & x>0\\ \frac{1}{\varepsilon_{\mathrm{m}}\left(\nu\right)}\exp\left(k_{\mathrm{m}}\left(\nu\right)x\right), & x<0\end{cases} \tag{2.6.3}$$

and for $E_z\left(x,y,\nu\right)$:

$$E_z\left(x,z\nu\right)=\frac{H_0}{\nu\varepsilon_0}\exp\left(\iota\beta\left(\nu\right)z\right)\begin{cases}-\frac{k_{\mathrm{d}}\left(\nu\right)}{\varepsilon_{\mathrm{d}}\left(\nu\right)}\exp\left(-k_{\mathrm{d}}\left(\nu\right)x\right), & x>0\\ \frac{k_{\mathrm{m}}\left(\nu\right)}{\varepsilon_{\mathrm{m}}\left(\nu\right)}\exp\left(k_{\mathrm{m}}\left(\nu\right)x\right), & x<0\end{cases}. \tag{2.6.4}$$

In order to solve for the wave number $\beta\left(\nu\right)$, we apply the boundary conditions obtained in Eqs. (2.1.10) and (2.1.11) on the tangential component of electric field $E_x\left(x,z,\nu\right)$ [Eq. (2.6.3)] and magnetic field $H_z\left(x,y,\nu\right)$ at the interface $\left(y=0\right)$. We note that the latter condition is already satisfied in the definition of ansatz in Eq. (2.6.1). An application of the former leads us to

$$\frac{k_{\mathrm{d}}(\nu)}{k_{\mathrm{m}}(\nu)} = -\frac{\varepsilon_{\mathrm{d}}(\nu)}{\varepsilon_{\mathrm{m}}(\nu)}. \tag{2.6.5}$$

We observe that Eq. (2.6.5) can be valid only if $\Re[\varepsilon_{\mathrm{m}}(\nu)] < 0$ given the ansatz in Eq. (2.6.1). Therefore, angular frequency ν of the electromagnetic wave has to be larger than the bulk plasma frequency of the metal. Solving for $\beta(\nu)$ in Eq. (2.6.5) yields:

$$\beta(\nu) = k_0 \sqrt{\frac{\varepsilon_{\mathrm{d}}(\nu)\,\varepsilon_{\mathrm{m}}(\nu)}{\varepsilon_{\mathrm{d}}(\nu) + \varepsilon_{\mathrm{m}}(\nu)}}. \tag{2.6.6}$$

In the light of Eqs. (2.6.2) and (2.6.6), following conclusions can be drawn about the dispersion $\beta(\nu)$ of the mode:

1. The real part $\beta'(\nu) = \Re[\beta(\nu)]$ is always larger than the dielectric wave number $k_0(\nu)\sqrt{\varepsilon_{\mathrm{d}}(\nu)}$. As a result, any incident illumination will fail to excite a PSPP mode at the surface unless the momentum-mismatch between the wave in the dielectric medium and $\beta(\nu)$ is compensated by artificial means such as grating vector (see Ref. [2] for details).

2. $\beta'(\nu)$ reaches a maximum value when the real part of the denominator in Eq. (2.6.6) is minimum. For the special case of a Drude metal and a dispersion-less dielectric, it can be defined in terms of the bulk plasma frequency as

$$\nu_{\mathrm{PSPP}} = \frac{\nu_{\mathrm{p}}}{\sqrt{1+\varepsilon_{\mathrm{d}}}}, \tag{2.6.7}$$

where ν_{P} is the bulk plasma frequency of the metal whose permittivity is defined together with the damping frequency ν_γ as:

$$\varepsilon_{\mathrm{m}}(\nu) = 1 - \frac{\nu_{\mathrm{p}}^2}{\nu(\nu_\gamma \iota + \nu)}. \tag{2.6.8}$$

The condition defined in Eq. (2.6.7) is usually referred as the resonance of PSPP. As a matter of fact, in the limit of negligible damping ($\Im[\varepsilon_{\mathrm{m}}(\nu)] = 0$), the wave number $\beta'(\nu)$ approaches infinity at resonance and the group velocity becomes zero. The PSPP thus acquires the character of a standing wave and the distinction we had set between PSPP and LSPP vanishes. However, in realistic metallic media such a negligible damping limit is never reached. In fact, metallic dissipation causes a steady increase in mode damping as can be observed in Fig. 2.6.2(b). Therefore, for all practical purposes, we can overlook the ramifications of operating in the extreme limit of loss-less metals.

3. When $\beta'(\nu)/k_0$ becomes smaller than $\sqrt{\varepsilon_{\mathrm{d}}(\nu)}$, $k_{\mathrm{d}}(\nu)$ becomes predominantly imaginary. As a result, the wave can be said to have lost its evanescent character in the dielectric half-space in Eqs. (2.6.1), (2.6.3) and (2.6.4). Therefore, the frequency when $\beta'(\nu)/k_0$ becomes equal to $\sqrt{\varepsilon_{\mathrm{d}}(\nu)}$ is usually referred as the mode cut-off frequency. Note that the cut-off frequency is smaller than the bulk plasma frequency beyond which the mode definition becomes invalid as already discussed with reference to Eq. (2.6.5).

Figure 2.6.2 plots the frequency dispersion of wave number $\beta(\nu)$ of a PSPP mode guided at the interface between air and silver (Ag) whose experimentally determined values of the permittivity is used [105]. For smaller frequencies in Fig. 2.6.2(a), we find $\beta'(\nu)$ to be linear as it should only be marginally larger than the dielectric wave number $k_0\sqrt{\varepsilon_{\mathrm{d}}(\nu)}$. However, as it proceeds to the resonance frequency, $\beta'(\nu)$ steadily increases until it reaches the maximum as discussed above. Thereafter, it undergoes back-bending until it meets with the dielectric wave number $k_0\sqrt{\varepsilon_{\mathrm{d}}(\nu)}$ beyond which it loses its evanescent character as already discussed. It should be noted that the possibility to achieve sub-wavelength confinement through PSPP comes from the fact that modes are allowed to decay evanescently in both media forming the interface. In conventional waveguides formed either with perfect metals ($\Re\{\varepsilon_{\mathrm{m}}\} \approx -\infty$), dielectrics or both, there is always a requirement for a dielectric *core* in which the mode maintains non-evanescent, oscillatory character (see for instance Refs. [61,91,104]). It is the core whose dimensions cannot be made smaller than the wavelength which prohibits conventional waveguides from guiding modes at scale smaller than the wavelength.

We will now finally address the problem of TE surface modes sustained by the geometry shown in Fig. 2.6.1. Similar to Eq. (2.6.1), we propose the following ansatz for the independent E_y component of electric field:

$$E_y(x,z,\nu) = \begin{cases} E_0 \exp(-k_{\mathrm{d}}(\nu)\,x)\exp(\iota\beta(\nu)\,z)\,, & x > 0 \\ E_0 \exp(k_{\mathrm{m}}(\nu)\,x)\exp(\iota\beta(\nu)\,z)\,, & x < 0 \end{cases}, \tag{2.6.9}$$

where $k_{\{\mathrm{m,d}\}}(\nu)$ and $\beta(\nu)$ have the same definition and relation as already discussed with respect to Eq. (2.6.2). The corresponding magnetic field components are obtained likewise from the Maxwell's curl equation [Eq. (2.1.4)] for electric field as

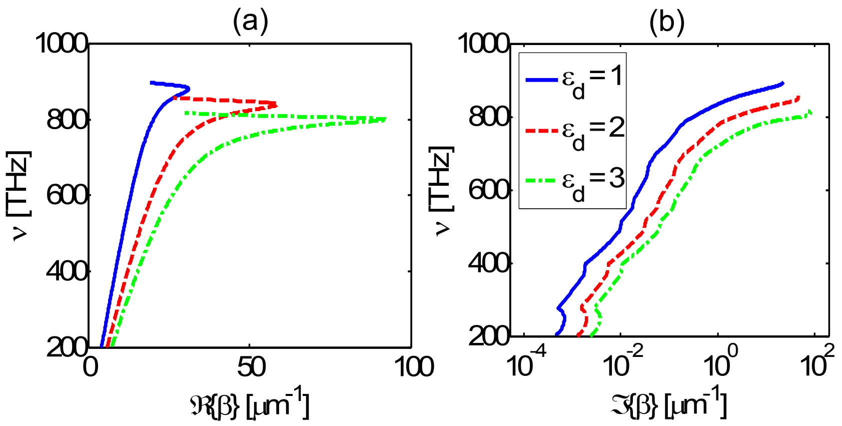

Figure 2.6.2: Dispersion of the real (a) and imaginary (b) parts of the propagation wave number $\beta\,(\nu)$ of PSPP using the experimentally obtained values of the permittivity of Ag [105] and dispersion less dielectric medium of permittivity $\varepsilon_{\rm d}$.

$$H_z\,(x, z, \nu) = \frac{\iota E_0}{\nu\mu_0}\exp\left(\iota\beta\,(\nu)\,z\right)\begin{cases} k_{\rm d}\,(\nu)\exp\left(-k_{\rm d}\,(\nu)\,x\right), & x > 0 \\ -k_{\rm m}\,(\nu)\exp\left(k_{\rm m}\,(\nu)\,x\right), & x < 0 \end{cases} \qquad (2.6.10)$$

and

$$H_x\,(x, y\nu) = -\frac{E_0\beta\,(\nu)}{\nu\mu_0}\exp\left(\iota\beta\,(\nu)\,z\right)\begin{cases} \exp\left(-k_{\rm d}\,(\nu)\,x\right), & x > 0 \\ \exp\left(k_{\rm m}\,(\nu)\,x\right), & x < 0 \end{cases}. \qquad (2.6.11)$$

As before, we subject the tangential components of the electric and magnetic fields to the boundary conditions Eqs. (2.1.10) and (2.1.11). This leads us to:

$$E_0\left[k_{\rm m}\,(\nu) + k_{\rm d}\,(\nu)\right] = 0. \qquad (2.6.12)$$

Equation (2.6.12) cannot be satisfied until $\Re\left\{k_{\{\rm m,d\}}\,(\nu)\right\}$ in either metal or dielectric is allowed to be negative. This however contradicts our earlier stipulation in the ansatz [Eq. (2.6.9)] that both of them should be positive. Therefore, there is no surface mode solution for TE polarization and PSPP exists only for TM polarization. This also corresponds to the intuitive requirement for a non-vanishing component of electric field along the propagation direction in order to drive surface electrons.

To conclude this section, we would like to point out that the basic PSPP example presented in the foregoing pertains only to the simplest case. There are more complicated cases formed by more complex metal dielectric interfaces, not all of which are

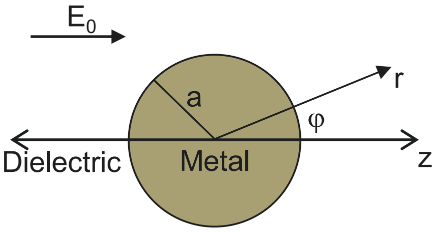

Figure 2.6.3: Geometrical sketch of a metallic sphere in dielectric space.

known to be analytically considerable. However, the simplest case still shares the basic features, advantages and limitations that are associated with PSPP modes found in complex waveguides. Therefore, we leave the discussion specific to a particular plasmonic waveguide geometry to those sections where they will be used.

2.6.2 Localized SPP

In finite metallic objects surrounded by the dielectric media (and vice versa), the interaction with an incident monochromatic plane wave can induce a resonant scattering response from the structure. For spherical particles, a rigorous solution was presented by Gustav Mie in 1908 that described the field scattered by the object as a superposition of vector spherical harmonics [7, 8]. While the theory is fully sufficient to account for the scattering of light by spheres of any size, it is physically more instructive to consider the problem in terms of the so-called quasi-static (QS) approximation for spheres significantly smaller than the incident wavelength. As the size of the problem becomes sufficiently small (roughly less than $\lambda/10$), the retardation effect of the incident wave can be neglected. Mathematically, this amounts to approximating the time derivative terms in Eq. (2.1.1) to be negligible which causes a decoupling of electric and magnetic fields [106]. This allows writing Maxwell's curl equations [Eq. (2.1.1)] as

$$\nabla \times \mathbf{E}(\mathbf{r}) = 0, \qquad \nabla \times \mathbf{H}(\mathbf{r}) = 0. \tag{2.6.13}$$

The electric field in Eq. (2.6.13) can be written in terms of the scalar potential $\Phi(\mathbf{r})$ as

$$\mathbf{E}(\mathbf{r}) = -\nabla\Phi(\mathbf{r}),$$

which further simplifies the problem to solving for the potential according to Laplace equation:

$$\nabla^2\Phi\left(\mathbf{r}\right)=0. \tag{2.6.14}$$

Equation (2.6.14) is valid in each homogeneous medium making up the geometry. The interface between two media are dealt with through appropriate boundary conditions as we shall see shortly. Now let us consider a spherical particle of radius a, made up of metal of permittivity $\varepsilon_{\mathrm{m}}\left(\nu\right)$, embedded in a dielectric medium of permittivity $\varepsilon_{\mathrm{d}}\left(\nu\right)$ and illuminated by an incoming wave mono-chromatic of frequency ν and electric field amplitude E_0 polarized along the z-axis as shown in Fig. 2.6.3. As we are approximating the problem in quasi-static, the temporal response of the medium can be approximated as complex constants ε_{m} and ε_{d} respectively. Amplitude of the incident mono-chromatic electric field is expressed as

$$\mathbf{E}_{\mathrm{in}}=E_0\hat{\mathbf{a}}_z. \tag{2.6.15}$$

Considering Eq. (2.6.13), we can write down the potential of the incident field in spherical symmetry as

$$\Phi_{\mathrm{in}}\left(r,\theta\right)=-E_0z=-E_0r\cos\left(\theta\right). \tag{2.6.16}$$

In order to solve for the field scattered by the sphere it is convenient to consider spherical coordinates in order to take advantage of the azimuthal symmetry of the geometry. In this case, the general solution of the Laplace equation [Eq. (2.6.14)] is written as [88]:

$$\Phi\left(r,\theta\right)=\Sigma_{l=0}^{\infty}\left[A_lr^l+B_lr^{-(l+1)}\right]P_l\left(\cos\theta\right) \tag{2.6.17}$$

where $P_l\left(\cos\theta\right)$ is the Legendre polynomial of order l and θ is the angle between the position vector $\mathbf{r}$ and the z-axis (Fig. 2.6.3). Since the factor $r^{-(l+1)}$ becomes infinite when $r=0$ inside the sphere, B_l has to be zero within the sphere. In the same vein, the scattered field outside the sphere should reduce to zero as the radius r goes to infinity leaving behind only the incident field. This implies:

$$\lim_{r\to\infty}\Phi\left(r,\theta\right)=-E_0z=-E_0r\cos\left(\theta\right). \tag{2.6.18}$$

Therefore, $B_1=-E_0$ and for all $l\neq1$ we have $B_l=0$. With this we can rewrite Eq. (2.6.17) for the two cases of within $(r<a)$ and without $(r>a)$ the metallic sphere as

$$\Phi\left(r,\theta\right)=\begin{cases}\Sigma_{l=0}^{\infty}A_{l}r^{l}P_{l}\left(\cos\theta\right), & r<a\\ -E_{0}r\cos\left(\theta\right)+\Sigma_{l=0}^{\infty}C_{l}r^{-(l+1)}P_{l}\left(\cos\theta\right), & r>a\end{cases}. \tag{2.6.19}$$

For the rest of coefficients A_l and C_l, we apply the boundary conditions at the interface $r = a$. The boundary conditions for the continuity of the tangential component of electric field and the normal component of electric displacement [Eq. (2.1.10)] are translated into scalar potential as

$$\begin{aligned}-\frac{1}{a}\frac{\partial\Phi\left(r,\theta\right)}{\partial\theta}\bigg|_{r=a^{-}} &= -\frac{1}{a}\frac{\partial\Phi\left(r,\theta\right)}{\partial\theta}\bigg|_{r=a^{+}},\\ -\varepsilon_{0}\varepsilon_{\mathrm{m}}\frac{\partial\Phi\left(r,\theta\right)}{\partial\theta}\bigg|_{r=a^{-}} &= -\varepsilon_{0}\varepsilon_{\mathrm{d}}\frac{\partial\Phi\left(r,\theta\right)}{\partial\theta}\bigg|_{r=a^{+}}.\end{aligned} \tag{2.6.20}$$

A straightforward application of Eqs. (2.6.20) gives us the following result for potential inside and outside the sphere:

$$\Phi\left(r,\theta\right)=\begin{cases}\frac{3\varepsilon_{\mathrm{d}}}{\varepsilon_{\mathrm{m}}+2\varepsilon_{\mathrm{d}}}E_{0}r\cos\theta, & r<a\\ -E_{0}r\cos\theta+\frac{\mathbf{p.r}}{4\pi\varepsilon_{0}\varepsilon_{\mathrm{m}}r^{3}}, & r>a\end{cases}. \tag{2.6.21}$$

In Eq. (2.6.21) above, the dipole moment vector $\mathbf{p}$ is defined in terms of the polarizability α as

$$\mathbf{p}=\varepsilon_{0}\varepsilon_{\mathrm{m}}\alpha\mathbf{E}_{0}, \tag{2.6.22}$$

where

$$\alpha=4\pi a^{3}\frac{\varepsilon_{\mathrm{m}}-\varepsilon_{\mathrm{d}}}{\varepsilon_{\mathrm{m}}+2\varepsilon_{\mathrm{d}}}. \tag{2.6.23}$$

According to Eq. (2.6.21), the total field outside the sphere in Eq. (2.6.21) is a superposition of the incident field and the field radiated by a dipole induced inside the sphere with a moment proportional to the incident field's amplitude [Eq. (2.6.22)]. We now note the fact that the permittivities of metal and dielectric in Eqs. (2.6.21,2.6.22,2.6.23) parametrically depend upon the frequency ν_0 of the incident plane wave. Therefore, the polarizability α [Eq. (2.6.23)] of the sub-wavelength sphere exhibits a resonant response when the real part of the denominator in Eq. (2.6.23) is minimum. This is known as the dipole SPP resonance of the metallic sphere. However, for the purpose of distinguishing it from the PSPP resonance discussed in the preceding section we shall refer to it sim-

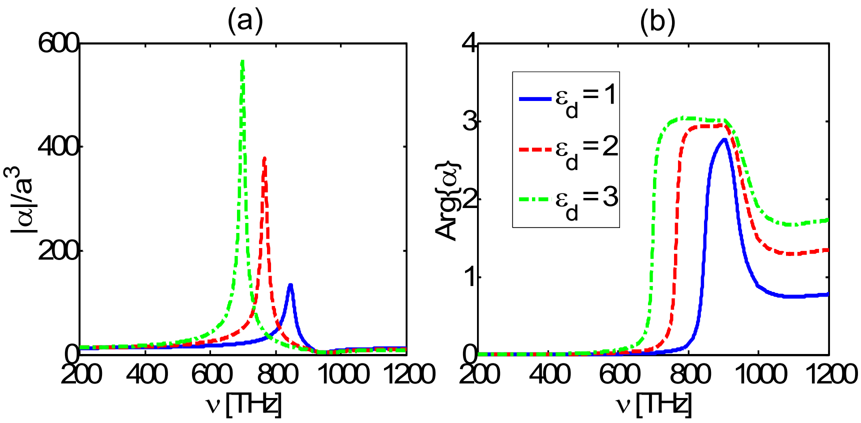

Figure 2.6.4: Normalized magnitude (a) and phase (b) of the polarizability α of a Ag sphere in a dispersion less dielectric medium of permittivity ε_{d}.

ply as LSPP resonance. At resonance, the incident field couples strongly to the surface charges causing it oscillate together. The resonance condition is expressed as

$$\Re\left\{\varepsilon_{\mathrm{m}}\left(\nu_0\right)\right\}=-2\varepsilon_{\mathrm{d}}\left(\nu_0\right). \tag{2.6.24}$$

Figure 2.6.4 shows the dispersion of the absolute value and phase of the polarizability $\alpha(\nu)$ for a Ag sphere [105] in dispersion less dielectric media. Once again, for a Drude metal whose permittivity is defined previously in Eq. (2.6.8) and dispersion-less dielectric of permittivity ε_{d}, it can be shown that the resonance condition in Eq. (2.6.24) is satisfied at:

$$\nu_{\mathrm{LSPP}}=\frac{\nu_{\mathrm{P}}}{\sqrt{1+2\varepsilon_{\mathrm{d}}}}. \tag{2.6.25}$$

We can now finally write the expression for the total electric field as

$$\mathbf{E}\left(\mathbf{r}\right)=-\nabla\Phi\left(r\right)=\begin{cases}\frac{3\varepsilon_{\mathrm{d}}}{\varepsilon_{\mathrm{m}}+2\varepsilon_{\mathrm{d}}}\mathbf{E}_0, & r<a\\ \mathbf{E}_0+\frac{3\mathbf{n}[\mathbf{n}.\mathbf{p}]-\mathbf{p}}{4\pi\varepsilon_0\varepsilon_{\mathrm{d}}}.\frac{1}{r^3}, & r>a\end{cases}, \tag{2.6.26}$$

where $\mathbf{n}$ is the unit vector along the position vector $\mathbf{r}$. Therefore, we find the electric fields in the near-field to undergo resonant enhancement when the condition in Eq. (2.6.24) is satisfied. This allows the sub-wavelength metallic spheres to act as simple yet effective antenna elements for focusing light at optical frequencies.

Before leaving, we would like to point out that the simplest example of PSPP considered here is to provide a foundation on which more complex plasmonic waveguiding geometries to appear later can be understood. As such, we would not treat the referential metal dielectric interface anymore. However, the basic insights derived from this case will guide our qualitative eye in understanding the behavior of more complex structures.

Likewise, the scattering of light by sub-wavelength sphere considered here serves as the simplest referential example of the antenna focusing of light by plasmonic particles. Cases such as infinitely extended metallic cylinder or more complicated geometries like core-shells, spheroids, etc. have also been analytically studied but due to space constraints we would have to content with just citing their unique results from the available literature wherever required. Qualitative meaning once again will be built upon the insight we gained in this section from the example of a spherical scatterer.

2.7 Concluding remarks

To sum up, we presented in this chapter the basic framework of reciprocity relations formulated on top of bulk Maxwell's Equations Using those results, we further derived the impedance definition between waveguiding interfaces and the interaction of modes coupled through second order nonlinear channels. At the very end, we went back yet again to Maxwell's equations to establish fundamental results for the most basic cases involving SPPs, both propagating at the interface between metal and dielectric media or localized thereon.

3 Antenna description of localized plasmonic resonances

3.1 Introduction

With the tools to analyze the behavior of modes in waveguides, we begin with the problem of localized resonance in plasmonic systems whose dimensions are much smaller than interacting light's wavelength. As we derived results in Sec. 2.6.2 for the referential example of a sphere, such cases can be described through quasi-static (QS) approximation whereby the propagation effects are ignored and the problem is solved by finding the static potential of the field scattered by the illuminated object [2,88]. This has led to extremely simple expressions offering insights into a multitude of particle geometries such as sphere, infinitely extended cylinders, ellipsoids, etc. While in general the resonance frequencies remain sensitive to the geometrical features of the particle, it was curiously shown that the quality factor (Q-factor) approaches a constant limit determined only by the material absorption of the particle irrespective of its shape at resonance [107]. This universal Q-factor, so to say, in QS limit is defined only in terms of material parameters as [107]:

$$Q = \pi \frac{\nu_0 \frac{\partial \varepsilon'_{\mathrm{m}}(\nu)}{\partial \nu}}{\varepsilon''_{\mathrm{m}}(\nu)}, \tag{3.1.1}$$

where ν_0 is the resonance frequency and $\varepsilon_{\mathrm{m}}(\nu) = \varepsilon'_{\mathrm{m}}(\nu) + \iota \varepsilon''_{\mathrm{m}}(\nu)$ is the complex permittivity of the metal.

With all its success, however, the aforementioned approach also presents a theoretical puzzle. As we saw in Sec. 2.6.2, QS approach allows us to treat the problem as static for all practical purpose. If the physical properties of a QS system can indeed be understood without considering wave dynamics, is it still possible to view the resonance of subwavelength systems through wave effects? In a previous study, a finite length metallic cylinder of dimensions much smaller than the incident wavelength was shown to sustain

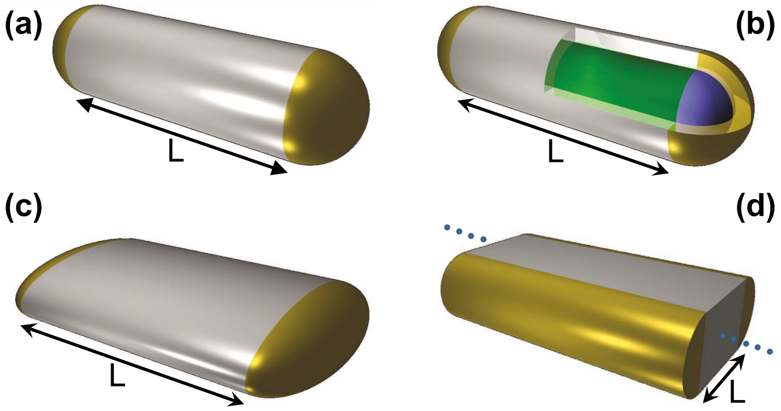

Figure 3.1.1: Schematic illustration of the FP antennas of length L considered in this chapter. (a) Sphere, (b) core-shell, (c) ellipsoid and (d) cylinder. The last one extends indefinitely along the direction indicated by dotted blue line. Notice that when L goes to zero, all the cavities collapse to familiar nano-particle geometries.

Fabry-Perot (FP) resonances of the PSPP mode excited by the incident radiation [108]. Since FP resonance is based on wave interference effect, it means that a system which is well within QS regime can still be described from a wave perspective.

To further motivate this problem, we refer to Figs. 3.1.1(a-d) which show circular, core-shell, elliptical and strip waveguides having hemispherical, half core-shell, semi-spheroidal and semi-circular terminations respectively. The response of these antennas can be easily predicted through FP description of the guided PSPP mode sustained by the respective waveguiding geometries (see for instance, Refs. [59, 60, 109]). If the length L of the waveguide is made vanishingly small, it is easy to see that we will recover particles made up of terminal caps in Fig. 3.1.1. The question arises whether the resonator model will still be applicable? If so, it can potentially provide us a unified way of looking at the response of plasmonic antennas and particles.

This becomes all the more interesting when we consider the fact that a QS approach can be applied only to simple particles possessing certain geometrical symmetry that lends the problem to analytical treatment. This makes it unlikely, if not outright impossible, to subject complex particles, such as those possessing asymmetric geometrical features, to analytical treatment under quasi-static formulation. If a semi-analytical FP model is indeed applicable to closed-form particles much like extended antenna geometries of Fig. (3.1.1), it can potentially provide a way to numerically investigate and design closed-form particles which are otherwise inaccessible or cumbersome to approach by means of theoretical methods.

In what follows, we attempt to answer this question. We will first formally present FP model and outline the general procedure. Then we will consider metallic sphere as a specific application in detail. Afterward, metallic core-shell, spheroidal and cylindrical geometries would be considered in the same vein. At last, we will apply our approach to a composite particle whose resonance cannot be predicted by means of a theoretical model.

3.2 Fabry-Perot model

To subject nano-particles to a treatment based on semi-analytical FP approach, we consider the antennas shown in Fig. 3.1.1. Each of these antennas support propagating SPP modes traveling along length L of the antenna between the caps. Antennas with symmetric mirrors respond resonantly whenever the following condition is satisfied:

$$\psi\left(\nu\right) = \beta'\left(\nu\right) L + \phi_{\mathrm{r}}\left(\nu\right) = n\pi. \tag{3.2.1}$$

In Eq. (3.2.1) above, $\beta'\left(\nu\right)$ is the real part of the complex mode vector $\beta\left(\nu\right)$ of the PSPP supported by the antenna, $\phi_{\mathrm{r}}\left(\nu\right)$ the reflected phase jump of the PSPP mode and n denotes the integer order of FP resonance. In the curious limit when the length L of the resonator becomes negligibly small, we regain the nanoparticle geometry. The resonance of the antenna, if the model remains valid, is then exclusively determined by the phase jump $\phi_{\mathrm{r}}\left(\nu\right)$ of the PSPP mode supported by the structure. Therefore, the antenna should respond resonantly whenever $\phi_{\mathrm{r}}\left(\nu\right)$ is equal to integer multiple of π. In the specific context of symmetric particles and symmetric illumination schemes, there should be additional requirement of n to be an odd integer in Eq. (3.2.1) because even values lead to symmetry forbidden modes. As the procedure remains the same for all the geometries shown in Fig. 3.1.1, we shall demonstrate our approach in detail only for the first case of sphere [Fig. 3.1.1(a)] before presenting results obtained in the same manner for other geometries.

Before we formally consider any specific example, it is instructive to clarify that the antenna approach presented here is demonstrated only to the point of predicting the frequencies of QS resonances. Additional properties of interest such as scattering response, induced polarization, absorption spectra etc. of the particle will not be considered. Since this is pretty much the beginning of a new way to predict the scattering response of plasmonic particles, we will be contented with establishing the fundamental possibility to correlate the resonances found in similar geometries but seen from different standpoints.

3.3 Sphere

We divide our discussion on spheres into a brief recap of the known QS formulation and the antenna model which we wish to demonstrate as an equivalent alternative.

Quasi-static model

As already discussed at length in Sec. 2.6.2, the scattering response of a sphere much smaller than the incident wavelength can be described in QS limit to be the response of an induced electric dipole. For a sphere made up of metal of permittivity $\varepsilon_{\mathrm{m}}(\nu)$ and surrounded by a dielectric of permittivity $\varepsilon_{\mathrm{d}}(\nu)$, the induced polarizability $\alpha(\nu)$ can be described as

$$\alpha(\nu) = 4\pi a^3 \frac{\varepsilon_{\mathrm{m}}(\nu) - \varepsilon_{\mathrm{d}}(\nu)}{\varepsilon_{\mathrm{m}}(\nu) + 2\varepsilon_{\mathrm{d}}(\nu)}. \tag{3.3.1}$$

The resonance of the electric dipole induced inside the sphere is described by the Fröhlich condition [Eq. (2.6.25)] and the associated mode is called LSPP of the metallic sphere [2]. This is as much as needed to be understood in order to follow the proceedings of this chapter.

Antenna model

In order to solve the resonance problem of sphere through Eq. (3.2.1), we begin by finding the guided mode supported by the metallic cylinder surrounded by a dielectric medium as shown in Fig. 3.1.1(a). The earliest known trace of this problem appears to be the work of Sommerfeld in which he considered the problem of metallic cylinders of finite conductivity in microwave regime [110]. In recent years, however, the problem has received increased attention after it came to be known that in THz regime these cylinders act as low-dispersion and low-loss waveguides (for instance, see Refs. [111–113]). Here we shall focus our attention on the results relevant to our discussion on antennas operating near plasma frequency and formed using these cylinders within quasi-static regime only.

By considering cylindrical symmetry, it is possible to analytically find the modes guided by the structure. A metallic cylinder of given radius a, in general, is host to a myriad of guided modes identified according to their azimuthal order l. It has been shown that in the limit when the radius a becomes sufficiently small compared to the wavelength, all azimuthal modes for $|l| \geq 2$ experience cut-off [114]. On the other hand, the mode with $|l| = 1$ azimuthal dependance [Fig. 3.3.1(b)] has its propagation wave number $\beta_l(\nu)$

approach the free-space propagation number $k = 2\pi/\lambda$ of the surrounding dielectric medium accompanied by a simultaneous delocalization of the modal fields. Therefore, the resonance generated by this mode, if at all, will necessarily be delocalized. However, the characteristic of QS resonance is to localize the fields and not the other way around. Therefore, this mode has to have negligible effect in driving the resonance response of sphere in QS limit.

As for the the azimuthally symmetric fundamental TM_0 mode ($l = 0$), it undergoes increased localization caused by the corresponding increase in its propagation wave number $\beta_l(\nu)$ with increasing frequency. Any resonance brought about by this mode should also be localized, meeting with our expectation of a QS resonance of the sphere. Therefore, if our resonator model has to correspond with the QS scattering of sphere, the azimuthally symmetric fundamental TM_0 mode should determine the resonant response of the antenna in QS regime.

By a straightforward application of the boundary conditions at the metal-dielectric interface, the dispersion of the TM_0 mode can be found to be given by the following transcendental equation [115]:

$$\frac{K_0\left[p_{\mathrm{d}}(\nu)\,a\right] I_1\left[p_{\mathrm{m}}(\nu)\,a\right]}{K_1\left[p_{\mathrm{d}}(\nu)\,a\right] I_0\left[p_{\mathrm{m}}(\nu)\,a\right]} = -\frac{\varepsilon_{\mathrm{d}}(\nu)\,p_{\mathrm{m}}(\nu)}{\varepsilon_{\mathrm{m}}(\nu)\,p_{\mathrm{d}}(\nu)}, \tag{3.3.2}$$

where I_n and K_n being the modified Bessel functions of first and second kind of order n and the transverse wave number $p_{\mathrm{m,d}}(\nu)$ defined in metal $[\varepsilon_{\mathrm{m}}(\nu)]$ and dielectric $[\varepsilon_{\mathrm{d}}(\nu)]$ as

$$p_{\mathrm{m,d}}(\nu) = \sqrt{\beta^2(\nu) - k_0^2(\nu)\,\varepsilon_{\mathrm{m,d}}(\nu)}. \tag{3.3.3}$$

The distribution of the independent azimuthal component of the magnetic field is given again in terms of the modified Bessel functions as

$$H_\phi(\rho,\nu) = \begin{cases} \frac{I_1(p_{\mathrm{m}}(\nu)\rho)}{I_1(p_{\mathrm{m}}(\nu)a)}, & \rho < a \\ \frac{K_1(p_{\mathrm{m}}(\nu)\rho)}{K_1(p_{\mathrm{m}}(\nu)a)}, & \rho > a \end{cases}. \tag{3.3.4}$$

To solve the antenna problem defined in Eq. (3.2.1), we consider a silver cylinder of radius $a = 10\,\mathrm{nm}$ surrounded by a homogeneous and isotropic dielectric medium. Metallic dispersion is described by the experimentally measured values [105] while the dielectric medium is assumed to be dispersion-less without any loss of generality. The terminal caps of the cylinder are also taken to be hemispheres of the same radius as that of the cylinder. Therefore, the radius of the corresponding sphere in our case is the same

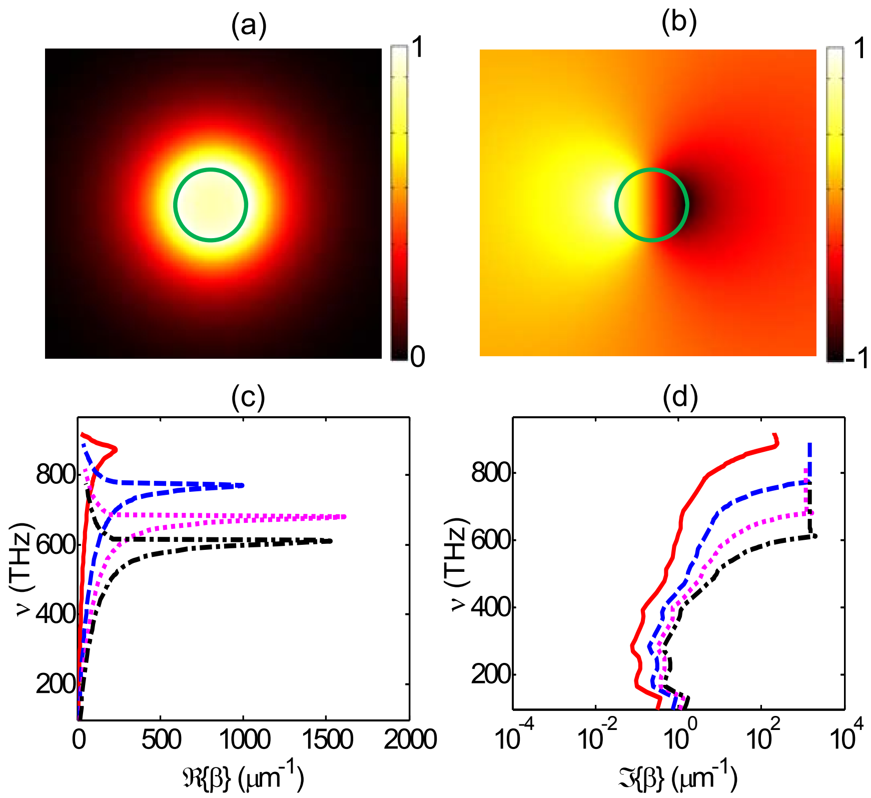

Figure 3.3.1: Electric field component parallel to the propagation direction of the fundamental TM$_0$ (a) and TM$_1$ (b) mode of a Ag cylinder in air with a radius of 10nm at $\nu = 500\,\mathrm{THz}$. Real (c) and imaginary (d) part of the modal wave number $\beta(\nu)$ of the fundamental TM$_0$ mode for select values of the permittivity ε_d of the surrounding medium: $\varepsilon_\mathrm{d} = 1$ (solid red), $\varepsilon_\mathrm{d} = 2.8$ (dashed blue), $\varepsilon_\mathrm{d} = 5.4$ (dotted magenta), $\varepsilon_\mathrm{d} = 9$ (dotted-dash black).

as that of the radius of the cylinder.

Figures 3.3.1(c) and (d) show dispersion of the fundamental TM$_0$ mode guided by the cylinder. The characteristic resonant behavior of the plasmonic mode is easily discerned in Fig. 3.3.1(c) followed by a back bending of the curve which is characterized by increased mode damping [Fig. 3.3.1(d)].

Having obtained modal dispersion, we move on to compute the complex modal reflection coefficient of the fundamental TM$_0$ mode at the hemispherical cap. For a metallic cylinder with flat termination, it is possible to solve the problem analytically by representing the field scattered in free-space through a superposition of the radiating Bessel fields in cylindrical basis [115]. In our case, however, the curvature of the hemispherical cap does not allow any straightforward analytical tool for solving the boundary conditions at the complex interface formed by the cylinder, hemispherical cap and free-space.

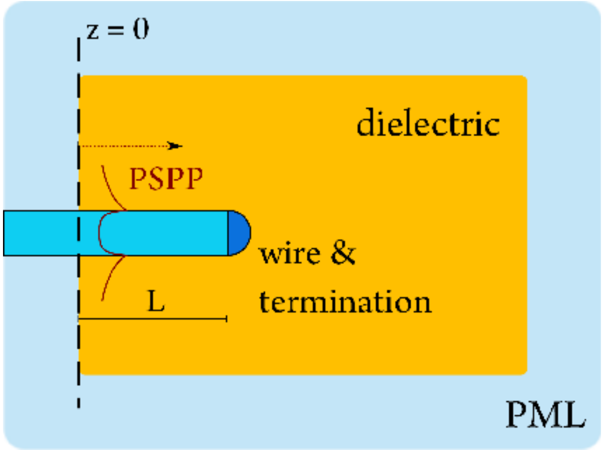

Figure 3.3.2: Schematic sketch of the simulation geometry used for obtaining modal reflection coefficient of the mode.

Therefore, we resort to numerically compute the reflection coefficient of the mode.

Figure 3.3.2 schematically sketches the 2D profile of the axially symmetric simulation scheme employed for obtaining the modal reflection coefficient. By using a commercial finite element method (FEM) based solver, Comsol Multiphysics, we launch the TM_0 mode onto the cylinder from $z = 0$ plane in the Figure The whole geometry is wrapped around with perfectly matched layers (PMLs) to absorb the back reflected mode as well as the scattered radiation from the hemispherical termination. Through a straightforward application of the mode orthogonality relations [Eq. (2.3.1)], we obtain the expression for the modal reflection coefficient:

$$r\left(\nu\right) = -\exp\left[-2\imath\beta\left(\nu\right)L\right]\frac{\int_0^\infty E_{\rho,0}\left(\rho,\nu\right)\left[H_{\phi,\mathrm{T}}\left(\rho,z=0,\nu\right)-H_{\phi,0}\left(\rho,\nu\right)\right]\rho d\rho}{\int_0^\infty E_{\rho,0}\left(\rho,\nu\right)H_{\phi,0}\left(\rho,\nu\right)\rho d\rho}. \tag{3.3.5}$$

In Eq. (3.3.5) above, $E_{\rho,0}\left(\rho,\nu\right)$ and $H_{\phi,0}\left(\rho,\nu\right)$ are the radial electric and azimuthal magnetic field components of the guided mode respectively which is launched at $z = 0$ plane whereas $H_{\phi,\mathrm{T}}\left(\rho,z,\nu\right)$ is the total azimuthal magnetic field in the simulation geometry. A glance at Eq. (3.3.5) reveals that the reflection coefficient $r\left(\nu\right)$ should be complex because of the complex nature of the field components of the TM_0 mode at optical frequencies owing in turn to the complex nature of the permittivity of metal (Ag) near the plasma frequency. Therefore, the phase $\phi_\mathrm{r}\left(\nu\right)$ in Eq. (3.2.1) would not be negligible and play a significant role in correctly predicting the FP resonances of the antenna. This is in contrast to antennas in the microwave regime where the electro-

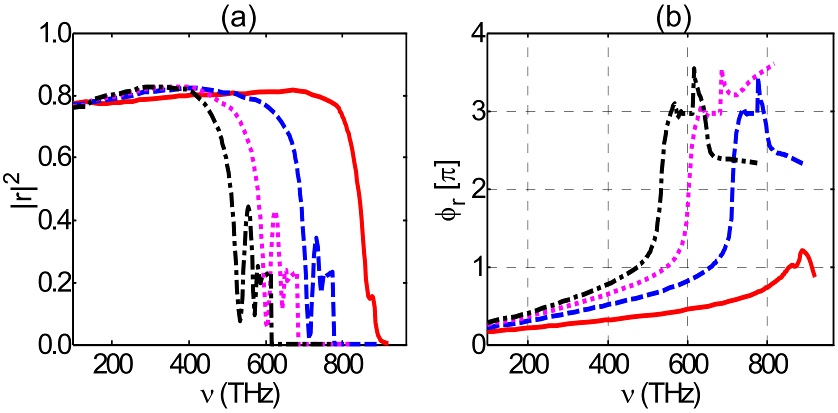

Figure 3.3.3: Amplitude (a) and unwrapped phase (b) of the modal reflection coefficient of TM_0 mode for various values of the permittivity ε_d of the surrounding medium: $\varepsilon_d = 1$ (solid red), $\varepsilon_d = 2.8$ (dashed blue), $\varepsilon_d = 5.4$ (dotted magenta), $\varepsilon_d = 9$ (dotted-dash black).

magnetic field components of the guided modes to a good approximation are either real or imaginary, thereby obviating the need to account for the reflection phase jump in predicting antenna resonances.

Figure 3.3.3 plots the amplitude and phase of the complex reflection coefficient. Since we are primarily interested in the problem of antenna resonance in the limit of vanishing length, we consider the phase jump $\phi_r(\nu)$ of the reflection coefficient in Fig. 3.3.3(b) only. It is seen to rise from small to large values as we move to higher frequencies which conforms well to the qualitative understanding we had while discussing Eq. (3.3.5) above. In fact, it continues to rise and even becomes equal and larger than π. As the antenna resonates when the round-trip phase is equal to integer multiple of 2π, we compare the resonance frequencies predicted by the antenna model with those suggested by QS theory [Eq. (3.3.1)] in Fig. 3.3.4 for various values of the permittivity ε_d of the surrounding dielectric medium. Evidently, there is a perfect agreement between the two which substantiates the proposition that localized plasmonic resonances under QS regime can be understood as FP resonances of the corresponding antenna of negligible length.

Before we move on to the next section, for completeness sake we take a brief moment to observe the behavior of reflection amplitude in Fig. 3.3.3(a). It is found to be relatively larger at smaller frequencies indicating the mirrors to be well-reflecting like metals. However, at larger frequencies it takes a downward slope even though we would have otherwise expected the PSPP mode to overlap even more poorly with the free-space

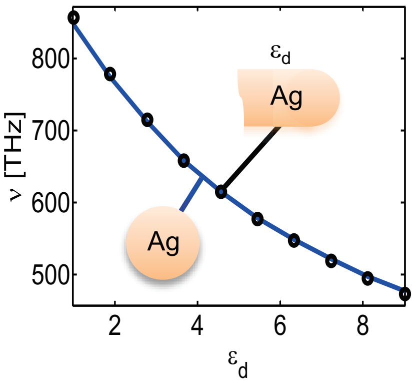

Figure 3.3.4: Comparison between the resonance frequencies predicted by QS theory and antenna models as a function of the permittivity ε_d of the surrounding medium. Solid line describes the QS resonances whereas the antenna resonance is indicated by circular marks.

modes beyond hemispherical cap (Fig. 3.3.2). We speculate it to be caused by the increased metallic damping which steadily increases as the plasma limit is approached.

In the following sections, we will perform the foregoing analysis for other geometries presented in Fig. 3.1.1. Since the methodology is exactly the same, we will keep the description terse and present results straightforwardly unless a peculiarity of the case under consideration calls for greater illustration.

3.4 Core-shell

Plasmonic core-shell particles are a straightforward extension of the spherical geometry in which the sphere made up of metal (dielectric) is coated over with a thin layer of dielectric (metal). It allows the thickness of the film to be used as a degree of freedom to tune the resonance of the particle over a wide spectral range [116] which in the simple case of a sphere is dependent only upon the physical parameters of the metal and surrounding medium. In the QS limit, this behavior is well-understood in terms of the hybridization theory which describes the splitting of resonances of the isolated core and shell spherical particles into bonding and anti-bonding modes. The corresponding frequencies of the modes are given by [117]:

$$\nu_{l\pm} = \frac{\nu_\mathrm{p}^2}{2}\left[1 \pm \frac{1}{2l+1}\sqrt{1 + 4l\left(l+1\right)\left(\frac{a}{b}\right)^{2l+1}}\right], \tag{3.4.1}$$

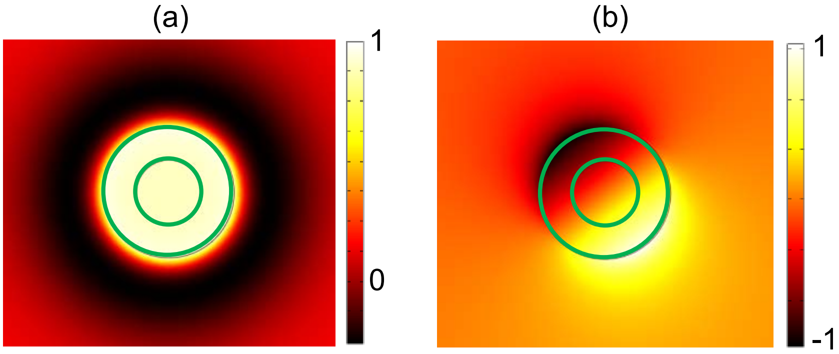

Figure 3.4.1: Electric field distribution of the longitudinal component of symmetric (a) and anti-symmetric (b) modes supported by the core-shell waveguide. Inner and outer radii are 10 nm and 20 nm respectively whereas the core and cladding are air and shell is assumed to be Ag at $\nu = 500\,\mathrm{THz}$.

where ν_p denotes the bulk plasma frequency of the electron gas, l stands for the order of spherical harmonic that is undergoing hybridization and the inner and outer radii of the core-shell particle are denoted by a and b respectively. Of the two hybridized modes, only the lower energy one brightly scatters the light. The higher energy mode has a dominantly quadrupolar character and thus does not interact strongly under normal circumstances with the plane wave excitation. Therefore, it is the bright lower energy mode that we shall be interested in the rest of this section.

From the antenna point of view, the whole problem once again has to be understood in terms of a core-shell waveguide with hemispherical core-shell termination likewise. As shown in Fig. 3.1.1(b), we consider a dielectric core of radius a cladded with Ag metallic film of thickness $b - a$. The waveguide is terminated similarly into a core-shell cap whose inner and outer radii are the same as those of the core. Similar to the behavior of localized resonances in core-shell particles, the modes related to each azimuthal order m splits into symmetric and anti-symmetric modes, each characterized with respect to the electric field component parallel to propagation direction. Dispersion of these modes is determined by a complicated transcendental equation obtained by applying Maxwell boundary conditions at the material interfaces [118]. Since we will be exclusively working with core and shell radii $\{a, b\} \ll \lambda$, modes characterized by azimuthal order $|m| \geq 1$ can be ignored which cut-off in this regime [118]. Furthermore, the anti-symmetric mode of azimuthal order $m = 0$ is cut-off except near the plasma frequency of metal and certain ratio of a/b [118]. This leaves us practically with a mono-mode system that sustains only the symmetric TM_0 mode. Figures 3.4.1(a) and (b) show the longitudinal electric

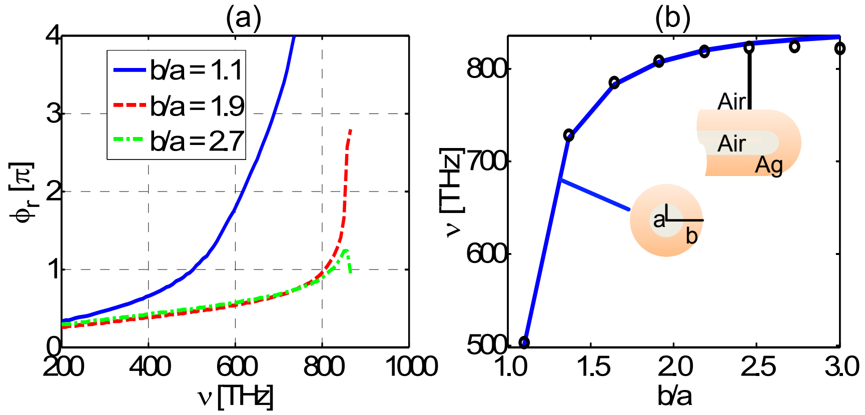

Figure 3.4.2: (a) Reflection phase jump of the symmetric TM_0 mode guided on the core-shell waveguide of inner radius $a = 10\,\mathrm{nm}$ and outer radius given by the b/a ratio. Shell is made up of Ag while the core and cladding are taken to be air. (b) Comparison between QS resonance denoted by the blue solid curve with antenna resonances represented by circular marks.

field distribution of symmetric and anti-symmetric modes for $m = 0$.

To compare the QS and antenna model, we consider a core-shell particle whose core of fixed radius $a = 10\,\mathrm{nm}$ and cladding are made up of air while the shell of radius b is made up of Ag. Figure 3.4.2(a) plots the reflection phase jump $\phi_{\mathrm{r}}(\nu)$ for various values of the outer and inner radii ratio b/a. The first order antenna resonance is compared with the QS resonance of the lower energy symmetric mode of Eq. (3.4.1) in Fig. 3.4.2(b) for a range of ratio b/a. As evident from Fig. 3.4.2(b), the resonance frequency asymptotes to a limiting value for larger values of b/a whereas for smaller ratios splitting of the resonance seems to be larger. This happens because the coupling between the modes of isolated metallic sphere and hole weakens due to decreasing field overlap of the modes when the shell thickness is increased. Quite remarkably, this feature appears to be perfectly captured by the reflection phase jump in Fig. 3.4.2(a). For smaller values of the ratio b/a, it accumulates faster to π causing the cavity resonance to coincide just around the same frequency as predicted by the QS model. As the value of b/a becomes larger, we find the reflected phase jump converges to a curve which becomes by and large independent of the defining b/a ratio.

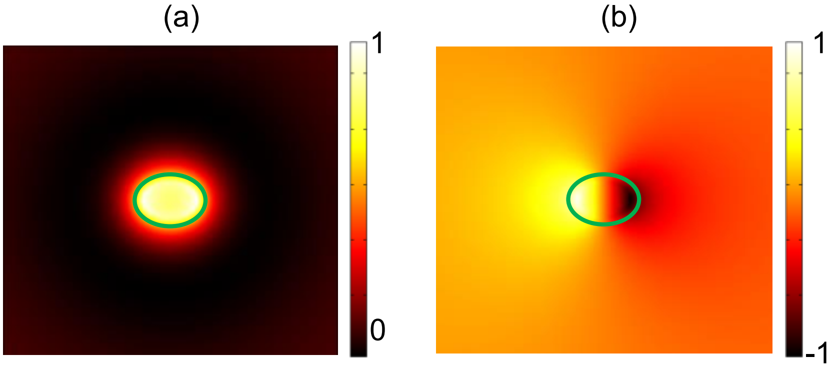

Figure 3.5.1: Electric field distribution of the longitudinal component of symmetric (a) and anti-symmetric (b) modes supported by a Ag elliptical core waveguide surrounded by air at $\nu = 400\,\mathrm{THz}$. Smaller and larger semi-axes are 15 nm and 20 nm respectively.

3.5 Ellipsoid

Ellipsoids are direct generalization of the spherical geometry in which all the semi-axes are identical. For theoretical evaluation, ellipsoids are generally characterized in terms of prolate and oblate spheroids which are formed by rotating an ellipse around its major and minor axes respectively. Thus the spheroids have two of the three semi-axes identical. From a physical point of view, spheroids (or ellipsoids) afford additional degree of freedom by allowing the possibility to tune their resonance through adjusting their defining axes [119]. In quasi-static limit, the dipole polarizability of the ellipsoid is defined as [8]

$$\alpha(\nu) = 4\pi abc \frac{\varepsilon_{\mathrm{d}}(\nu) - \varepsilon_{\mathrm{m}}(\nu)}{3\varepsilon_{\mathrm{m}}(\nu) + 3S\left[\varepsilon_{\mathrm{d}}(\nu) - \varepsilon_{\mathrm{m}}(\nu)\right]}, \tag{3.5.1}$$

where a, b and c are the three semi-axes and S is the geometrical shape-factor. While the exact expression of the shape factor can take a complicated form and vary according to the incident polarization from prolate to oblate spheroids [8], it geometrically remains a function only of the aspect ratio between the two non-identical axes of the spheroid. This allows the dipole resonance to be adjusted by tailoring the geometrical features of the particles in a simple yet flexible way.

The FP equivalent of a general ellipsoidal particle is illustrated in Fig. 3.1.1(c). We consider a nano-wire of elliptical cross-section which is terminated by a semi-ellipsoidal cap. The semi-axes of the cap on the plane of wire cross-section are identical to those of the wire whereas the semi-axis perpendicular to the plane of cross-section is allowed to be different. Without any loss of generality, the surrounding dielectric medium is assumed to be air. The spheroids considered are generated by revolving around the semi-axis a while the semi-axis c (and hence b of the generated spheroid) remain fixed at 20 nm. As to the modes guided on the nanowire, for the semi-axes ratio $c/a = 1$ we retrieve a circular cross-section which has already been discussed in Sec. 3.3. For all other values, the cross-section is elliptical in shape. Figures 3.5.1(a) and (b) show the distribution of electric field components parallel to the propagation direction of the two modes supported on a Ag nanowire surrounded by air. While the mode shown in Fig. 3.5.1(a) is localized strongly on the metal-air interface, the mode of Fig. 3.5.1(b) has quite a wide spatial expanse and unlike the former mode its effective mode index is less than air. Therefore, we conclude that the symmetric mode shown in Fig. 3.5.1(a) should account for the QS resonance of the spheroid. Figures 3.5.1(c) and (d) plot the reflection phase jump of the mode for selected values of the ratio c/a.

We can finally now compare the resonances predicted according to the antenna model from Figs. 3.5.2(a) and (b) and the QS description obtained from Eq. (3.5.1). Figure 3.5.2(c) plots the two resonances together. The quasi-static resonance is represented in Fig. 3.5.2 through solid blue curve which is the case when the illuminating radiation is polarized parallel to the a-axis (axis of revolution). For the case when the incident polarization is perpendicular to the a-axis, quasi-static resonance is plotted in dashed-red color. Comparison with the antenna resonance for the two cases is shown through circular and diamond marks respectively. While we observe some deviation between QS and cavity resonances, we attribute it to numerical noise which arises due to compromise between mesh resolution and computational cost incurred in running a rigorous 3D FEM simulation. But overall, we find good agreement between the resonance frequencies predicted by both approaches.

3.6 Cylinder

Having discussed 3D particles, we at last consider metallic cylinder which extends indefinitely along its cylindrical axis. As the geometry is invariant along cylindrical axis, the whole problem can be reduced to a formulation on the 2D cross-sectional plane. The resonance sustained by such a metallic cylinder of permittivity $\varepsilon_{\mathrm{m}}(\nu)$ when illuminated with light propagating in the cross-sectional plane and polarized perpendicular to the cylindrical axis (i.e. polarized in the plane of propagation) is defined as [8]

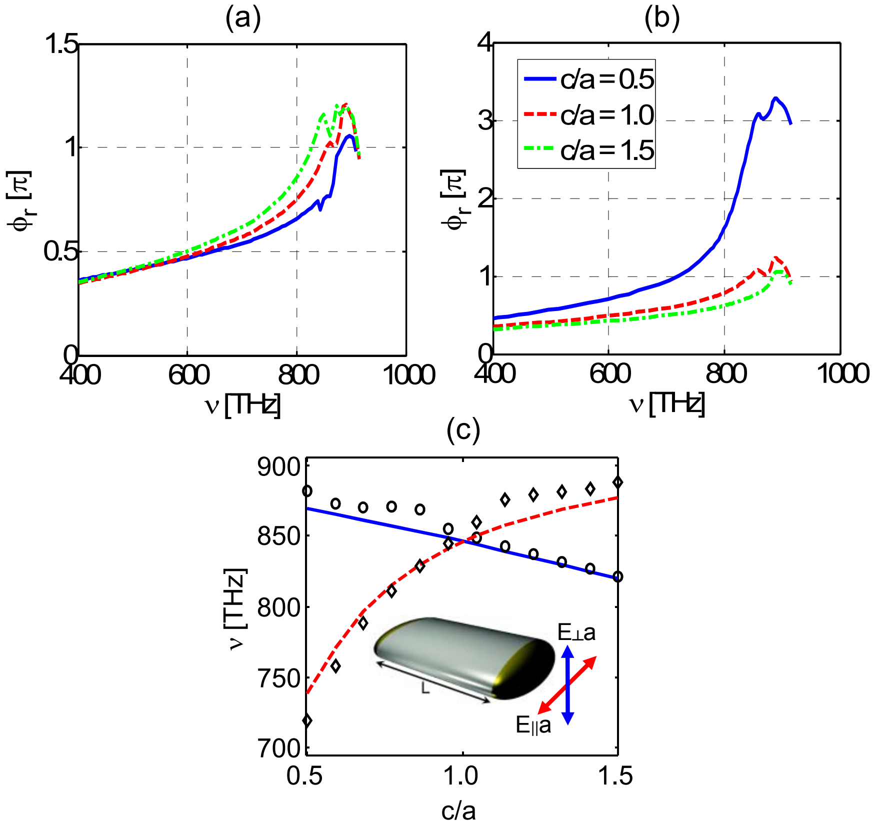

Figure 3.5.2: Reflection phase jump of the symmetric mode [Fig. 3.5.1(a)] when the incident polarization is parallel (a) and perpendicular (b) to the axis of rotation a [inset of (c)]. Comparison between QS and antenna resonance of spheroids in (c) as the ratio between semi-axes c/a. Blue solid line represents QS resonance when the incident polarization is parallel to a-axis (inset) while the dashed red line represents the case when it is perpendicular. The corresponding cavity resonances are denoted by circular and diamond marks for the two respective cases.

$$\Re\left\{\varepsilon_{\mathrm{m}}(\nu)\right\} = -\varepsilon_{\mathrm{d}}(\nu), \tag{3.6.1}$$

where $\varepsilon_{\mathrm{d}}(\nu)$ is the permittivity of the surrounding medium. In terms of a Fabry-Perot cavity, the geometry of a cylinder can be mimicked by an insulator-metal-insulator (IMI) strip having semi-circular terminations [Fig. 3.1.1(d)]. The IMI waveguide of thickness a exhibits hybridized symmetric and anti-symmetric SPP modes whose dispersion is defined as [2]

$$\tanh\left[\frac{k_{\mathrm{m}}(\nu)\,a}{2}\right] = -\frac{k_{\mathrm{d}}(\nu)\,\varepsilon_{\mathrm{m}}(\nu)}{k_{\mathrm{m}}(\nu)\,\varepsilon_{\mathrm{d}}(\nu)} \tag{3.6.2}$$

for odd symmetry and

$$\tanh\left[\frac{k_{\mathrm{m}}(\nu)\,a}{2}\right] = -\frac{k_{\mathrm{m}}(\nu)\,\varepsilon_{\mathrm{d}}(\nu)}{k_{\mathrm{d}}(\nu)\,\varepsilon_{\mathrm{m}}(\nu)} \tag{3.6.3}$$

for even parity. Symmetry of the modes is considered with respect to the component of electric field parallel to propagation direction. Mode propagation wave number $\beta(\nu)$ is defined in Eq. (3.6.2,3.6.3) through the transverse wave number $k_{\{\mathrm{m,d}\}}(\nu)$ as

$$k_{\{\mathrm{m,d}\}}(\nu) = \sqrt{\beta^2(\nu) - k_0^2(\nu)\,\varepsilon_{\{\mathrm{m,d}\}}(\nu)}. \tag{3.6.4}$$

While writing Eqs. (3.6.2) and (3.6.3), the geometry was assumed to be symmetric such that the dielectric permittivity of both substrate and cladding is $\varepsilon_{\mathrm{d}}(\nu)$. Figures 3.6.1(a) and (b) plot the cross-sectional distribution of the longitudinal component of the electric field (i.e. parallel to propagation direction) of the anti-symmetric and symmetric modes respectively.

In order to relate the modes guided on Ag film with the QS response of metallic cylinder, we note that only one of the two modes guided can be a possible candidate for producing cavity resonance in Fabry-Perot model. The symmetric mode of the IMI geometry has the characteristic that it localizes with reducing thickness whereas the anti-symmetric one delocalizes in the limit of vanishing thickness. As already discussed in the context of TM_1 mode sustained by metallic cylinder in Sec. 3.3, the anti-symmetric mode of IMI strip cannot be responsible for a localized resonance which is the hallmark of QS response. Therefore, we discern that the symmetric mode should be probed for comparison with scattering resonance of the cylinder in quasi-static regime.

We perform numerical computations on a Ag strip of thickness $a = 20\,\mathrm{nm}$ surrounded by a dielectric medium of constant permittivity ε_{d}. This corresponds to a cylinder

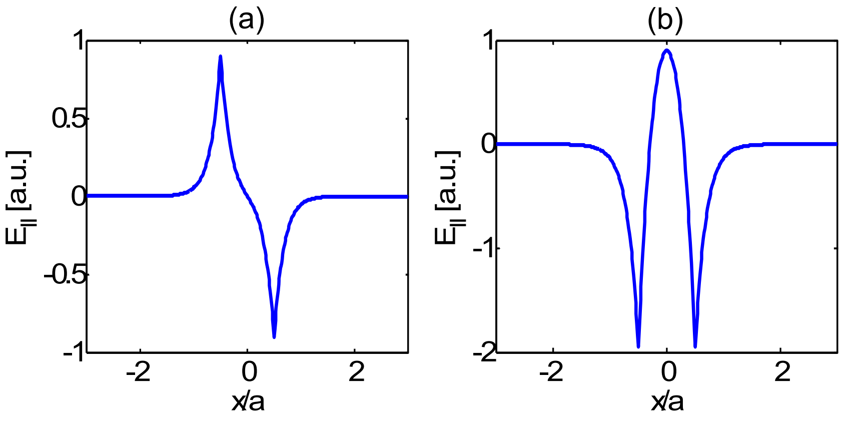

Figure 3.6.1: Electric field component parallel to propagation direction of (a) anti-symmetric and (b) symmetric modes. Modes have been computed for a Ag film of thickness $a = 20\,\mathrm{nm}$ at $\nu = 600\,\mathrm{THz}$ and surrounded by air.

whose radius is 10 nm. Simulation geometry remains essentially the same as shown in Fig. (3.3.2) with now a different interpretation of being on a 2D plane. Figure 3.6.2(a) plots the reflection phase jump of the symmetric mode from the semi-circular termination for a few select values of the permittivity of the surrounding medium. We note that for the case of air [solid blue curve in Fig. 3.6.2(a)], the maximum value of the phase $\phi_\mathrm{r}(\nu)$ of the mode is around 0.95π. However, we attribute this to a shift induced by numerical errors such as discretization, finite cross-section length and the influence of PML regions on the cross-sectional plane where the mode overlap is evaluated. Figure 3.6.2 shows the comparison between the antenna resonance of Fig. 3.1.1(d) when its length is reduced to zero and the localized resonances of the cylinder according to QS resonance [Eq. (3.6.1)]. Once again, we observe excellent correspondence between the two resonances substantiating the applicability of FP model for 2D cylinders.

3.7 Composite particle

After demonstrating the applicability of the FP model to localized resonances found in nano-particles we are now in a position to extend this proposition to a structure that are not amenable to analytical treatment. This would be potentially useful for tuning or determining resonances of particles whose shape does not conform to that of analytically studied geometries either due to fabrication errors or because fine tuning of their resonance properties is desired. As a specific case, we consider an egg shaped particle which is made up by conjoining a hemisphere with a semi-ellipsoid. The two

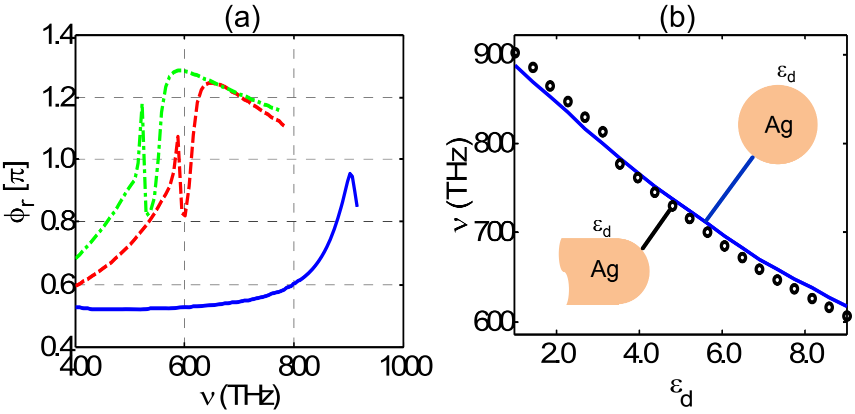

Figure 3.6.2: (a) Reflection phase jump of the symmetric IMI mode for $\varepsilon_{\mathrm{d}} = 1$ (solid blue), $\varepsilon_{\mathrm{d}} = 5$ (dashed red) and $\varepsilon_{\mathrm{d}} = 9$ (dotted-dash green) of the surrounding medium. Thickness of the Ag metallic film was taken to be 20nm. (b) Comparison between QS and antenna resonance of a 2D cylinder as a function of the permittivity ε_{d} of the surrounding medium. The solid line denotes quasi-static resonance whereas cavity resonances are marked with circles.

semi-axes of the semi-ellipsoid are equal to radius of the hemisphere while the third axis is different so as to produce the egg shape of the composite particle (inset of Fig. 3.7.1).

Such a geometry cannot be analytically treated at least through any of the known, established methods. The semi-analytical model, nevertheless, of waveguide resonances in a FP cavity presented and demonstrated in the foregoing sections makes it possible to predict and tune the resonance of such particles. In terms of Fig. 3.1.1(a), the asymmetric cavity is formed by having a hemispherical on one end while a semi-ellipsoidal cap on the other. Half of the reflection phase-jump of the guided TM_0 mode on the cylinder is contributed by the hemispherical cap $[\phi_{\mathrm{s}}(\nu)]$ while the rest comes from the semi-ellipsoid $[\phi_{\mathrm{e}}(\nu)]$. The structure resonates when the total round trip phase $\phi(\nu) = \phi_{\mathrm{s}}(\nu) + \phi_{\mathrm{e}}(\nu)$ is equal to an integer multiple of 2π (Fig. 3.7.1).

In order to compare the prediction of our semi-analytical model, we numerically compute the scattering spectra of our composite particle shown in the upper part of Fig. 3.7.1. For reference, we also include the spectra of a perfect sphere (radius 15 nm) and spheroid ($a = b = 15\,\mathrm{nm}$ and $c = 20\,\mathrm{nm}$). The lower part of Fig. 3.7.1 shows the total round-trip phase whose intersection with the 2π line indicates cavity resonance. Comparing the lower and upper parts, it is evident that the resonances predicted by FP model and rigorous scattering computations are in excellent agreement.

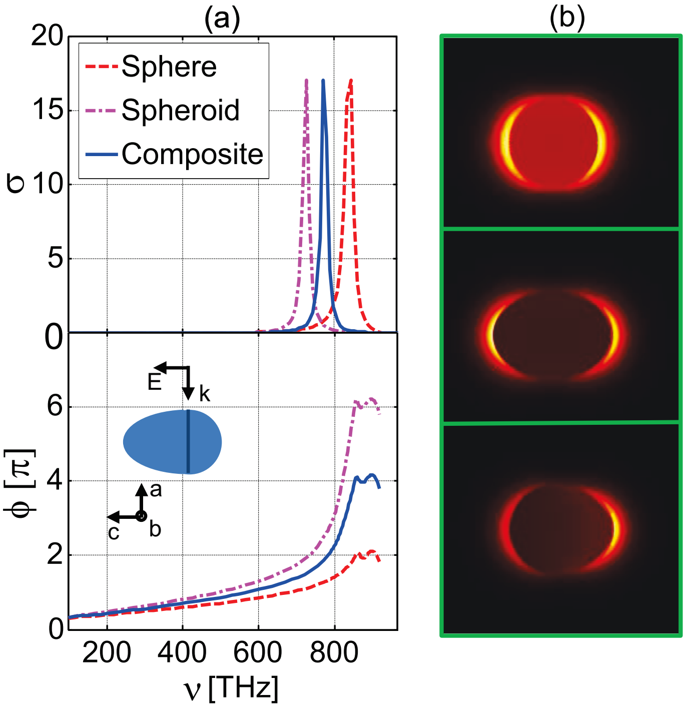

Figure 3.7.1: (a) Normalized scattering spectra (top) and round-trip phase (bottom) of a sphere, spheroid and composite particle made up by conjoining a semi-ellipsoid with a hemisphere (inset of the figure at bottom). Radius of the sphere is 15nm, spheroids semi-axes $a = b = 15\,\mathrm{nm}$ and $c = 20\,\mathrm{nm}$, while the composite particle is made up of hemisphere and semi-ellipsoids just described. (b) Scattered electric field norm at resonance of the corresponding sphere, spheroid and composite particles in order from top to bottom.

3.8 Concluding remarks

To sum up the results of our foregoing discussion, we demonstrated the equivalence between the localized resonances exhibited by plasmonic nano-particles in QS regime with the resonances exhibited by a FP antenna of negligible length but with suitable terminations such that the round-trip phase accumulates only upon reflection from the mirrors. Much sophisticated structures were also possible however we sufficed to discuss only those geometries whose physics is understood on analytical grounds to permit comparison between exact results and semi-analytical model. Therefore, we treated a core-shell particle, spheroids and infinitely extending cylinders. All of the cases turned out to be well predictable by our approach within the limits of numerical accuracy. At the very end, we tested the FP approach to predict the resonance of a composite particle which was formed by putting together a semi-spheroid and a hemisphere. By means of rigorous scattering simulations, we were able to validate the prediction of our approach. This suggests a new way to tailor the resonance of those particles which are otherwise inaccessible to theoretical methods.

After publication of the results presented in the foregoing [120], the equivalence between QS and antenna model was further investigated by analyzing the Q-factor of a sub-wavelength FP cavity [121]. As it turned out, the Q-factor was shown to be equal to that of a particle in QS limit [Eq. (3.1.1)] which is the same for all particles irrespective of geometrical shape. This served as yet another proof of the equivalence between the two perspectives.

Nevertheless, we would like to honestly point out the missing links in our picture which should be found for the completion of our model. In discussing the antenna resonances of particles, we always considered the first π-crossing of reflection phase jump $\phi_{\mathrm{r}}(\nu)$ for comparison with QS limit. However, at times we found there to be multiple crossings of π as well as its higher order integer multiples [see Fig.3.3.4 (a), Fig. 3.4.2(a), Figs. 3.5.2(a) and (b), Fig. 3.6.2(a), Fig. 3.7.1(b)]. In principle, all the odd integer multiple values of π should cause FP resonances in symmetric structures. However, except for the core-shell geometry which exhibits two hybridized resonances, this contradicts the QS description of the particles considered in this chapter which are known to support only one scattering resonance. Even for core-shell particles, the higher energy resonance is dark whereas we find $\phi_{\mathrm{r}}(\nu)$ of PSPP mode supported by core-shell waveguide to be achieving 3π value [Fig. 3.4.2(a)] which should be able to induce a bright resonance. As a possible way to address this discrepancy, we speculate that a complete treatment of the FP cavity is required that takes into account absorption at the mirrors, coupling efficiency of the incoming radiation to the guided PSPP mode and out-coupling to plane waves in the free-space at terminations. If there is indeed full correspondence between QS and FP models, it should be able to explain why higher order modes are not found in the scattering response.

4 Nonlinear response of cylindrical antennas

4.1 Introduction

It was established in the previous chapter how the localized resonances sustained by plasmonic nano-structures in the QS limit can be seen as an epiphenomenon of the cavity dynamics induced by the excitation of PSPP modes at the terminal edges. In the present chapter, we will be considering plasmonic cavities with similar terminal caps from another viewpoint. We wish to investigate the potential of such systems in enhancing the strength of nonlinear response of the system. The objective of the previous chapter necessitated us to consider that have a vanishing length such that the entire phase-accumulation takes place only at the terminal caps. However, now we will allow ourselves a greater degree of design freedom by considering similar cavities but with non-vanishing length such that the phase-accumulation incurred during the propagation of SPP mode also contributes to determining the resonance of antennas. It is to naturally take advantage of the highly dispersive behavior of the modal reflection coefficient of the PSPP mode both to physical and geometrical parameters of the system.

Thanks to the sub-wavelength focusing of light by plasmonic antennas, there is an ever increasing interest in exploring both novel and known design schemes but at the sub-wavelength scale. Some famous examples include directional control of light by a nano-optical Yagi-Uda scheme [122], detecting the presence of Hydrogen gas at single particle level [123], controlling single molecule emission [124], etc. At the same time, however, the high near field intensities found at the metal-dielectric interface naturally give rise to the question as to the potential of this phenomenon in enhancing the nonlinear response of the antenna [11]. Unlike the linear response of the system, the nature and strength of nonlinear interaction depends critically upon the intensity of the electromagnetic field involved. Therefore, any optical system or illuminating scheme that provides higher electromagnetic field intensities would naturally be more favorable for observing nonlinear electromagnetic phenomena at nanoscale.

Consequently, the high field confinement in plasmonic systems raises the bar for familiar phenomena such as frequency mixing and nonlinear modulation of material index. At the same time, high near fields also trigger to prominent levels those nonlinear processes which are at times too weak to be of any practical interest. Some conspicuous examples of such cases include the generation of third harmonic (TH) due to the nonlinear polarization induced inside metals or even the observation of second harmonic (SH) generation due to symmetry breaking at metallic surfaces [111,125–128] or even bulk SH generation from non-centrosymmetric plasmonic structures [129–133]. Therefore, it is possible to observe significant frequency conversion from plasmonic systems even if they are placed in vacuum or surrounded by media having vanishingly small nonlinear response. This naturally caused a great deal of research to separate the contribution originating from the nonlinear polarization induced inside the dielectric and metallic regions. The former is referred to as extrinsic [134] whereas the latter is usually understood as the intrinsic nonlinear response of the nano-optical systems [135–138].

On a theoretical level, another recent approach for treating the intrinsic nonlinear response has been to consider the material dispersion of metals beyond the Drude formalism by means of semi-classical hydrodynamic models [94,139,140]. In the same vein, much work has also been done to study plasmonic systems containing dielectric materials which act as a much stronger source of nonlinear activity [141,142]. The metallic components are designed such as to focus large amount of incident power to dielectric regions which results in huge enhancement of nonlinear response compared to an all-dielectric setup.

As a general rule, the nonlinear processes involve the interaction of light oscillating at multiple frequencies depending on the order of nonlinearity and the specific nature of interaction under consideration. This makes it ideal, if not necessary, to have plasmonic elements that are resonant to all the frequencies involved. Recent studies attempted to perceive such nanostructures by employing innovative antenna designs with tunability at multiple frequencies [83–86]. However, most of these approaches usually choose a path where a few individual antennas that sustain resonances at selected frequencies are fused into a single optical antenna. This assures the requirement of having a antenna that sustains resonances at all frequencies of interest [83, 85]. But it is challenging to achieve a good spatial overlap - necessary for strong nonlinear response - among the modes at different frequencies which might localize in different spatial domains of the composite antenna geometry. Moreover, it is easy to realize that the fabrication of such structures that consist of multiple elements remains a challenge for current nanofabrication. Even though many top-down as well as bottom-up approaches for nanofabrication are developed, the precise alignment of the individual elements to form the actual antenna constitutes an unnecessary complication. Therefore, it is desirable to have available compact and isolated antennas that can sustain resonances at frequencies on demand.

In the present chapter, we aim to explore the potential of cylindrical nanowires as an ideal platform to tailor the nonlinear interaction of light with matter and which meets both aforementioned requirements. These optical nanowire antennas are superior for various reasons when compared to many other antennas. First, their basic functionality is well understood by now in terms of semi-analytical models [59, 115]. Second, various fabrication methods have been proven to be applicable to realize these antennas with high precision in experimental studies (see for instance Refs. [60, 143]).

In the following sections, we will show that by engineering the termination of a cylindrical antenna, we can devise configurations that sustain resonances at multiple frequencies which are involved in the nonlinear process. This will be followed by numerical estimation of the nonlinear response of these antennas to demonstrate their superiority over singly-resonant schemes. To this end, we will combine a mix of theoretical and numerical means to explore the opportunities available to tailor the second-order nonlinear response of nanowire antennas embedded in Lithium Niobate ($\mathrm{LiNbO_3}$). Specifically, we utilize an analytical model that can precisely predict the resonances, use a coupled-field theory approach to calculate the strength of the nonlinear response, and verify all our predictions using full-wave simulations that take into account the nonlinear process correctly.

4.2 Antenna design consideration

As mentioned in the introduction, we will exploit the length of the antenna as an important degree of freedom along with terminal caps to tune the resonance frequencies of our antennas. Therefore, the resonance is determined by identifying the geometrical configurations in which the back and forth propagating guided PSPP mode accumulates a round-trip phase which is an integral multiple of 2π at resonance frequency. Contributions to this phase accumulation are due to propagation along the nanowire, i.e., determined by the dispersion relation, but also by the phase of the complex reflection coefficient at the termination. While the phase accumulation due to propagation is independent of the cap, the reflection phase jump depends in a complex way on both geometry of the cap as well as the dispersion of PSPP mode. Similarly, while it has been possible in some special yet practically important cases to analytically calculate the dispersion of PSPP mode, the same does not hold true for the modal reflection coefficient except for the simplest case of flat wire termination [115]. Perhaps for these reasons, the design and engineering of the antenna terminations with a view to tailor the antenna resonances has thus far remained an underestimated factor. Therefore, it is only natural to fill in this gap by taking into account the phase of modal reflection coefficient from antenna terminations and apply it towards an enhancement of multi-frequency nonlinear processes as discussed before.

4.3 Linear response

The nonlinear response of the system in case of a non-resonant interaction of light with matter can be well described within the formalism of perturbative nonlinear optics [87]. Therefore, tuning the linear response of the system is the first step towards predicting the nonlinear output. A strong linear light matter interaction will also result in strong nonlinear interaction.

Figure 4.3.1(a) sketches the antenna geometry under consideration. It consists of a cylindrical nanowire of length L that has a semi-ellipsoidal cap as termination. Two of the three semi-axes of the cap are identical to the radius of the nanowire whereas the third semi-axis a [Fig. 4.3.1(a)] is allowed to be different. This serves as an additional degree of freedom to tailor the response of the antenna. The limiting case of $a = 0$ would make it an abrupt termination whereas the other limiting scenario of $L = 0$ would cause the antenna to collapse towards an ellipsoidal nano-particle [120]. When illuminated with a plane wave whose electric field is polarized along the cylinder's axis [x-axis in Fig. 4.3.1(a)] and propagating along the z-axis [Fig. 4.3.1(a)], a PSPP is excited on the nanowire. It bounces back and forth between the semi-ellipsoidal terminations where it causes the antenna to sustain eventually Fabry-Perot (FP) resonances at specific frequencies for a fixed geometry. The requirement to observe antenna resonance at a frequency ν is expressed as [59, 109, 120]

$$\beta^{'}(\nu)L + \phi_{\mathrm{r}}(a,\nu) = m\pi, \tag{4.3.1}$$

where $\beta^{'}(\nu) = \Re\{\beta(\nu)\}$ is the real part of the propagation constant, $\phi_{\mathrm{r}}(a,\nu)$ the phase of the modal reflection coefficient $r(\nu)$, L the length of the cavity, and m an integer denoting

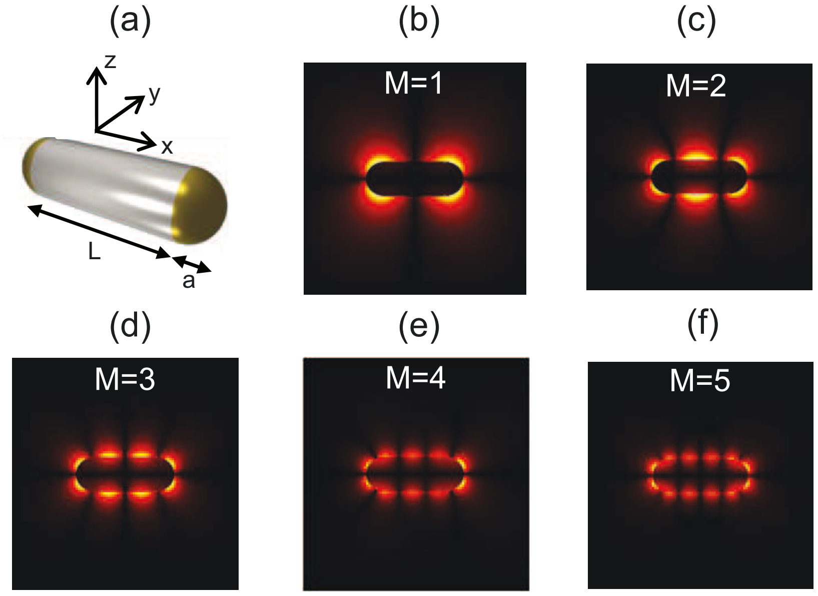

Figure 4.3.1: (a) Cylindrical nanowire of length L terminated by semi-ellipsoidal caps on both sides. Two semi-axes of these caps are shared with the radius of the nanowire whereas the third axis is a free parameter, labeled as a. (b-f) $|E_\mathrm{y}|$ distribution on xy-plane of FP modes of order M when the antenna is illuminated by an x-polarized plane wave propagating along z-axis. For exciting modes with even integer M, the exciting wave was inclined with respect to the z-axis on the xz-plane in order to break the symmetry. Length of the antenna is 50nm while the cap semi-axis $a = 17\,\mathrm{nm}$.

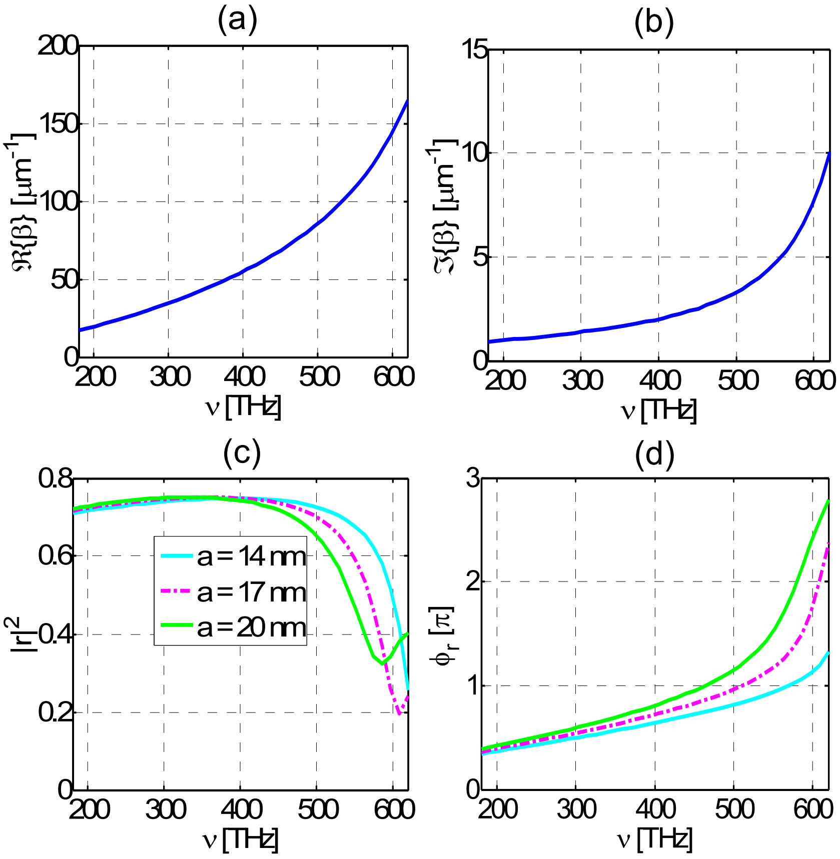

Figure 4.3.2: Dispersion of the real (a) and imaginary (b) parts of fundamental TM_0 mode computed for a cylindrical wire of radius 15 nm embedded in $\mathrm{LiNb}O_3$. (c) Amplitude $|r|^2$ and (d) phase $\phi_\mathrm{r}(\nu) = \arg\left[r(\nu)\right]$ of the reflection coefficient for three different spheroids as the termination.

the order of FP resonance. It should be pointed out that only symmetric antennas are considered here, i.e., those where the antenna cap is identical for both terminations. This means that for normal incidence with respect to z-axis, only resonances associated with odd integer values of m would be visible. Even integer order resonances would remain forbidden in this scheme until the illuminating field is inclined to the z-axis on xz-plane [Fig. 4.3.1(a)] to break the illumination symmetry. Figures 4.3.1(b-f) plot the $|E_\mathrm{y}|$ field distribution of FP resonances of various order m in the xz cross-section plane of the antenna.

To be able to easily model the system in finite difference time domain (FDTD) simulations later, we numerically model the system by describing the cylindrical metallic antenna using a Drude fit of Ag [105] which is defined by the plasma frequency $\nu_\mathrm{p} = 1.88 \times 10^3$ THz and damping $\nu_\gamma = 19.3$ THz. Radius of the cylinder is chosen to be

15 nm such that the cross-section remains much smaller than the illuminating wavelength obviating any need to consider guided modes other than the fundamental TM_0 [59,120]. The surrounding dielectric medium is assumed to be LiNbO_3 whose dispersion is isotropically defined, for the sake of computational simplicity, through the extraordinary axis by means of a Sellmeir fit [144]. The anisotropy of the nonlinear $\chi^{(2)}$ tensor, however, is fully considered and its c-axis is aligned to the x-axis [Fig. 4.3.1(a)] to make the most out of the strongest d_{33} coefficient. Considering the fact that numerical techniques based on FEM are more suitable to capture geometrical curvature [145], we persist with our choice of commercially available FEM based electromagnetic solver COMSOL MULTIPHYSICS to compute all the physical quantities of interest in linear analysis.

Given the strong dispersion of $\beta(\nu)$ and $r(a,\nu)$ [Figs. 4.3.2(a-d)] upon both frequency and, in the case of latter, cap geometry, we attempt to explore the possibility to align FP resonances of different orders with the frequencies taking part in the nonlinear process. To this end, we propose to exploit the semi-axis a of the cap as a degree of freedom in design parameters while keeping the radius of the nanowire constant. This can be desirable in circumstances where strong field localization is required since the fundamental TM_0 mode shows increasing localization with decreasing wire radius (see the discussion in Sec. 3.3). As for the specific nonlinear interaction considered, we choose to work with nonlinear process of degenerate SH generation when the metallic cylinder is embedded in a dielectric medium possessing $\chi^{(2)}$ response. More complex scenarios involving three- or four-wave mixing (cubic media) can be explored along the same lines.

4.4 Tuning the resonances

Having obtained the modal dispersion and reflection phase jump of the TM_0 mode propagating on the wire, we are now in a position to predict the spectral position of various FP resonances that are supported by the antenna. In terms of the antenna length L, the resonance condition of Eq. (4.3.1) can be expressed for FH and SH frequencies as

$$\begin{aligned} L_m &= \frac{m\pi - \phi_\mathrm{r}(a,\nu^\mathrm{F})}{\beta'(\nu^\mathrm{F})}, \\ L_n &= \frac{n\pi - \phi_\mathrm{r}(a,\nu^\mathrm{S})}{\beta'(\nu^\mathrm{S})}, \end{aligned} \tag{4.4.1}$$

where $\beta'\left(\nu^{\{\mathrm{F,S}\}}\right) = \Re\left\{\beta\left(\nu^{\{\mathrm{F,S}\}}\right)\right\}$, m and n are integers denoting the order of the

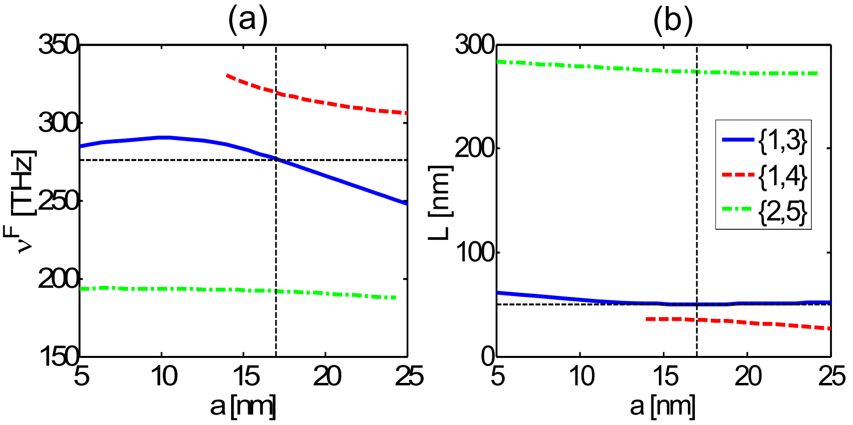

Figure 4.4.1: (a) Pump frequency ν^{F} at FH and (b) length L for the given cap radius a where the structure resonates at both FH and SH for FP orders m, n. Intersection of dashed-black lines indicates the doubly-resonant configuration chosen for further computations.

FP resonances at FH $\left(\nu^{\mathrm{F}}\right)$ and SH $\left(\nu^{\mathrm{S}}\right)$ frequencies respectively. For an antenna to be resonant at both FH and SH, we have the condition that $L_m = L_n$ for certain combinations of FP resonance orders m and n.

Figure 4.4.1 displays the result when the semi-axis a is varied from 5 nm to 25 nm and the FH frequency from 180 THz to 320 THz. The horizontal scale displays the cap radius a whereas the vertical scale in Fig. 4.4.1(a) denotes the frequency of illumination at FH. Figure 4.4.1(b) plots the required antenna length for the structure to be resonant at that illuminating frequency. Different graph colors identify the combination of FP resonance orders $\{m, n\}$ such that a working configuration is obtained by reading the configuration of the same order in both graphs.

Allowing for different FP orders at FH and SH, we found doubly-resonant configurations for the combination of 1st order at FH with 3rd and 4th order at SH, and the combination of 2nd order at FH with 5th order at SH, as indicated in the legend of Fig. 4.4.1(b). It is apparent that a suitable design that spans the entire frequency spectrum is not found for the present geometry. Nevertheless, this is something that will vary from structure to structure depending upon the exact geometrical configuration and physical properties of the media surrounding it.

We demonstrate the precise tuning of our multi-resonant structures by means of power transmission simulation through an array of such antennas. We choose a working configuration of FP mode orders {1,3} for the cap radius $a = 17\,\mathrm{nm}$. This is done so as to be able to work with bright resonances at both harmonic, i.e. excitable resonances, under

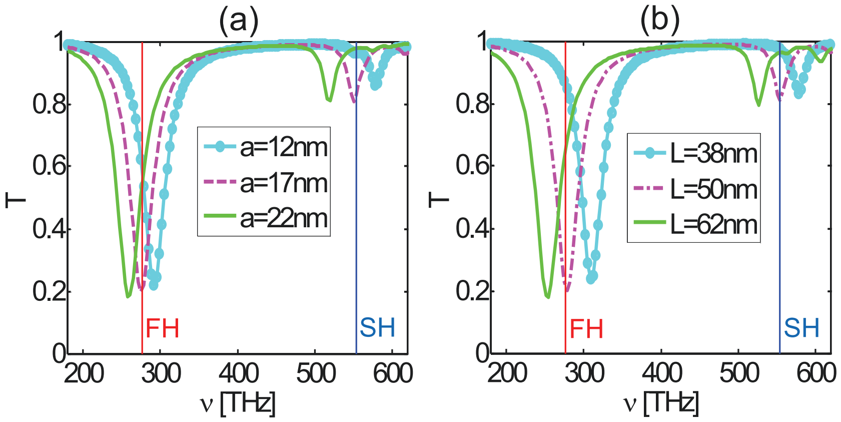

Figure 4.4.2: Linear transmission through the period array of antennas for (a) cap detuning and (b) length detuning.

normal illumination (parallel to the z-axis [Fig. 4.3.1(a)]). However, it is by no means a general restriction because other combinations could have been explored as well. This corresponds to illuminating frequency $\nu^{\mathrm{F}} = 277\,\mathrm{THz}$ and an antenna length $L = 50\,\mathrm{nm}$ according to the solid blue curve in Figs. 4.4.1 (a) and (b). Dimension of the periodic cell is taken to be 200 nm x 200 nm which is large enough to make the coupling between nearest neighbors negligible. The periodic array is then excited with x-polarized light according to Fig. 4.3.1(a) to compute the linear response of the system. Figures 4.4.2(a) and (b) plot the simulation results for cap and length detuning respectively. Evidently, the structures exhibit $1^{\mathrm{st}}$and 3^{rd} order resonances at $\nu = 277\,\mathrm{THz}$ and its corresponding SH when the geometrical configuration is precisely tuned to the required cap radius and antenna length. Therefore, we can safely conclude that the resonances predicted with the analytical model are indeed supported by the structure at the correct frequencies.

4.5 Nonlinear response

Having found structures that are capable of exhibiting resonances at both the illuminating FH and its corresponding SH frequencies, we will now attempt to estimate the benefit of employing such schemes for nonlinear interaction through a semi-analytic formulation. Therefore, an attempt will not be made to define a rigorous analytical approach to the problem of nonlinear interaction between normal modes, as we did in Sec. 2.5 for waveguides. Instead, we adopt a rather simplified and non-exact approach that gives us an estimate of the nonlinear interaction strength but not the quantified output.

According to the coupled mode theory employed in resonators that sustain weakly radiating modes, the nonlinear mode coupling coefficient is expressed as [146]

$$\gamma = \pi\nu_{\mathrm{S}} \frac{\iiint d\mathbf{r}\varepsilon_{\mathrm{r}}\left(\mathbf{r},\nu^{\mathrm{S}}\right)\chi^{(2)}\left(\mathbf{r},-2\nu^{\mathrm{F}};\nu^{\mathrm{F}},\nu^{\mathrm{F}}\right).\left[\mathbf{e}_0\left(\mathbf{r},\nu^{\mathrm{S}}\right)\right]^{\star}}{\iiint d\mathbf{r}\varepsilon_{\mathrm{r}}\left(\mathbf{r},\nu^{\mathrm{F}}\right)\left|\mathbf{e}_0\left(\mathbf{r},\nu^{\mathrm{F}}\right)\right|^2\left(\iiint d\mathbf{r}\varepsilon_{\mathrm{r}}\left(\mathbf{r},\nu^{\mathrm{S}}\right)\left|\mathbf{e}_0\left(\mathbf{r},\nu^{\mathrm{S}}\right)\right|^2\right)^{\frac{1}{2}}}, \tag{4.5.1}$$

where $\mathbf{e}_0\left(\mathbf{r},\nu^{\{\mathrm{F,S}\}}\right)$ is the linear eigen mode of resonator and $\varepsilon_{\mathrm{r}}\left(\mathbf{r},\nu^{\{\mathrm{F,S}\}}\right)$ is the permittivity of the medium at frequency $\nu^{\{\mathrm{F,S}\}}$. The corresponding coupled mode equations describing the evolution of mode envelopes $\tilde{a}^{\{\mathrm{F,S}\}}(t)$ are written as [146]

$$\begin{aligned}
\frac{d\tilde{a}^{\mathrm{F}}(t)}{dt} &= \left(\iota 2\pi\nu^{\mathrm{F}} - \frac{1}{\tau_{\mathrm{FH}}}\right)\tilde{a}^{\mathrm{F}}(t) - \iota\gamma\left\{\tilde{a}^{\mathrm{F}}(t)\right\}^{\star}\tilde{a}^{\mathrm{S}}(t) + \sqrt{\frac{2}{\tau_{\mathrm{s}}^{\mathrm{F}}}}s_{+}(t), \\
\frac{d\tilde{a}^{\mathrm{S}}(t)}{dt} &= \left(\iota 2\pi\nu^{\mathrm{S}} - \frac{1}{\tau^{\mathrm{S}}}\right)\tilde{a}^{\mathrm{S}}(t) - \iota\gamma\left\{\tilde{a}^{\mathrm{F}}(t)\right\}^{2} + \sqrt{\frac{2}{\tau_{\mathrm{s}}^{\mathrm{S}}}}s_{+}(t),
\end{aligned} \tag{4.5.2}$$

where $\tau^{\{\mathrm{F,S}\}}$ is the total cavity life time, $\tau_{\mathrm{s}}^{\{\mathrm{F,S}\}}$ the decay time to outgoing wave and $s_{+}(t)$ the amplitude of the incoming pump wave. Superscript $\{\mathrm{F,S}\}$ describes the harmonic of operation like before.

We take cue from the semi-analytical formalism presented above but modify it to suit our specific scenario. Computing linear modes of the antennas under consideration at both FH and SH for a wide range of geometrical parameters is prohibitively expensive in terms of computational cost. Instead, we consider the total electric field when the antennas are illuminated with incoming plane wave at FH. Taking total field at SH into account would actually correspond to parametric interaction in which both harmonics are pumped. Therefore, we consider the scattered field at SH which is easily obtained by removing the contribution of incoming plane wave from the total field. At resonance, the total and scattered fields around the antenna would be nevertheless dominated by the resonant mode. Otherwise, it would be just a superposition of linear modes as expected in any realistic illumination scheme. We thus define a nonlinear *field* coupling or overlap coefficient as

$$\gamma = \varepsilon_0\nu^{\mathrm{S}}\iiint d\mathbf{r}\chi^{(2)}\left(\mathbf{r},-2\nu^{\mathrm{F}};\nu^{\mathrm{F}},\nu^{\mathrm{F}}\right).\left[\mathbf{e}_{\mathrm{sc}}\left(\mathbf{r},\nu^{\mathrm{S}}\right)\right]^{\star}. \tag{4.5.3}$$

The field overlap coefficient γ defined in Eq. (4.5.3) above has a unit of Watts. Assuming Kleinman's symmetry [87] and exploiting the fact that d_{33} component of the nonlinear susceptibility tensor of $\mathrm{LiNbO_3}$ happens to be the strongest [87], we align the

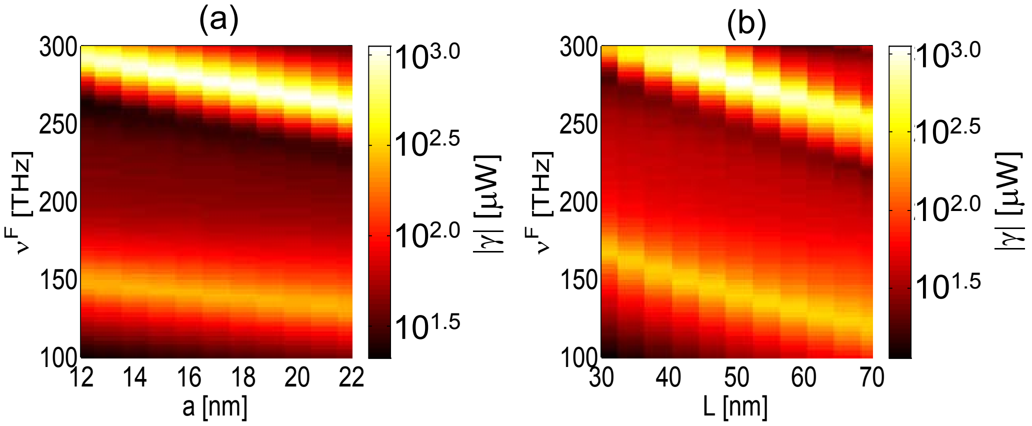

Figure 4.5.1: The nonlinear mode overlap over a range of frequencies when cap radius (a) and length of the antenna (b) are varied. Periodic cell is illuminated with a pump of power 1 W per unit cell at both FH and SH frequencies. Please note that $|\gamma|$ is mapped on a logarithmic scale.

optical axis of the nonlinear crystal with the incident polarization [x-axis in Fig. 4.3.1(a)]. This allows us to simplify Eq. (4.5.3) into an approximate form:

$$\gamma \approx \varepsilon_0 \nu^{\mathrm{S}} \iiint d\mathbf{r} d_{33}(\mathbf{r}) E_x^2(\mathbf{r}, \nu^{\mathrm{F}}) E_{x,\mathrm{sc}}^{\star}(\mathbf{r}, \nu^{\mathrm{S}}) \tag{4.5.4}$$

Equation (4.5.4) helps in qualitatively understanding the outcome of Eq. (4.5.3). In numerical simulations, however, the full anisotropic $\chi^{(2)}$ tensor is taken into account. It can be seen from Eq. (4.5.4) that for there to be strong nonlinear coupling, the $E_{x,\mathrm{sc}}\left(\mathbf{r}, \nu^{\mathrm{S}}\right)$ component of scattered electric field (and of resonant mode) at SH needs to have symmetric distribution. Anti-symmetric field distribution at SH will prevent any enhancement of nonlinear response even with a resonance at FH.

By illuminating the periodic array with a plane wave of power 1 W per unit cell at each harmonic, we scanned for the variation of $|\gamma|$ in case of cap and length detuning as before. The results are shown in Fig. 4.5.1. We find approximately twice the order of magnitude enhancement in $|\gamma|$ when $\nu^{\mathrm{F}} = 277\,\mathrm{THz}$ and the cap axis $a = 17\,\mathrm{nm}$ [Fig. 4.5.1(a)] or length $L = 50\,\mathrm{nm}$ [Fig. 4.5.1(b)]. Another bright trace is visible when the incident pump frequency is $\nu^{\mathrm{F}} \approx 139\,\mathrm{THz}$. This happens because the corresponding SH frequency coincides with the first order FP resonance of the antenna causing a comparatively weak enhancement in the strength of nonlinear interaction.

As described before, the nonlinear coupling coefficient γ is only to estimate the nonlinear coupling strength in the light of a semi-analytical coupled mode theory. To confirm its prediction, we resort to an in-house code based on rigorous finite-difference time-domain (FDTD) method [147] to substantiate its predictions. The cartesian grid size was chosen to be 1 nm whereas the metallic and dielectric dispersions were directly incorporated through the Drude and Sellmeir models described earlier. The instantaneous nonlinear polarization of the dielectric medium was embedded in the code in the following form:

$$\tilde{\mathbf{P}}^{(2)}(\mathbf{r},t) = 2\varepsilon_0 \begin{pmatrix} d_{33}(\mathbf{r})\tilde{E}_x^2(\mathbf{r},t) + d_{31}(\mathbf{r})\tilde{E}_y^2(\mathbf{r},t) \\ 2d_{31}(\mathbf{r})\tilde{E}_x(\mathbf{r},t)\tilde{E}_y(\mathbf{r},t) \\ 0 \end{pmatrix}. \tag{4.5.5}$$

In order to save computational cost, we omitted factors in Eq. (4.5.5) that depend upon $\tilde{E}_z\left(\mathbf{r},t\right)$ and the weakest d_{22} component of $\chi^{(2)}$ tensor. Due to symmetry of the geometry, scattered $\tilde{E}_y\left(\mathbf{r},t\right)$ and $\tilde{E}_z\left(\mathbf{r},t\right)$ components are almost equal in strength and share the same symmetry properties. Therefore, by omitting one we do not lose any essential information. However, this helps us save a significant amount of computational effort which is already quite high owing to the size and discretization requirements. In each case, it should be noted that the nonlinear polarization response would be dominated by $d_{33}(\mathbf{r})\tilde{E}_x^2(\mathbf{r},t)$ term in Eq. (4.5.5).

Illuminating the periodic array with a continuous-wave (CW) pump at $\nu^{\mathrm{F}} = 277\,\mathrm{THz}$ and carrying 13 mW power per unit cell, we computed the power flux in transmission at SH through a single periodic cell. Figures 4.5.2(a) and (b) show the results of the same two specific cases of cap and length detuning discussed earlier in Figs. 4.5.1 above. Although the considerations of numerical stability forced use considerably weaker pump power than what was used (1 W) to compute γ, an order of magnitude enhancement is still observed in the generated SH when the geometrical parameters coincide with the doubly resonant configuration (Fig. 4.5.2). This clearly demonstrates the prediction made by the nonlinear coupling coefficient γ.

The cases discussed until now consider geometric schemes in which the antenna is either resonant at both the FH and SH or at none. In order to fully distinguish the advantage of working with multiply-resonant schemes over the singly-resonant ones, we will now consider antenna geometries in which only one of the two frequencies induce resonant response when illuminated at the same CW frequency $\nu = 277\,\mathrm{THz}$. Figure 4.5.3(a) shows the geometric configuration for this purpose. The red curve provides the configuration in which the antenna remains resonant at FH whereas the dashed blue specifies the same at SH. At the intersection of the two curves we recover the doubly-resonant scheme used before. Since majority of the antenna designs are made to be resonant at FH, we choose

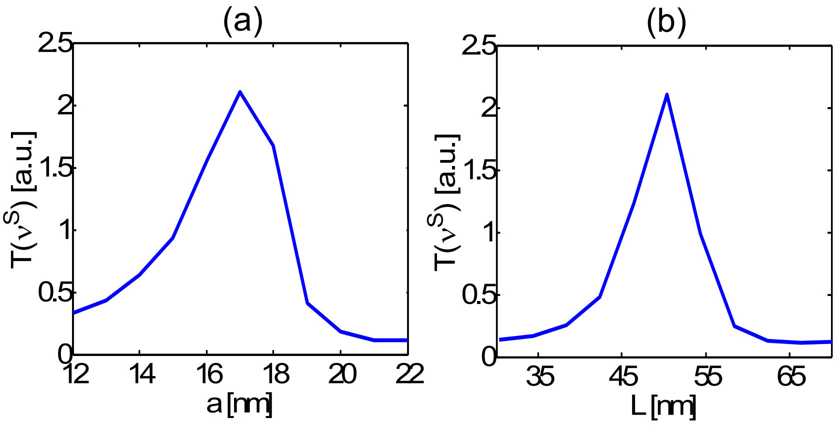

Figure 4.5.2: (a) Power transmission flux as computed from nonlinear FDTD simulation. Periodic cells were illuminated with CW pump of 13 mW power at input frequency $\nu = 277\,\text{THz}$. Part (a) shows the effect of detuning the cap radius a ($L = 50\,\text{nm}$) while (b) plots the length L ($a = 17\,\text{nm}$) being detuned from their resonant values of $a = 17\,\text{nm}$ and $L = 50\,\text{nm}$, respectively.

to work with the red-curve in which FH is always resonant in order to clearly observe the relative advantage of reaching the doubly resonant design. Figure 4.5.3(b) plots the linear transmission spectrum for a few chosen configurations according to Fig. 4.5.3(a) by modifying the cap and length simultaneously. The FH is found to be always resonant at $\nu^{\mathrm{F}} = 277\,\text{THz}$ but the third-order FP resonance gets detuned from the corresponding SH frequency with changing geometrical configurations.

Figure 4.5.3(c) scans the value of $|\gamma|$. The bright line in Fig. 4.5.3(c) at $\nu^{\mathrm{F}} = 139\,\text{THz}$ shows no geometrical dependance because the antenna is always resonant at the corresponding SH. But the bright line around $\nu^{\mathrm{F}} = 277\,\text{THz}$ is slanted indicating a prominent dependance upon the SH resonance of the antenna which keeps changing for different geometrical configurations. Figure 4.5.3(d) shows the computed SH transmission spectrum in nonlinear FDTD-simulations whose computational details are the same as described earlier. The peak for the largest second harmonic signal is reached in Fig. 4.5.3(c) for $a = 18\,\text{nm}$ which is close enough to the predicted value of $a = 17\,\text{nm}$. This minor deviation can be attributed to disparity between the numerical methods - FEM for the analytical prediction while the FDTD-method was employed for nonlinear computations. However, overall we see an excellent agreement and a clear demonstration of the positive impact doubly resonant antennas can have on enhancing the efficiency of nonlinear interaction.

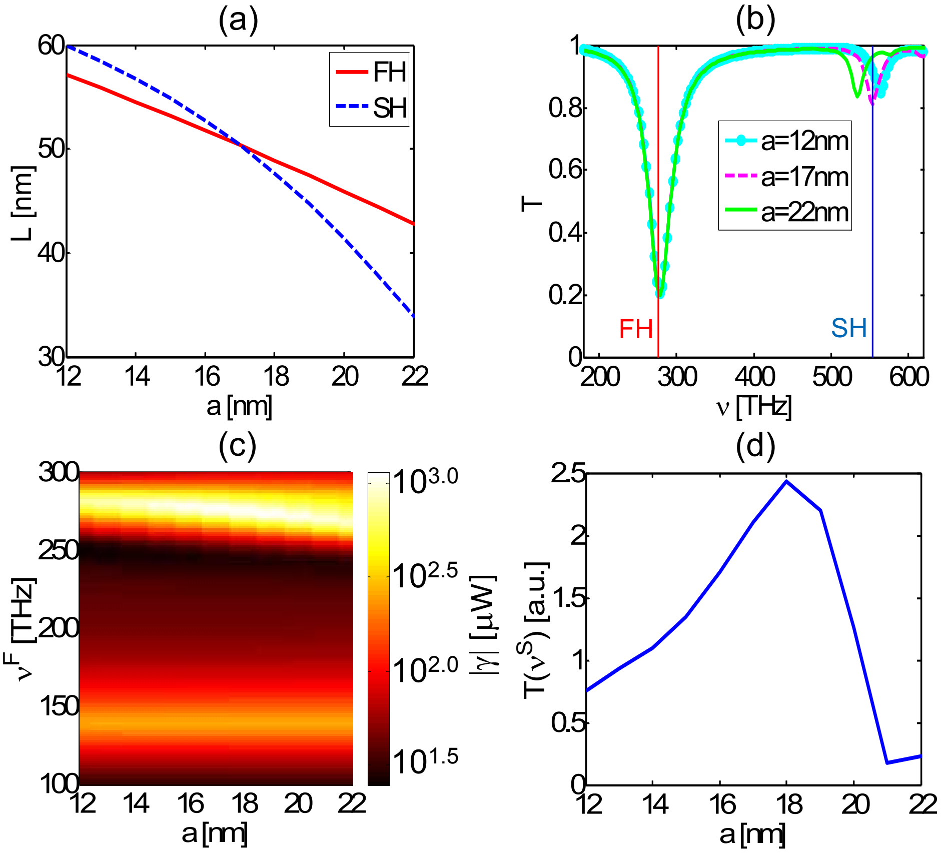

Figure 4.5.3: (a) Antenna configuration at $\nu^{\mathrm{F}} = 277\,\mathrm{THz}$ when FH has FP resonance of 1st and SH of 3rd order. (b) Linear transmission spectrum and (c) nonlinear mode overlap $|\gamma|$ are shown when the antenna is kept resonant at FH according to (a). Likewise, the transmission spectrum of nonlinear FDTD-simulations is shown in (d) when the structure is illuminated with a pump of $\nu^{\mathrm{F}} = 277\,\mathrm{THz}$.

4.6 Other example: Core-shell antenna

In the foregoing sections we demonstrated the potential of cylindrical metallic antennas with semi-ellipsoidal caps to act as a doubly-resonant platform for enhancing degenerate SH generation. In this section, we briefly present, without repeating complete analysis, a simple extension of the above scheme to present another example of the practical possibilities that exist in employing this design methodology.

Instead of a bare-metal antenna, we now consider a core-shell geometry in which the cylindrical dielectric core is layered with a thin metallic shell. The whole geometry is terminated with semi-ellipsoidal caps which in our case are made up of the same core-shell structure. In this scheme, we therefore have thickness of the metallic shell as

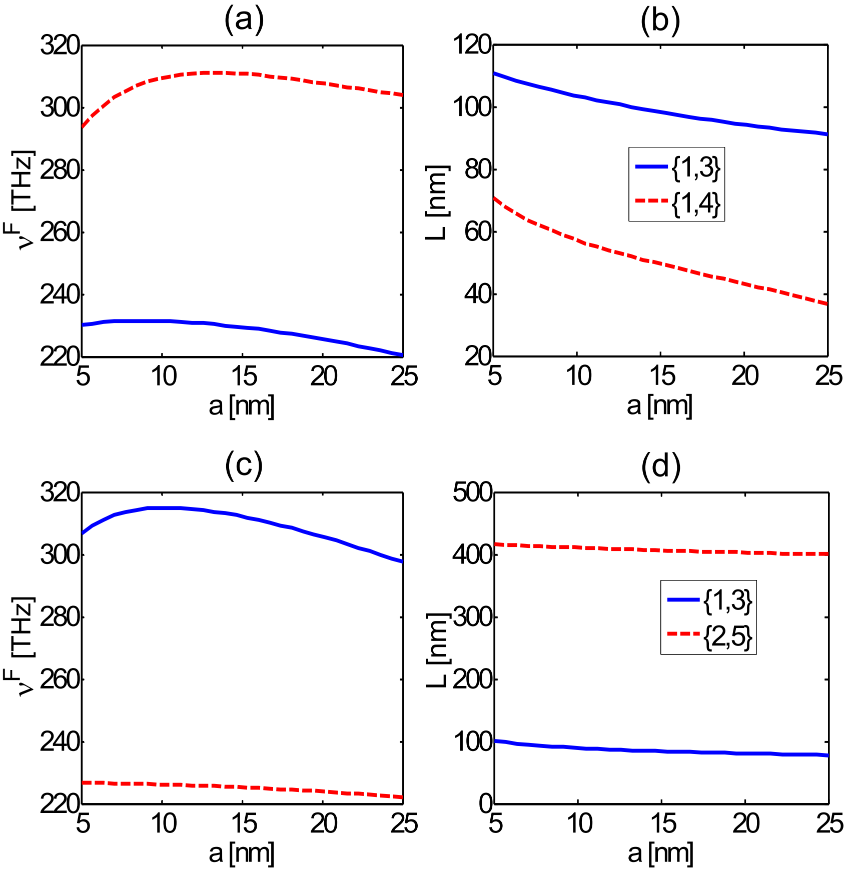

Figure 4.6.1: (a) Doubly resonant configurations for FP order m, n showing (a) the pump frequency ν_{FH} and (b) length L for the given cap radius a when thickness of the shell is 5 nm. Parts (c) and (d) show the same result for shell thickness of 10 nm.

another degree of freedom in addition to the semi-axis of the semi-ellipsoidal core that was considered before. As such, it is the same geometry that was considered earlier in Fig. 3.1.1(b) except that now we allow length of the antenna to be non-zero. These geometries have already been considered for the linear tunability of resonant scattering in particle form ($L = 0$) [113] and SH generation due to non-centrosymmetric medium in the core [148]. Therefore, it is of practical interest to consider further possibilities for materializing their full potential for nonlinear applications.

Figure 3.1.1 sketches the geometrical configuration that support resonances at both FH and SH by using the method outlined in the foregoing sections. Also included is the FP order of the modes sustained by these configurations. We only consider shell thicknesses of 5 nm [Figs. 3.1.1(a) and (b)] and 10 nm [Figs. 3.1.1(c) and (d)] here although other values are possible too. However, it adequately establishes the possibility to further explore our antenna design methodology for similar structures of practical interest.

4.7 Concluding remarks

In conclusion, we demonstrated the possibility of designing simple yet highly efficient plasmonic antennas for the purpose of strong nonlinear frequency mixing. By utilizing the high frequency and geometrical dispersion of the reflection phase jump of the guided SPP mode at terminal cap, we managed to design FP cavities that exhibited resonant response at both the frequencies involved in degenerate SH generation. By means of a semi-analytical approach to the nonlinear interaction, the superiority of multiply-resonant schemes was predicted over singly-resonant ones. Further characterization of the predicted nonlinear enhancement was confirmed through rigorous FDTD simulations. In the end, we also considered a simple extension of this work by considering antennas made up of a cylindrical dielectric core cladded with thin metallic shell. It was found that following a similar design methodology conveniently uncovered existence of geometrical parameters which are highly optimized for nonlinear interaction thanks to the resonances of various FP orders at both FH and SH frequencies. It should be interesting to see if experimental methods for fabricating these geometries can cope up with the challenge of meeting stringent design requirements suggested by our results.

At the end, we note that some results of this chapter have already appeared in our publication found in Ref. [149]

5 Nonlinear interaction in slot waveguides

5.1 Introduction

In this chapter we will be finally considering guided wave phenomenon in its own light. Like in dielectric integrated optics platform, plasmonic waveguides are seen to be a potential candidate for routing on-chip communication at a scale much smaller than the half-wavelength limit [5]. While the linear properties of plasmonic waveguides are interesting enough for the said reason, they too are viewed with the same kind of opportunism to observe enhanced nonlinear phenomena as in structures sustaining localized plasmonic resonances [134, 150–159]. However, most of the times, attention has been given to 2D waveguides which guide light only in one dimension that is perpendicular to the propagation direction. This helps in making a large part of the problem, if not whole, analytically accessible. At the same time, however, it poses the question of correspondence of the results thus obtained to practical devices which are necessarily bounded in both dimensions transverse to propagation. In the same vein, diffraction spread of the beam also remains unaccounted in cases when the beam width of the launched mode is much smaller compared to either of the transverse dimension of waveguide core on the cross-section plane. Addressing the latter, it was shown with the help of third order polarization response that the diffractive spread of the propagating plasmonic modes can be arrested at sufficiently high intensities by means of plasmon-solitons [160–162]. The second order nonlinear response is always much stronger in non-centrosymmetric media but poses additional overhead of phase mismatch owing to dispersion effects of the waves interacting at distinct frequencies [87]. To circumvent this problem, quasi-phase-matching (QPM) by periodically poling the nonlinear dielectric was considered to obtain steady conversion of energy from the pump at fundamental harmonic (FH) to second harmonic (SH) in an insulator-metal-insulator (IMI) geometry [163]. Although QPM in principle can always compensate the phase-mismatch, it remains practically challenging to implement it in an actual device and has an additional side-effect of decreasing the strength of effective nonlinearity by a factor corresponding to the discrete Fourier order employed to balance the phase-mismatch [87].

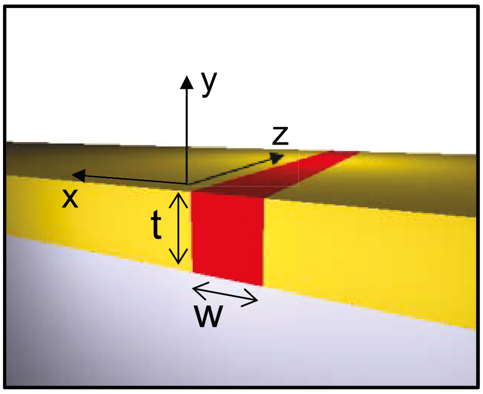

Figure 5.1.1: Schematic illustration of the metallic slot waveguides. Thickness and width are denoted by t and w respectively.

Another possibility for achieving phase matching is to exploit distinct modal dispersion present in waveguides between disparate modes to obtain steady nonlinear interaction. In dielectric waveguides, it is a well reported method to achieve phase-matched quadratic conversion between modes of different orders at FH and SH by optimizing geometrical parameters of the waveguide [164–167]. However, it comes at the cost of a reduced mode overlap which is always less when compared to the interaction of modes with the same order at FH and SH. For plasmonic waveguides, it was recently shown that the width of metal-insulator-metal (MIM) waveguides can be optimized to phase-match quadratic interaction between the symmetric mode at FH and anti-symmetric mode at SH [168]. In yet another report, the same modal phase matching was used to parametrically amplify the plasmonic mode propagating at FH through the TM_1 photonic mode at SH by varying the thickness of dielectric layer deposited on the semi-infinite metallic substrate [169].

As stated earlier, the potential for enhanced nonlinear effects in 3D plasmonic waveguides which guide light in both transverse directions has attracted comparatively less attention. Metallic slot waveguides (Fig. 5.1.1) are one well-known example which were tailored to be an efficient source for producing coherent THz radiation by down-converting from optical frequencies [170]. These waveguides happen to be one of the most straightforward 3D extensions of the 2D MIM waveguides [26]. Whilst retaining high field confinement, which is the hallmark of MIM waveguides, they also introduce a whole new range of plasmonic modes as opposed to the symmetric and anti-symmetric modes realizable in the simple MIM geometries [26].

It is the objective of this chapter to explore the potential of metallic slot waveguides for efficient frequency mixing in the presence of quadratic nonlinearity. In particular, we will consider degenerate SH generation in the presence of a dielectric medium possessing strong quadratic nonlinear response. But the significance of our results should make a strong case for further methodologically similar exploration for the enhancement of full breadth of phenomena possible in three and even four wave mixing processes, the latter in the context of a cubic nonlinear response. As an example of the application of our results, we will consider parametric amplification of a weak low-frequency mode with a strong high-frequency pump mode at SH. Given the short propagation distances of modes in plasmonic waveguides, this can have a far-reaching implication on the ongoing drive toward realization of practical plasmonic circuits. With that said, it is instructive to recall that extending the propagation length to infinity by fully compensating the metallic damping is never a necessary objective for practical purposes. Extending the propagation length by twice the original scale can also push the frontiers of plasmonic devices to practical limits for certain applications.

In the following sections we will present the modes sustained by slot waveguides and the theoretical framework used in our investigations, followed by results from both SH generation as well parametric amplification of the mode at FH.

5.2 Modes in slot waveguides

Any exposition of modes in slot waveguides (Fig. 5.1.1) necessarily involves reference to 2D MIM waveguides which are thoroughly treated in standard texts on plasmonics (for example, see [2]). Therefore, we will overstep detailed derivations and be content with delineating essential results and features which are necessary to understand the actual problem at hand.

MIM Waveguide

MIM waveguides are formed by bringing two metal-dielectric interfaces in close proximity such that the guided SPP mode supported at each interface strongly couples with the other. This leads to a splitting of modes into even and odd branches which are hereby characterized with respect to the symmetry of the longitudinal electric field component.

The dispersion of mode number $\beta(\nu)$ is defined through the following transcendental equations as [2]

$$\tanh\left[\frac{k_{\mathrm{d}}(\nu)\,a}{2}\right] = -\frac{k_{\mathrm{m}}(\nu)\,\varepsilon_{\mathrm{d}}(\nu)}{k_{\mathrm{d}}(\nu)\,\varepsilon_{\mathrm{m}}(\nu)} \tag{5.2.1}$$

for odd symmetry and

$$\tanh\left[\frac{k_{\mathrm{d}}(\nu)\,a}{2}\right] = -\frac{k_{\mathrm{d}}(\nu)\,\varepsilon_{\mathrm{m}}(\nu)}{k_{\mathrm{m}}(\nu)\,\varepsilon_{\mathrm{d}}(\nu)} \tag{5.2.2}$$

for even parity. In Eqs. (5.2.1, 5.2.2), dielectric permittivities of metal and dielectric media are denoted by $\varepsilon_{\mathrm{m}}(\nu)$ and $\varepsilon_{\mathrm{d}}(\nu)$ respectively while thickness of the dielectric film is a. The wave number $\beta(\nu)$ is defined in terms of $k_{\{\mathrm{m,d}\}}(\nu)$ as

$$\beta(\nu) = \sqrt{k^2_{\{\mathrm{m,d}\}}(\nu) - k_0^2(\nu)\,\varepsilon_{\{\mathrm{m,d}\}}(\nu)}, \tag{5.2.3}$$

where $k_0(\nu) = 2\pi\nu/c$ is the vacuum wave number with c being velocity of light in the vacuum. Since the even parity mode is mostly cut-off and is found propagating only for special geometrical configurations near the bulk plasma frequency, we will ignore it henceforth. The odd parity mode, however, never cuts-off and is therefore responsible for most of the field dynamics that dominates the behavior of more complexly shaped waveguides formed out of MIM geometries. Therefore, it suffices to look at the important features of odd symmetry mode here. Figure 5.2.1 shows the mode profile as well as the dispersion of modes for an MIM geometry made up of Ag [105] and a dielectric film of dispersion-less dielectric permittivity $\varepsilon_{\mathrm{d}} = 4.84$.

In Fig. 5.2.1, we observe the effect of mode coupling between the metal-dielectric SPP modes for varying thicknesses of the dielectric film. For stronger coupling, i.e. smaller film thickness, the wave number assumes larger values and so does the concomitant propagation loss due to larger field penetration into the metal [Fig. 5.2.1(d)]. This is a necessary trade-off between larger field confinement that is achieved with smaller film thicknesses and propagation losses. The same goes for the resonance [around $\nu =$ 720 THz in Fig. 5.2.1(c)] where the propagation loss tends to dominate any other feature of the system. Therefore, for most problems of practical interest, it benefits more to operate at frequencies much lower than resonance.

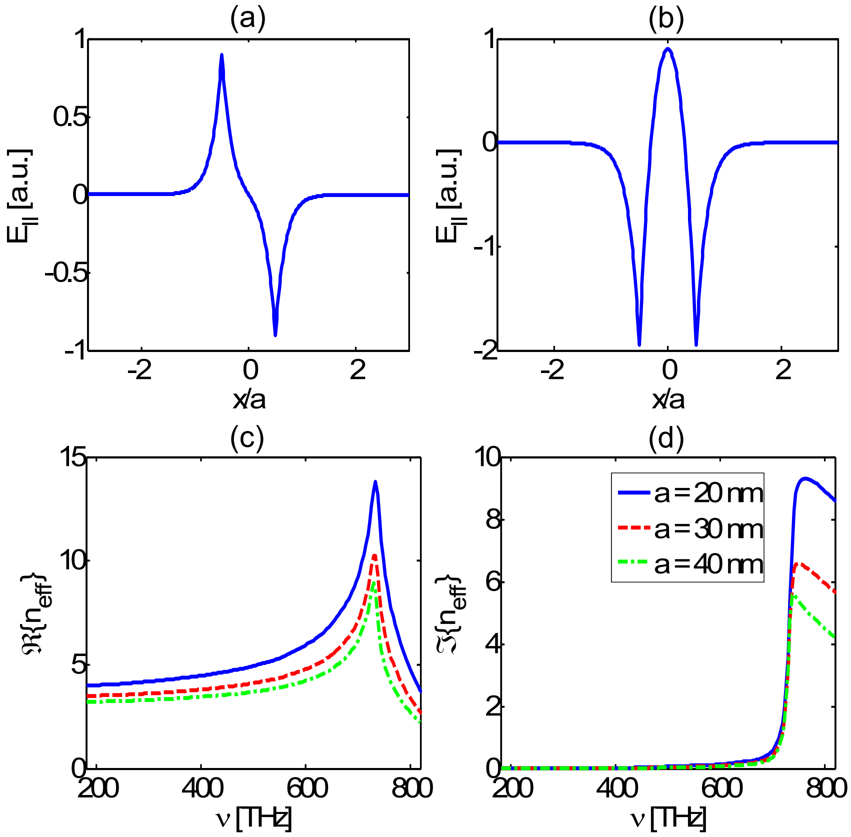

Figure 5.2.1: Cross-sectional profile of the longitudinal component of electric field $\left(E_{\parallel}\right)$ component of the (a) odd [Eq. (5.2.1)] and (b) even modes [Eq. (5.2.2)] supported by MIM waveguides having a dielectric film of thickness a. Dispersion of the real (c) and imaginary (d) parts of the effective mode index $\left(n_{\text{eff}}\left(\nu\right)=\beta\left(\nu\right)/k_0\right)$ of odd-parity mode supported by the MIM waveguide for various values of film thickness.

Slot waveguide

Slot waveguides are the simplest 3D extension of MIM waveguides by clipping the indefinitely extending dimension of the waveguide to finite lengths (Fig. 5.1.1). Like the MIM waveguide, a slot waveguide can be essentially understood to support the same even and odd modes with respect to the longitudinal electric component (E_z in Fig. 5.1.1) formed by the hybridization of modes at metal-dielectric interface. Much like the MIM waveguide, the even mode is visible only near the plasma frequency and that too for special frequency bands and geometrical configurations. The odd mode, however, remains accessible and is responsible for the fundamental and higher mode orders depending upon the thickness and wavelength of light (Fig. 5.2.3). For characterizing the waveguide, we once again take metal to be Ag, dielectric core to be $\mathrm{LiNbO_3}$ (optics axis parallel to the x-axis according to Fig. 5.1.1), substrate to be dispersion-less $\mathrm{SiO_2}$ ($\varepsilon_\mathrm{r} = 1.96$) and air as cladding. Since the problem is not amenable to analytical solution, we resort to FEM based mode solver Comsol Multiphysics to find the modes. Figures 5.2.2(a-c) show the $E_x(\mathbf{r})$ field distribution of the mode for mode orders $L = \{0, 1, 2\}$. Field symmetry is further highlighted in Figs. 5.2.2(d-f) along y-axis defined according to Fig. 5.1.1. Figure 5.2.3 plots the frequency dispersion of the same modes for constant values of width and thickness of the waveguide (Fig. 5.1.1) over the frequency range of interest. As expected, we observe the higher order mode ($L = 2$) to be cut-off (n_eff less than maximum core index which is around 2.2) at lower frequencies. However, the terminology of mode cut-off in the context of slot waveguides that we are discussing only signifies a loss of sub-wavelength confinement. They in fact continue to propagate while guided within the core until the n_eff becomes smaller than the refractive index of the surrounding substrate after which they start leaking power in the substrate as they propagate. But since we are primarily interested in sub-wavelength guiding feature of slot waveguides, we will not be taking any practical interest in the modes that are cut-off.

Like the physical parameters, modes guided in the slot waveguides are also sensitive to geometrical features of the system. Figure 5.2.4 exposes the dependence of modes on width and thickness of the dielectric slot shown in Fig. 5.1.1(a). Figures 5.2.4(a) and (b) plot the dependance of mode of order $L = 0$ for various values of slot width. Expectedly, the smaller the width, the larger the effective mode index (and loss) owing to tighter packing of modes between metallic boundaries. Increasing the thickness, however, allows the mode to asymptotically stabilize to a value corresponding to that of the even mode in 2D MIM waveguide. Figures 5.2.4(c) and (d) show the modal dependance of various orders for a fixed width ($w = 20\,\mathrm{nm}$) and thickness. Like before, we find the modes to

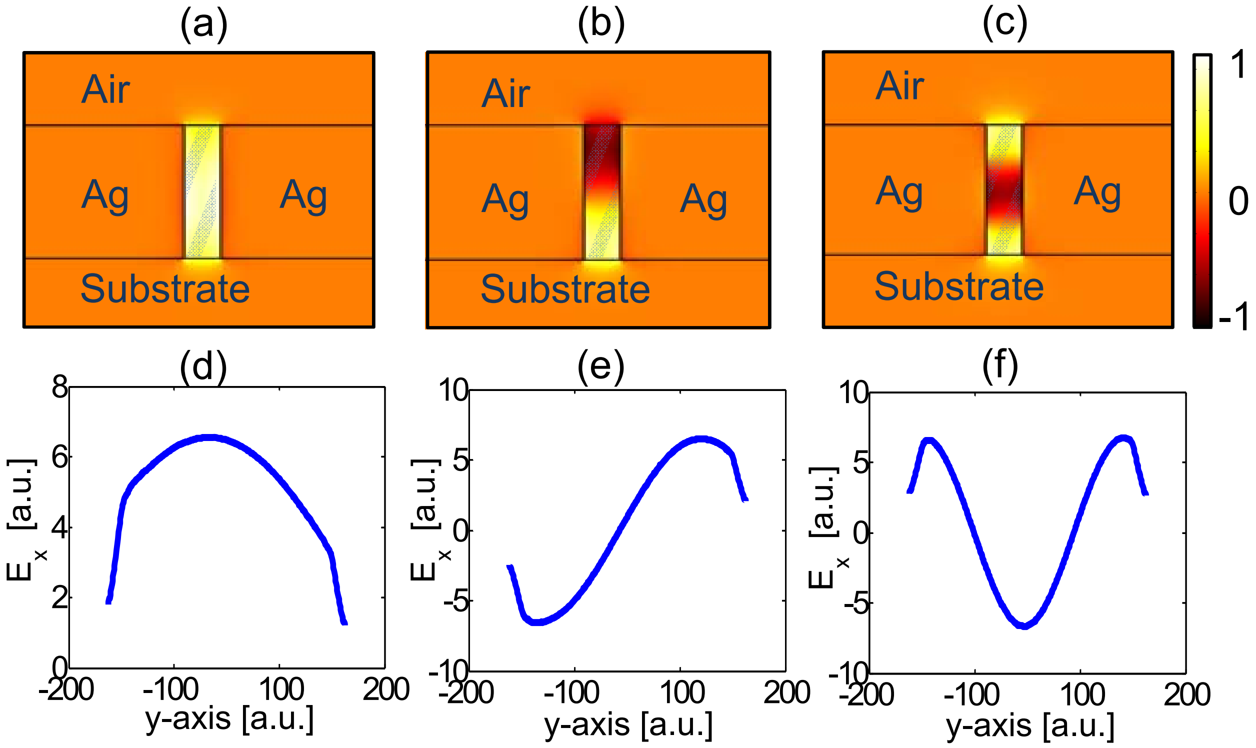

Figure 5.2.2: Modal distribution of the electric field's x-component according to the coordinate frame shown in Fig. 5.1.1 for mode order $L = 0$ (a), $L = 2$ (b) and $L = 3$. Dielectric core (shaded) is made up of $LiNbO_3$ while the dielectric substrate is SiO_2 ($\varepsilon_{\mathrm{r}} = 1.96$). Parts (d-f) show the profile of E_x along y-axis (Fig. 5.1.1) in the core to highlight symmetry of the modes shown in (a-c) respectively.

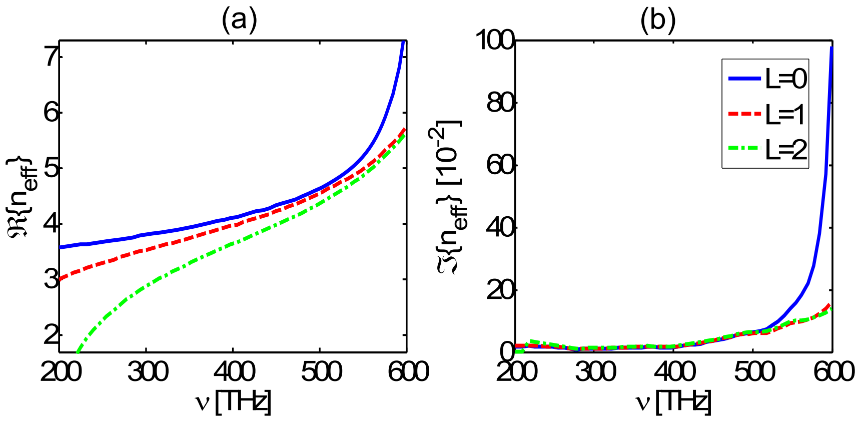

Figure 5.2.3: Frequency dispersion of various mode order L shown in Figs. 5.2.2(a-c). (a) shows the real and (b) imaginary part of effective mode index. Width and thickness have been taken to be 50 nm and 100 nm respectively.

become more or less insensitive to the thickness for sufficiently large values. For smaller values, however, the imaginary part of mode index [Fig. (5.2.4)(d)] suddenly declines below the cut-off point indicating lower losses that should be associated for the modes which are localized primarily in the dielectric core rather than on the metal-dielectric interface.

The high field confinement, which is the hallmark of MIM waveguides and existence of high sensitivity to geometrical and physical features, prompts us to investigate the possibility of tailoring the system in order to optimize the efficiency of degenerate SH generation. Like before, we have chosen the degenerate SH generation owing to its simplicity of concept together with the diversity of forms in which it finds applications such as generation of $\chi^{(2)}$ solitons, parametric amplification, optical diode etc. In the following, we will briefly reproduce the relevant results derived in detail in Sec. 2.5 that describe the interaction of guided modes in a quadratic medium.

5.3 Coupled mode theory

Considering the waveguide to be mono-mode at FH and multi-mode at SH, we define the modes at each harmonic as:

$$\mathbf{E}_0(\mathbf{r},\nu^{\mathrm{F}}) = A\left(z\right)\mathbf{e}_0^{\mathrm{F}}\left(x,y\right)\exp\left(\iota\beta_0^{\mathrm{F}\prime}z\right) \tag{5.3.1}$$

for FH and

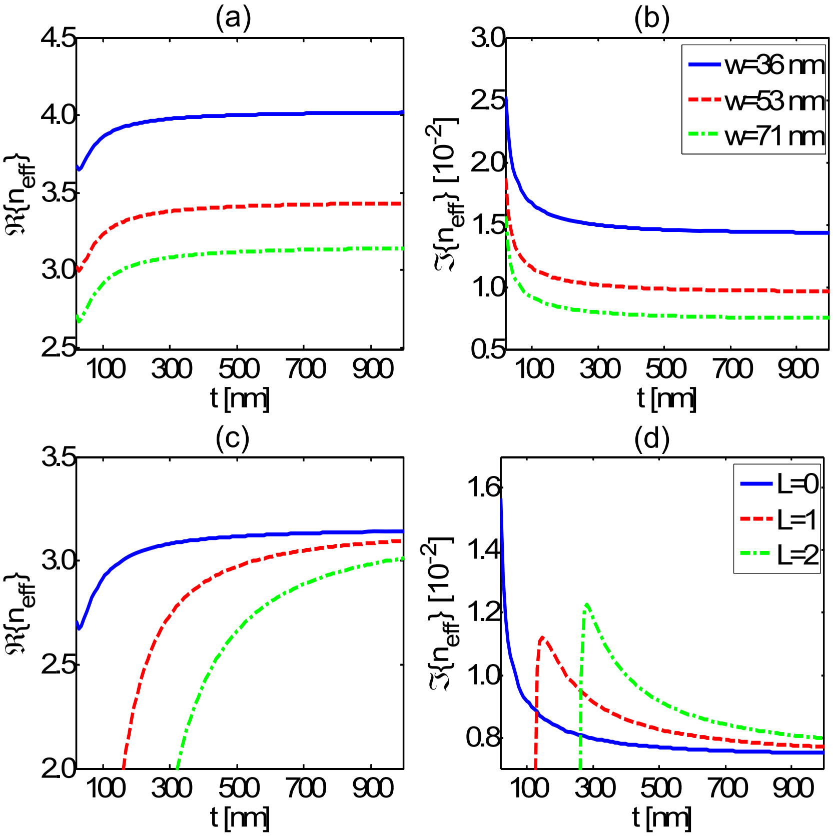

Figure 5.2.4: Geometric dispersion of slot waveguides. (a) and (b) show the dispersion of mode order $L = 0$ order as a function of slot thickness and width while (c) and (d) plot the dependence of modes of various order L on thickness t for a fixed width ($w = 20\,\text{nm}$). Modes were evaluated in all figures at telecom wavelength $\lambda = 1.55\,\mu\text{m}$.

$$\mathbf{E}_m(\mathbf{r},\nu^{\mathrm{S}}) = B_m\left(z\right)\mathbf{e}_m^{\mathrm{S}}\left(x,y\right)\exp\left(\iota\beta_m^{\mathrm{S}\prime}z\right) \tag{5.3.2}$$

for SH. In Eqs. (5.3.1) and (5.3.2) above, field distribution of the complex vectorial mode is denoted by $\mathbf{e}_m^{\{\mathrm{F,S}\}}\left(x,y\right)$ where the subscript m denotes the mode order and superscripts F and S represent the FH and SH frequencies respectively. The mode order for FH in Eq. (5.3.1) is already specified since we shall be considering only mono-mode configuration at FH. Nonlinear interaction and linear propagation loss are accounted for through the mode envelopes $A\left(z\right)$ and $B_m\left(z\right)$. If the modes at FH and SH are normalized to unit power, then the power contained in the mode at any point z along the propagation path is directly obtained through $|A(z)|^2$ and $|B_m\left(z\right)|^2$. Linear phase accumulation along the propagation direction z is described by $\beta_m^{\{\mathrm{F,S}\}\prime} = \Re\left\{\beta_m^{\{\mathrm{F,S}\}}\right\}$ where $\beta_m^{\{\mathrm{F,S}\}}$ is the complex mode propagation wave number. With this, we can rewrite Eqs. (2.5.23) from Sec. 2.5 as

$$\begin{aligned}\frac{dA\left(z\right)}{dz} &= -\beta_0^{\mathrm{F}\prime\prime}A\left(z\right) + \iota\sum_m \gamma_m^{\mathrm{F}}A^\star\left(z\right)B_m\left(z\right)\exp\left(\iota\Delta\beta_m z\right), \\ \frac{dB_{\mathrm{M}}\left(z\right)}{dz} &= -\beta_{\mathrm{M}}^{\mathrm{S}\prime\prime}B_{\mathrm{M}}\left(z\right) + \iota\gamma_{\mathrm{M}}^{\mathrm{S}}A^2\left(z\right)\exp\left(-\iota\Delta\beta_{\mathrm{M}}z\right),\end{aligned} \tag{5.3.3}$$

where $\Delta\beta_m = \Re\left\{2\beta_0^{\mathrm{F}} - \beta_m^{\mathrm{S}}\right\}$ is the nonlinear phase-mismatch, $\beta_m^{\{\mathrm{F,S}\}\prime\prime} = \Im\left\{\beta_m^{\{\mathrm{F,S}\}}\right\}$ is the linear damping of the mode and $\gamma_m^{\{\mathrm{F,S}\}}$ is the mode overlap computed according to Eq. (2.5.22). In the following section, we will numerically attempt to solve the system of Eqs. (5.3.3). As already discussed in detail in Sec. 2.5, phase-mismatch $\Delta\beta_m$ determines oscillations in energy conversion cycle from one harmonic to another while $\gamma_{\mathrm{m}}^{\{\mathrm{F,S}\}}$ determines the nonlinear coupling strength already defined in Eqs. (2.5.22).

5.4 Numerical results

In finding the solution to Eqs. (5.3.3), we set out to search for cases that minimize the phase-mismatch $\Delta\beta_{\mathrm{m}}$ and maximize the mode coupling coefficient $\left|\gamma_m^{\{\mathrm{F,S}\}}\right|$. In the following sub-sections we discuss each of them in order.

5.4.1 Phase-mismatch

The phase-mismatch factor $\Delta\beta_m$ in Eqs. (5.3.3) can be equivalently written in terms of effective mode index as:

$$\Delta\beta_m = 2\pi\frac{\nu^{\mathrm{S}}}{c}\left(n^{\mathrm{S}\prime}_{\mathrm{eff},m} - n^{\mathrm{F}\prime}_{\mathrm{eff},0}\right), \tag{5.4.1}$$

where c is the vacuum velocity of light, ν^{S} the SH frequency and $n^{\{\mathrm{F,S}\}\prime}_{\mathrm{eff},m}$ is the real part of effective mode index of order m. For non-oscillating conversion of energy, we require $\Delta\beta_m$ to be zero which implies $n'^{\mathrm{S}}_{\mathrm{eff},m} = n'^{\mathrm{F}}_{\mathrm{eff},0}$. Therefore, we have to search for configurations in which both FH and SH have the same effective mode indices. In what follows, we will fix the FH at telecom wavelength ($\lambda = 1.55\,\mu$m) and optimize the geometry. Figure 5.4.2 shows the dispersion of modes for a fixed set of geometrical parameters. At the wavelength of choice and for sufficiently small geometrical dimensions ($w, t \lesssim 0.5\,\mu$m), there is only one fundamental mode ($l = 0$) having an effective mode index greater than the core. In this regime, higher order modes ($l \geq 1$) are delocalized out of the core and provide very small overlap with plasmonic modes at SH and at times are even radiative into the substrate. We will, therefore, restrict our attention to only fundamental mode $l = 0$ at FH. At SH, however, the modes are localized inside the core in the dimensions under consideration. Therefore, we will consider coupling to modes up to $m \leq 2$ at SH.

Figure 5.4.1 scans $\Delta n_m = \Re\left\{n^{\mathrm{S}}_{\mathrm{eff},m} - n^{\mathrm{F}}_{\mathrm{eff},0}\right\}$ over a range of geometrical parameters. We find that Δn_m exhibits no sign change for $m = 0$ order mode at SH indicating a lack of phase-matched configuration. For $m = \{1, 2\}$, however, Δn_m undergoes sign change indicating the existence of parameters where the phase matching condition is completely satisfied for the two modes at FH and SH respectively. Dark areas in Figs. 5.4.1(b) and (c) correspond to those configurations where the respective modes at SH are cut-off. Figure 5.4.2 plots the dispersion of phase-matched modes for select geometrical configurations as a function of FH frequency to provide an elaborate view of how the effective mode indices of modes at SH meet up with the one at FH.

5.4.2 Mode overlap

While the phase-mismatch factor $\Delta\beta_m$ describes the steady nonlinear conversion (or a lack thereof) from one frequency to another, mode overlap coefficients $\gamma^{\{\mathrm{F,S}\}}_m$ in Eq. (5.3.3) determine the strength of nonlinear interaction. In lossless systems, striking a phase-match guarantees complete energy conversion from the incident FH to SH. However, in

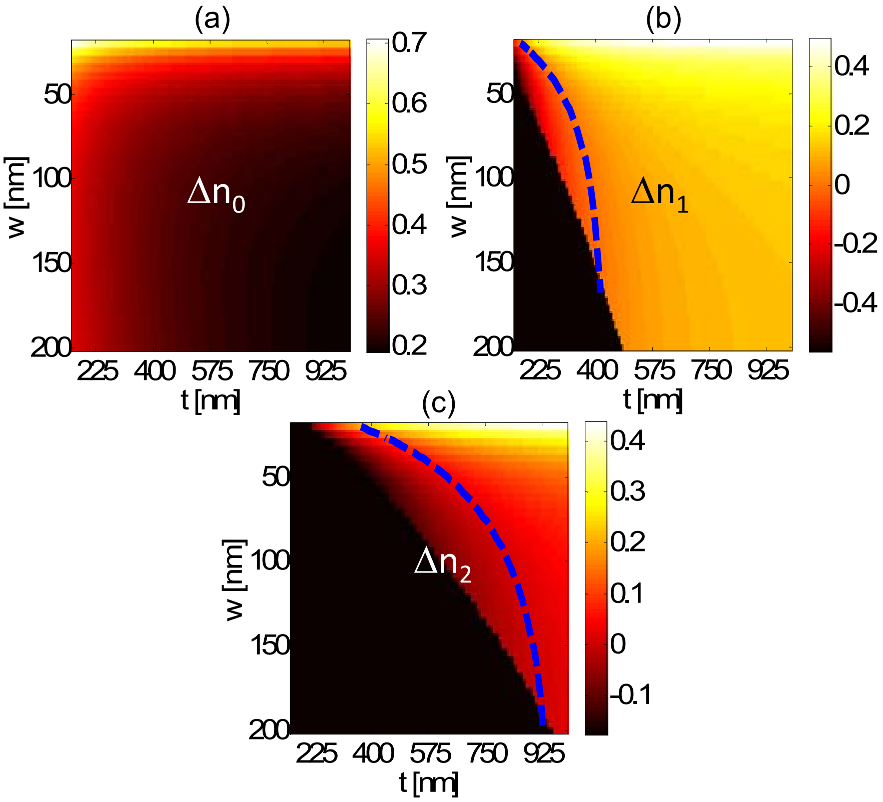

Figure 5.4.1: Phase mismatch Δn_m between $l = 0$ mode at FH and SH mode $m = 0$ (a), $m = 1$ (b) and $m = 2$ (c). Dashed blue curve indicates the line where phase matching takes place. Black area denotes regions in the parameter space where the SH plasmonic mode is cut-off.

plasmonic systems which are dominated by dissipation in the metal, a complete power conversion from FH to SH even when $\Delta\beta_m = 0$ is never accomplished. This is due to the fact that energy is depleted faster owing to linear damping which further causes the nonlinear interaction to grow weaker as the modes propagate. Therefore, in such lossless systems the mode overlap coefficient $\gamma_m^{\{\mathrm{F,S}\}}$ serves to provide at least a qualitative idea of the coupling strength that determines the rate at which an energy transfer takes place. It is instructive at this point to simplify Eqs. (2.5.22) in order to draw qualitative understanding of the results which we will discuss shortly. We note that the electric field component normal to metallic boundaries [E_x distribution in Figs. 5.2.2(a-c)] should always be the strongest and that the strongest. Therefore, the strongest d_{33} component of the nonlinear $\chi^{(2)}$ tensor of LiNbO$_3$ [87] should be aligned parallel to it to get maximum advantage. With this, Eqs. (2.5.22) can be approximated as

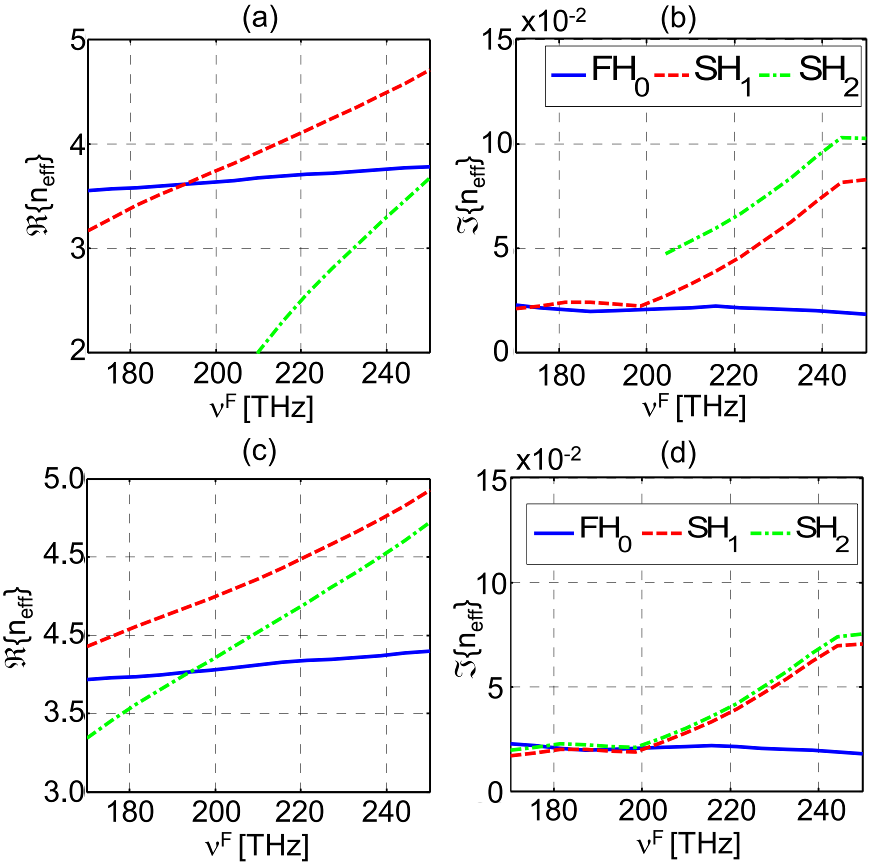

Figure 5.4.2: Linear dispersion of the modes. Horizontal axis defines the frequency of FH while the subscript of SH in the legend stands for the mode order. Width of the core is set to $w = 20\,\mathrm{nm}$. Thickness is defined as $t = 170\,\mathrm{nm}$ for (a) and (b) and $t = 360\,\mathrm{nm}$ for (c) and (d). $m = 2$ mode at SH shown in (a) and (b) undergoes cut-off near 210 THz.

$$\begin{aligned}
\gamma_m^{\mathrm{F}} &\backsimeq \frac{\nu^{\mathrm{F}}}{N_0^{\mathrm{F}}} \iint_{-\infty}^{\infty} d\mathbf{r}_\perp d_{33}\left(\mathbf{r}_\perp\right) \left|\mathbf{e}_{0,x}^{\mathrm{F}}\left(\mathbf{r}_\perp\right)\right|^2 \mathbf{e}_{m,x}^{\mathrm{S}}\left(\mathbf{r}_\perp\right), \\
\gamma_m^{\mathrm{S}} &\backsimeq \frac{\nu^{\mathrm{S}}}{N_m^{\mathrm{S}}} \iint_{-\infty}^{\infty} d\mathbf{r}_\perp d_{33}\left(\mathbf{r}_\perp\right) \mathbf{e}_{0,x}^{\mathrm{F}}\left(\mathbf{r}_\perp\right)^2 \mathbf{e}_{m,x}^{\mathrm{S}}\left(\mathbf{r}_\perp\right).
\end{aligned} \tag{5.4.2}$$

It is evident from Eqs. (5.4.2) that for there to observe a significant mode overlap, the x-component of the electric field of the mode at SH necessarily needs to have a symmetric distribution. The FH mode, however, gets squared and thus can have a symmetric and anti-symmetric profile. We take nonlinear coefficients of the LiNbO$_3$ tensor to be $d_{22} = 2.76\,\mathrm{pm/V}$, $d_{31} = 5.77\,\mathrm{pm/V}$ and $d_{33} = -31.8\,\mathrm{pm/V}$ [171] and compute the mode overlap coefficients of Eq. (2.5.22). Figure 5.4.3 maps the mode overlap coefficient $|\gamma_m^{\mathrm{S}}|$ at SH as a function of geometric parameters of the slot with all the modes normalized to unit power. The blacked out areas once again correspond to those configurations in which the SH mode is cut-off. Furthermore, in Fig. 5.4.3(b) we find another dark curve beginning from $\{t, w\} \approx \{200, 700\}$ nm which is due to the first order mode taking on anti-symmetric profile along the y-axis (Fig. 5.1.1). However, being away from the phase-matched configuration [Fig. 5.4.1(b)], it does not interest us for the purpose of nonlinear interaction and therefore we will not explore any further what could potentially be an interesting anomaly of the mode in its own right.

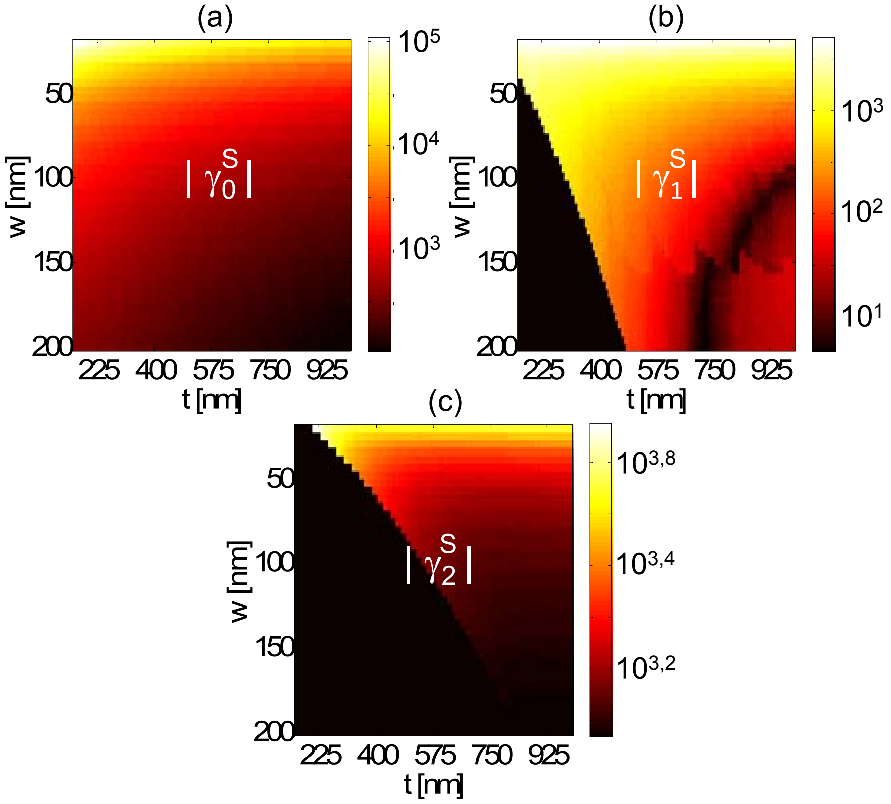

Figure 5.4.3: Mode overlap coefficient $|\gamma_m^{\mathrm{S}}|$ as defined in Eq. (2.5.22) between $l = 0$ mode at FH and SH modes of order $m = 0$ (a), $m = 1$ (b), and $m = 2$ (c). Linear modes have been normalized to unit power. Black area denotes regions in the parameter space where the SH plasmonic mode is cut-off.

According to Fig. 5.4.3, the highest values of $|\gamma_m^{\mathrm{S}}|$ is obtained for $m = 0$ while the lowest for mode order $m = 1$. This is because of the fact that the latter has an anti-symmetric profile of the strongest electric field x-component [Figs. 5.1.1(b) and (d)] which reduces the strength of overlap integral with symmetric $l = 0$ mode at FH in

Eq. (5.4.2). In case when both substrate and cladding are identical (not considered here), this value will reduce further to negligible limits as the modes assume perfectly symmetric or anti-symmetric character depending upon the specific polarization of the field. Before moving on, it should be pointed out that although $|\gamma_m^{\mathrm{S}}|$ is not equal to $|\gamma_m^{\mathrm{F}}|$, they share a proportional relationship with one another. As a matter of fact, it can be shown that in lossless systems and for the specific case of degenerate SH generation which is under consideration here, γ_m^{S} is exactly equal to γ_m^{F} (see Ref. [101] and further references therein). Therefore, in a qualitative discussion it suffices to speak in terms of either one of them.

We sum up the foregoing discussion by plotting in Fig. 5.4.4 phase-matched configurations obtained from Figs. 5.4.1(b) and (c) and the corresponding strength of nonlinear interaction determined through $|\gamma_m^{\mathrm{S}}|$ in Figs. 5.4.3(b) and (c). It is instructive to remark here the comparative advantage of working with metallic plasmonic waveguides over dielectric ones. If we substitute the metallic blocks in Fig. 5.1.1(a) with air and increase the dielectric core's width and thickness to 355 nm each, the maximum mode overlap coefficient $|\gamma_m^{\mathrm{S}}|$ turns out to be around $10^{2.54}$. This is an order of magnitude weaker than the maximum we can get in phase-matched configuration shown in Fig. 5.4.4(b). In case of identical modes interaction [Fig. 5.4.3(a)], the advantage is even higher although it is not the configuration of choice in most circumstances owing to phase-mismatch as discussed before.

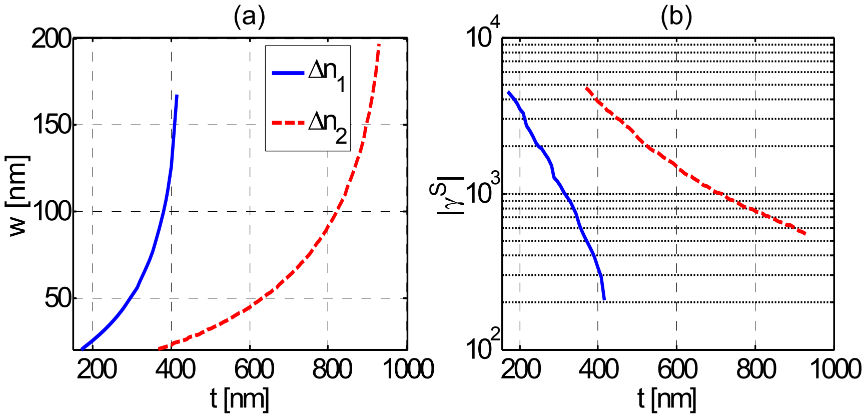

Figure 5.4.4: (a) Phase-matched configuration ($\Delta\beta_m = 0$) of the slot waveguide extracted from Fig. 5.4.1. (b) Value of nonlinear coupling coefficient $\left|\gamma_m^{\{\mathrm{F,S}\}}\right|$ at phase-matched points extracted from Fig. 5.4.3.

The knowledge of phase mismatch and mode overlap coefficients finally bring us to a position where we can quantify the output of the nonlinear interaction by numerically solving the coupled mode equations in Eq. (5.3.3). The linear modes at both FH and SH are normalized to unit power so that absolute squares of the mode envelopes $A(z)$ and $B_m(z)$ represent the amount of power in the modes at propagation distance z in an infinite waveguide. Without any loss of generality, the input pump power is taken to be 1 W which then gives $A(0) = 1$ and $B(0) = 0$ as the boundary conditions for solving the coupled differential equations in Eq. (5.3.3). Figure 5.4.5 scans the maximum conversion efficiency η_m from FH to SH defined in the units of $\%\mathrm{W}^{-1}\mathrm{cm}^{-1}$ as

$$\eta_m = \frac{\max\left\{\left|B_m\left(z\right)\right|^2\right\} 100\%}{\left|A\left(0\right)\right|^4 \kappa_m\left(\nu^{\mathrm{S}}\right)}, \tag{5.4.3}$$

where $\kappa_m(\nu^{\mathrm{S}})$ is the linear propagation length of SH mode in the unit of cm, $\left|B_m\left(z\right)\right|^2$ the power of the mode at SH and $\left|A\left(0\right)\right|^4$ the square of input pump power. Including propagation losses in the definition of conversion efficiency provides a better measure of the overall efficiency of the process given the finite propagation length of the SH modes involved.

Considering Fig. 5.4.5(a), we find that the larger mode overlap $\left|\gamma_m^{\mathrm{SH}}\right|$ (see Fig. 5.4.3) ensures that η_m always remains larger when the fundamental mode interacts with $m = 0$ at SH. This is valid even when $\Delta\beta_m$ goes to zero for $m = \{1, 2\}$ [Figs. 5.4.5(b) and (c)]. As already discussed at length, this is a direct consequence of the progressive depletion of the modal power due to metallic losses as the mode propagates forward.

It is instructive to highlight the underlying trade-off possible in working under phase-matched or higher overlap configuration. Figure 5.4.6 plots the evolution of SH mode envelope's amplitude $\left|B_m\left(z\right)\right|^2$ as a function of propagation distance for two different pairs of width and thickness. The two cases presented in Figs. 5.4.6(a,d) refer to the two extreme points in Figs. 5.4.3(b) and (c) where phase mismatch $\Delta\beta_m$ is zero to observe the maximum comparative advantages achievable through the two simultaneous nonlinear processes. In all the cases shown, the SH power $|B_0(z)|^2$ undergoes a comparatively larger rise due to stronger mode overlap in the beginning. However, sufficiently far away from the input at $z = 0$, $|B_2(z)|^2$ ultimately takes over with its steady rise due to $\Delta\beta_2 = 0$. This implies that in compact optical circuits designed for operation on nano-meter scale, the phase mismatch effects might become negligible and the feasibility will be completely determined by the value of mode overlap $\left|\gamma_{\mathrm{m}}^{\mathrm{S}}\right|$. This suggests that nonlinear mode interaction between modes of same order (i.e. $l = m = 0$) would be more useful. For long scale interaction, however, reducing the phase mismatch would be essential to observing significant SH conversion. Although the mode overlap is reduced,

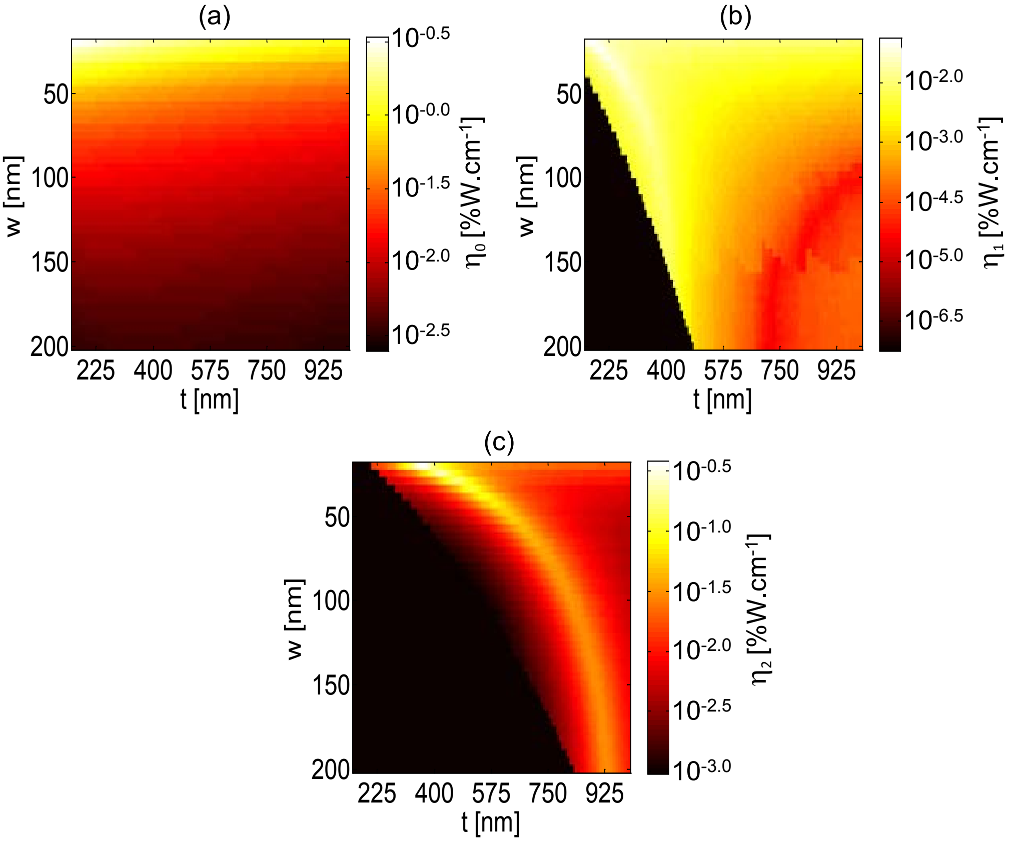

Figure 5.4.5: Nonlinear conversion efficiency η_m of the SH mode order $m = 0$ (a), $m = 1$ (b) and $m = 2$ (c). Input pump power of FH is equal to 1 W. Black area denotes regions in the parameter space where the plasmonic mode is cut-off.

it appears to be favorable to choose modes with different indices which can however be phase matched exploiting modal dispersion.

5.4.3 Parametric Amplification

Having obtained an understanding about the potential of slot waveguides for nonlinear interaction in both phase-matched schemes and otherwise, we are now in a position to suggest applications without necessarily involving any need for artificial schemes such as periodic poling of the nonlinear lattice or grating vector. Although plenty of applications can be gleaned up by looking at the existing literature on nonlinear effects in waveguides, we choose to explore the possibility of enhancing the propagation length of a weak seed signal at FH through parametric down-conversion of the pump at SH. It can be safely anticipated that such application could well be the most prominent $\chi^{(2)}$-effect

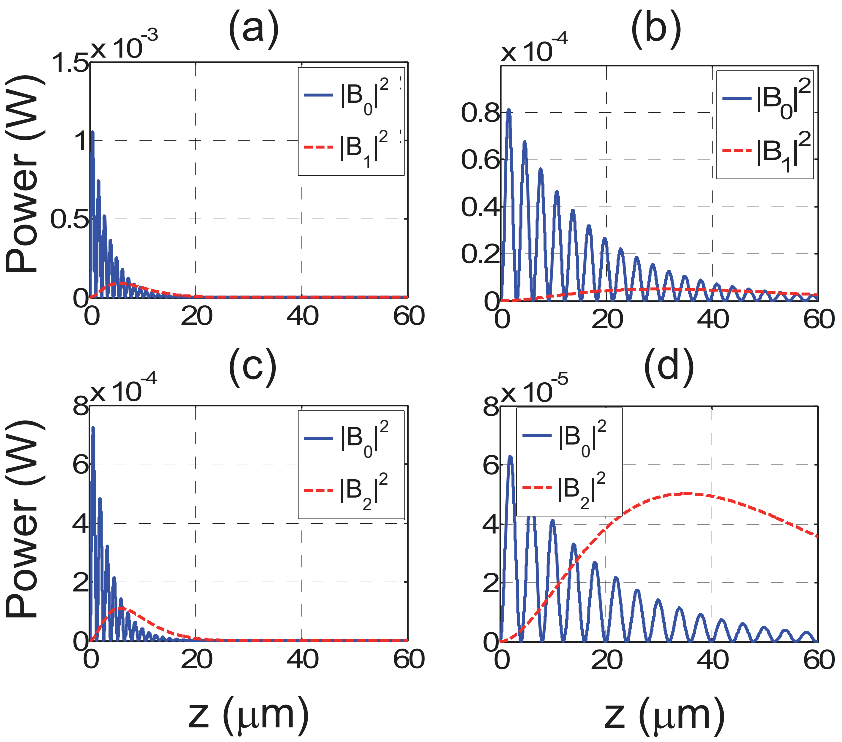

Figure 5.4.6: Evolution of SH power with propagation distance. (a) w = 20 nm, t = 170 nm. (b) w = 172 nm, t = 415 nm. (c) w = 20 nm, t = 360 nm. (d) w = 200 nm, t = 929 nm.

in the near-future given the fact that small propagation lengths of propagating SPPs is considered to be the biggest stumbling block toward realization of sub-wavelength optical circuits. Figure 5.4.7 shows the linear propagation length of the modes at phase-matched configuration, which is defined as the distance up to which the input intensity decreases by a factor of $\exp(-1)$ of its input strength. For the parametric interaction of modes, both $A(z=0)$ and $B_m(z=0)$ have non-zero amplitudes as input boundary conditions. For an input seed of 1 mW power at FH $\left(|A(z=0)|^2 = 10^{-3}\right)$, we scan the input pump power of SH at geometrical configurations taken from Fig. 5.4.1 for SH mode order $m = \{1, 2\}$ and disclose its impact on the propagation length for the seed signal at FH.

Figure 5.4.8 maps the length enhancement of the seed signal in form of the ratio δ between the maximum propagation length κ_{NL} in the presence of the pump beam relative to the linear propagation length κ_{LIN} as shown in Figs. 5.4.7(a) and (c). We point out that the propagation length of the seed signal is also a function of the relative input phase difference between the envelopes $A(z=0)$ and $B_m(z=0)$. In Fig. 5.4.8, however,

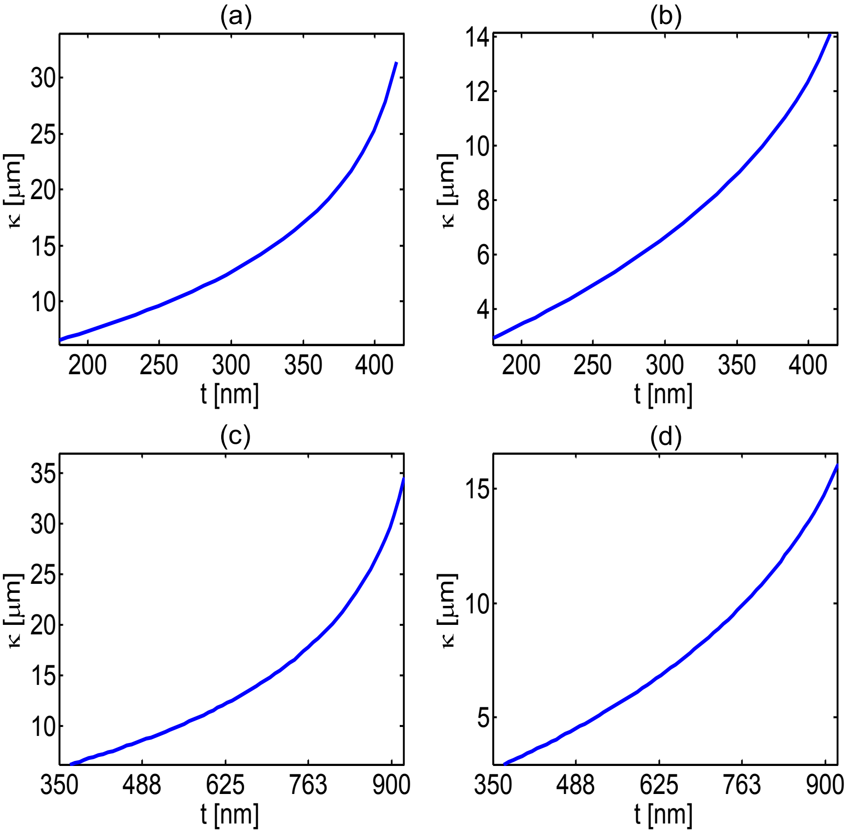

Figure 5.4.7: Linear propagation length κ of the modes at phase-matched configurations provided in Fig. 5.4.4(a). For $\Delta n_1 = 0$, propagation length of FH (a) and SH (b) are shown. Likewise, for $\Delta n_2 = 0$, propagation length at FH (c) and SH (d) are given.

only the maximum achievable propagation length is used while the optimum value of the input phase difference is not shown. Comparing the results of Fig. 5.4.8 with the linear propagation length of FH shown in Figs. 5.4.7(a) and (c), we observe that the length enhancement factor is always larger for smaller values of the thickness of the waveguide despite the fact that propagation lengths are smaller too. This is due to the high mode intensities and thus the higher overlap values obtained at those geometrical configurations. Another noteworthy feature is that while in the case of Fig. 5.4.8(a), δ decreases more or less monotonically with increasing values of thickness, in Fig. 5.4.8(b) it rises again after an initial pattern of decline. On the actual length scale, this results in larger values of the propagation length of the FH seed when pumped with mode of order $m = 2$ as the linear propagation length tends to be larger at higher values of thickness [Fig. 5.4.7(c)]. As a specific example from Fig. 5.4.8(b), for a pump of 35 W input power

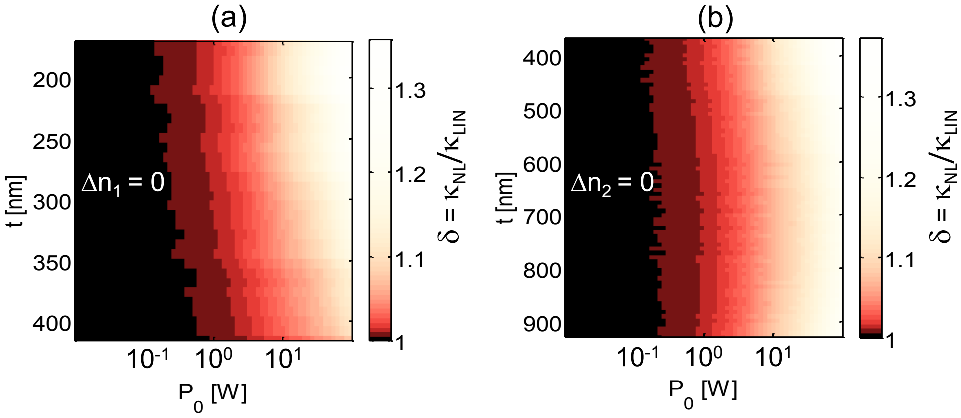

Figure 5.4.8: Ratio of the seed signal's propagation length obtained with a nonlinear pump (κ_{NL}) to the linear propagation (κ_{LIN}) when pumped from the mode of order $m = 1$ (a) and $m = 2$ (b) at SH.

we get δ equal to 1.22 and 1.16 for thickness of 368 nm and 930 nm respectively. This amounts to a differential increase in propagation length with respect to Fig. 5.4.7(c) $[\kappa_0(\nu_0)(\delta - 1)]$ equal to 1.37 μm and 5.92 μm respectively for the same pair of thickness as mentioned before.

5.5 Concluding remarks

To conclude the foregoing discussion, we demonstrated the possibility of modal phase-matching in plasmonic slot waveguides by exploiting geometrical dispersion of the modes. As expected, maximum conversion efficiency between modes of the same order at both FH and SH turned out to be superior because of better mode overlap despite the existence of phase mismatch. However, it was found that this advantage could be traded-off if the distance to observe nonlinear frequency conversion becomes large. In such circumstances, phase-matched interaction by exploiting geometric dispersion of disparate waveguide modes can yield superior results. As for the parametric amplification of a weak seed signal at FH, the results indicate the possibility to achieve moderate length enhancements whereas higher enhancement factors appear to lie beyond the realm of perturbative nonlinear effects.

At the end, we note that results of this chapter have already appeared in our publication found in Ref. [172]

6 Summary and outlook

The purpose of this thesis was to investigate select problems of practical interest that could usefully contribute to the drive towards functional plasmonic devices. In this regard, we began with laying down in Ch. 2 the analytical framework that was to be employed in understanding specific cases that were to follow in the following chapters. The three cases included, namely, the localized resonance of plasmonic particles seen in terms of PSPPs in Ch. 3, enhancing the nonlinear response of cylindrical plasmonic antennas in Ch. 4, and lastly, efficient SHG in plasmonic slot waveguides in Ch. 5. We will now summarize in a flow the essential points of each of them as well as present further research directions possible.

In Ch. 3, we revisited the problem of QS resonance in analytically known plasmonic particles but this time through a semi-analytical view of FP antennas. We hypothesized the existence of a unified explanation for the FP resonances found in extended antennas and LSPP resonances sustained by particles such as spheres when the length of antenna is reduced to zero. Therefore, for FP model to still predict resonances for antennas of negligible length, the reflection phase jump at the terminal mirrors (half particles in our case) had to be π. It turned out to be indeed the case for spheres, core-shell particles, spheroids and cylinders, all of which are analytically well-understood in QS approach. Thereafter, we demonstrated the applicability of FP model on a composite particle made up of hemisphere and semi-spheroid. Since the structure cannot be understood analytically, it was interesting to see if we can still predict the scattering resonance by means of antenna approach. In the end, we suggested factors other than reflection phase jump to be included into a full-fledged analysis so as to explain possible inconsistencies between LSPP resonances in QS theory and antenna approach. The latter presently seem to suggest a larger number of resonances compared to QS approach in the form of multiple π-crossings of the reflection phase jump.

Beyond QS limit, it shall be interesting to see whether and how successfully the idea can be extended to describe particle resonances beyond QS regime. This would probably necessitate investigation of all the modes sustained by the antenna at a given frequency to ascertain whether they too experience a π phase jump at the terminations. And if yes, then how do these resonances compare with their analytical counterparts found in the corresponding Mie theory description.

Another way of furthering this work would be to relate the analytically known dipole response of the respective particles to the modal parameters such as wave number, reflection and absorption coefficients of the guided PSPP mode. If successful, this would be a tremendous step forward as it might potentially lead to a complete description of the scattering properties of asymmetric particles much like their analytically known symmetric counterparts.

Moving over to actual antennas in Ch. 4, we put to use the dispersion of modal reflection coefficient in designing cylindrical antennas with semi-spheroidal caps that can resonate at both FH and SH frequencies involved in a nonlinear process. This was shown to considerably increase the nonlinear coupling coefficient which was defined in a form similar to what is found in another nonlinear interaction model for standing wave resonances before [146]. The prediction of enhanced nonlinear interaction was substantiated later by nonlinear FDTD simulations which demonstrated the superiority of doubly-resonant antennas over those which resonate only at the incident pump frequency as has been the standard practice until recently. At the end, we showed a similar approach works with cylindrical core-shell antennas made up of metallic shells and terminated with semi-spheroidal core-shall caps.

As a future research direction, we would like to see parametric effects investigated in our geometries in which the antennas are illuminated at both FH and SH frequencies. As the energy conversion in this case is sensitive upon the phase difference between the incident radiation at the two harmonics, it might enable interesting switching elements which could be turned on and off by means of a control signal through either FH or SH. Another plausible direction would be to go beyond SHG and consider full breadth of processes possible in quadratic and even cubic nonlinear interactions.

In Ch. 5, at last, we considered the problem of nonlinear SHG in infinitely extending plasmonic waveguides. Similar to Ch. 4, the already high nonlinear conversion efficiency due to high field intensities in sub-wavelength plasmonic waveguides could be further enhanced if the so-called momentum or phase mismatch is compensated between the modes involved in nonlinear conversion process. In this regards, we opted to work with metallic slot waveguides. By manipulating the geometrical parameters of the nonlinear dielectric core, we showed the possibility of finding configurations in which the momentum mismatch disappears for certain combination of modes which are sustained by the waveguides and taking part in degenerate SHG. Since modes of different orders are required in this scheme, we highlighted the fact in our discussion that the utility of employing this method would mostly depend upon the propagation distances at which higher conversion efficiencies are desired. For comparatively smaller propagation distances, we can achieve better conversion efficiency between modes of same order at both FH and SH without compensating phase-mismatch. At last, the existence of phase-matched schemes prompted us to consider the problem of compensating propagation losses which are usually considered to be the most prominent stumbling block in the deployment of plasmonic waveguides in optical devices of practical interest.

A straightforward extension of this work would be to improve the geometrical aspect ratio by suitably engineering the media used for substrate and perhaps even cladding. This would make the whole idea more amenable to implementation in practical schemes where a 1:1 aspect ratio is usually desired between the width and thickness of structures. With this we can further utilize the same method but extended out to include full range of frequencies participating in three- or even four-wave mixing.

The problem of compensating propagation losses also deserve further attention. In a recent study appearing after the publication of results presented in Ch. 5 [172], a polymeric material was used as the nonlinear core in the same geometry as considered here which was able to achieve much larger amplification at significantly lower pump power levels [173]. This provides a more optimistic outlook at the practical utility of the scheme considered here. Therefore, we believe there to be further possibility of exploring available polymeric media which could provide the required degree of loss compensation with minimum requirement on the input pump power.

Zusammenfassung

Ziel dieser Arbeit war es ausgewählte Strukturen von praktischer Relevanz zu untersuchen, die einen entscheidenden Beitrag zu funktionalen, plasmonischen Bauelementen zu leisten in der Lage sind. In diesem Sinne wurde in Kapitel 2 der analytische Rahmen dargelegt, auf dessen Basis die folgenden Kapitel aufgebaut werden sollten. Das Augenmerk wurde im Folgenden auf drei Spezialfälle gerichtet. Als Erstes wurde in Kapitel 3 die lokalisierte Plasmonenresonanz, welche in plasmonischen Partikeln beobachtet werden kann, aus dem Blickwinkel der propagierenden Oberflächenplasmonenpolaritonen betrachtet. In Kapitel 4 wurde als Zweites die Erhöhung der nichtlinearen Antwort zylindrischer, plasmonischer Antennen erörtert. Schließlich wurde in Kapitel 5 die effiziente Erzeugung der zweiten Harmonischen (SHG) in plasmonischen Schlitzhohlleitern behandelt. Im Folgenden werden nun die wichtigsten Punkte dieser Kapitel zusammengefasst.

In Kapitel 3 wurde das Problem der quasistatischen Resonanz in plasmonischen Partikeln aufgegriffen, die eine analytische Beschreibung zulassen. Diesmal hingegen mit dem semi-analytischen Ansatz der Fabry-Pérot (FP) Antenne. Die Existenz einer umfassenden Theorie zur Erklärung sowohl der FP Resonanzen in ausgedehnten Antennen als auch der auftretenden lokalisierten Oberflächenplasmonenpolaritonen-Resonanzen (LSPP) in Partikeln wie Kugeln, wenn die Länge der ausgedehnten Antenne gegen Null strebt, wurde vermutet. Damit der FP Ansatz die Resonanzen in Antennen vernachlässigbarer Länge korrekt beschreibt, muss der Phasensprung an den Endspiegeln, Halbkugeln im hier betrachteten Fall, π betragen. Es stellte sich heraus, dass für Kugeln, Kugel-Schalen-Systeme, Sphäroide und Zylinder, welche allesamt im quasistatischen Ansatz analytisch beschreibbar sind, dies in der Tat der Fall ist. Sodann wurde gezeigt, dass das Anwenden des FP Ansatzes auf Kompositpartikel, welche aus einer Halbkugel und einem Halbsphäroiden bestehen, ebenfalls zu korrekten Resultaten führt. Nebst dem Phasensprung bei der Reflexion wurden weitere Faktoren vorgeschlagen, welche in die Theorie einzufließen haben, um mögliche Unstimmigkeiten in der Form von mehrfachen π-Durchgängen im Reflexionsphasensprung zwischen den LSPP Resonanzen im Quasistatischen und dem Antennenansatz auszuräumen.

Des Weiteren stellt sich die Frage, ob und falls ja, wie erfolgreich die Beschreibung ausgeweitet werden kann, um auch jenseits des quasistatischen Limits Partikelresonanzen korrekt vorauszusagen. Vermutlich wird es die Notwendigkeit nach sich ziehen sämtliche in der Antenne auftretenden Moden bei einer bestimmten Frequenz zu untersuchen, um sicherzustellen, dass diese Moden einen Phasensprung von π an den Enden erleiden. Sollte das der Fall sein, taucht fast unweigerlich die Frage auf, ob diese Partikelresonanzen einen Vergleich zu mit der Mie-Theorie gefundenen analytischen Lösungen erlauben.

In Kapitel 4 wurden alsdann zylindrische Antennen mit semi-sphäroidalen Enden betrachtet. Diese Antennen sollten sowohl bei der an einem nicht linearen Prozess beteiligten Fundamentalfrequenz als auch bei der zweiten harmonischen Frequenz eine Resonanz besitzen. Hierzu wurde die Dispersion des modalen Reflexionskoeffizienten verwendet. Der nicht lineare Kopplungskoeffizient ließ sich damit erheblich steigern. Die Definition dieses nicht linearen Kopplungskoeffizienten wurde dabei in ähnlicher Weise vorgenommen, wie in nicht linearen Wechselwirkungmodellen für Resonanzen stehender Wellen [146]. Die vorhergesagte Steigerung der nicht linearen Wechselwirkung wurde numerisch untermauert unter Verwendung nicht linearer FDTD-Simulationen. Die Simulationen bestätigten die Überlegenheit doppelt resonanter Antennen über jene Antennen, welche ausschließlich bei der Pumpfrequenz eine Resonanz besitzen.

Kapitel 5 behandelte die nicht lineare SHG in unendlich ausgedehnten, plasmonischen Wellenleitern. Genauso wie in Kapitel 4 konnte auch hier die nicht lineare Konversionseffizienz gesteigert werden. Dies allerdings nur unter der Voraussetzung, dass der Impuls- oder Phasenmismatch zwischen den bei der nicht linearen Konversion beteiligten Moden kompensiert werden kann. Im Hinblick darauf fiel die Wahl auf plasmonische Schlitzhohlleiter. Indem die geometrischen Parameter des nicht linearen, dielektrischen Kerns variiert wurden, ließ sich zeigen, dass bei geeigneten Ausdehnungen des Kerns für bestimmte Kombinationen von erlaubten Moden des Wellenleiters, die auch bei der entarteten SHG beteiligt sind, der Impulsmismatch verschwindet. Abschließend wurden phasenangepasste Modelle betrachtet, um Propagationsverluste zu kompensieren. Nach gängiger Meinung stellen diese Propagationsverluste die höchste Hürde dar auf dem Weg zu plasmonischen Wellenleitern in optischen Systemen.

Publications

Publications whose contents are part of this thesis have been highlighted in bold.

Peer-reviewed Journals

1. **S. B. Hasan, R. Filter, A. Ahmed, R. Vogelgesang, R. Gordon, C. Rockstuhl, and F. Lederer. Relating localized nanoparticle resonances to an associated antenna problem. *Phys. Rev. B*, 84:195405, Nov 2011.**

2. A. Hänsel, O. A. Egorov, S. B. Hasan, C. Rockstuhl, and F. Lederer. Optical bistability in a doubly resonant $\chi^{(2)}$-nonlinear plasmonic nanocavity. *Phys. Rev. A*, 85:053843, May 2012.

3. **S. B. Hasan, C. Rockstuhl, T. Pertsch, and F. Lederer. Second-order nonlinear frequency conversion processes in plasmonic slot waveguides. *J. Opt. Soc. Am. B*, 29(7):1606–1611, Jul 2012.**

4. **T. Kaiser, S. B. Hasan, T. Paul, T. Pertsch, and C. Rockstuhl. Impedance generalization for plasmonic waveguides beyond the lumped circuit model. *Phys. Rev. B*, 88:035117, Jul 2013.**

5. R. Alaee, C. Menzel, U. Huebner, E. Pshenay-Severin, S. B. Hasan, T. Pertsch, C. Rockstuhl, and F. Lederer. Deep-Subwavelength Plasmonic Nanoresonators Exploiting Extreme Coupling. *Nano Lett.,* 13(8): 3482–3486, June 2013.

6. S. Mühlig, A. Cunningham, J. Dintinger, M. Farhat, S. B. Hasan, T. Scharf, T. Bürgi, F. Lederer and C. Rockstuhl. A self-assembled three-dimensional cloak in the visible. *Sci. Rep.* 3:2328, July 2013.

7. S. P. Scheeler, S. Mühlig, C. Rockstuhl, S. B. Hasan, S. Ullrich, F. Neubrech , S. Kudera and C. Pacholski. Plasmon Coupling in Self-Assembled Gold Nanoparticle-Based Honeycomb Islands. *J. Phys. Chem. C*, 117(36):18634–18641, Aug 2013.

8. **S. B. Hasan, C. Etrich, R. Filter, C. Rockstuhl, and F. Lederer. Enhancing the nonlinear response of plasmonic nanowire antennas by engineering their terminations. *Phys. Rev. B*, 88:205125, Nov 2013.**

Conference Papers

1. T. Kaiser, C. Helgert, T. Paul, S. B. Hasan, F. Lederer, C. Rockstuhl, and T. Pertsch. Resonant coupling of dielectric waveguides with plasmonic metaatoms. SPIE, Vol. 8093, 809322, (2011).
2. S. B. Hasan, C. Rockstuhl, T. Pertsch, and F. Lederer. Second Order Nonlinear Frequency Conversion Processes In Plasmonic Slot Waveguides. Conference on Lasers and Electro-Optics 2012, OSA Technical Digest (Optical Society of America, 2012), paper QTu1F.6.

Invited Talks

1. C. Rockstuhl, T. Paul, S. B. Hasan, C. Menzel, T. Kaiser, W. Smigaj, T. Pertsch, P. Lalanne and F. Lederer. The impedance of metamaterials and nanoplasmonic structures. Metamaterials, 2011, Barcelona, Spain
2. C. Rockstuhl, R. Alaee, C. Menzel, U. Huebner, E. Pshenay-Severin, S. B. Hasan, T. Pertsch and F. Lederer. Exploiting extreme coupling in nanoplasmonic elements, NOMA 2013, Cetraro, Italy
3. C. Rockstuhl, S. Mühlig, M. Farhat, S. B. Hasan, A. Cunningham, T. Bürgi, J. Dintinger, T. Scharf, and F. Lederer. A cloak from self-assembled metallic nanoparticles, META 2013, Sharjah, United Arab Emirates.

Conference Contributions

1. S. B. Hasan, C. Etrich, R. Filter, C. Rockstuhl, F. Lederer. Tailoring the quadratic response of nanoantennas: use of a waveguide model, OWTNM 2013, Twente, The Netherlands
2. S. B. Hasan, C. Rockstuhl, C. Etrich, and F. Lederer. Enhancing the quadratic response of plasmonic nanowire antennas. Nanometa 2013, Seefeld, Austria

3. T. Kaiser, S. B. Hasan, T. Paul, T. Pertsch and C. Rockstuhl. The impedance concept in plasmonic waveguides. 17th International Workshop on Microchip Plasmonics 2012, Erlangen, Germany
4. S. B. Hasan, C. Rockstuhl, T. Pertsch, and F. Lederer. Second order nonlinear frequency conversion processes in plasmonic slot waveguides. CLEO/QELS 2012 San Jose, California, USA
5. T. Kaiser, S. B. Hasan, T. Paul, T. Pertsch, C. Rockstuhl. The relative impedance of waveguiding structures. META 2012 Paris, France
6. T. Kaiser, C. Helgert, T. Paul, S. B. Hasan, F. Lederer, C. Rockstuhl, and T. Pertsch. Resonant coupling of dielectric waveguides with plasmonic metaatoms. SPIE Optics + Photonics 2011, San Diego, USA
7. S. B. Hasan, J. Reinhold, T. Paul, C. Helgert, A. Chipouline, C. Rockstuhl, T. Pertsch. Intrinsic and Extrinsic Nonlinearities of Nanooptical Systems. UNO 2 2010, Bad Dürkheim, Germany
8. T. Paul, S. B. Hasan, C. Rockstuhl and F. Lederer. Enhanced second and third harmonic generation using plasmonic metamaterials, PhoNa International Workshop 2010, Jena, Germany
9. T. Paul, C. Menzel, C. Rockstuhl, S. B. Hasan, and F. Lederer. Enhancing higher harmonics generation using plasmonic nanostructures, 74. Annual Meeting of the Deutsche Physikalische Gesellschaft 2010, Regensburg, GermanyEhrenwortliche Erklarung

Bibliography

[1] H. Raether. *Surface Plasmons on Smooth and Rough Surfaces and on Gratings.* Springer Tracts in Modern Physics. Springer, 1988.

[2] S. A. Maier. *Plasmonics: Fundamentals and Applications.* Springer, 2007.

[3] M. Born and E. Wolf. *Principles of Optics: Electromagnetic Theory of Propagation, Interference and Diffraction of Light.* Cambridge University Press, 7th edition, 1999.

[4] W. L. Barnes, A. Dereux, and T. W. Ebbesen. Surface plasmon subwavelength optics. *Nature*, 424(6950):824–830, Aug. 2003.

[5] D. K. Gramotnev and S. I. Bozhevolnyi. Plasmonics beyond the diffraction limit. *Nat Photon*, 4(2):83–91, Feb. 2010.

[6] J. A. Schuller, E. S. Barnard, W. Cai, Y. C. Jun, J. S. White, and M. L. Brongersma. Plasmonics for extreme light concentration and manipulation. *Nat Mater*, 9(3):193–204, Mar. 2010.

[7] G. Mie. Beiträge zur optik trüber medien, speziell kolloidaler metallösungen. *Annalen der Physik*, 330(3):377–445, 1908.

[8] D. R. H. Craig F. Bohren. *Absorption and Scattering of Light by Small Particles.* Wiley-VCH, 1998.

[9] L. Novotny and N. van Hulst. Antennas for light. *Nat Photon*, 5(2):83–90, Feb. 2011.

[10] S. Palomba, H. Harutyunyan, J. Renger, R. Quidant, N. F. van Hulst, and L. Novotny. Nonlinear plasmonics at planar metal surfaces. *Philosophical Transactions of the Royal Society A: Mathematical,Physical and Engineering Sciences*, 369(1950):3497–3509, 2011.

[11] M. Kauranen and A. V. Zayats. Nonlinear plasmonics. *Nat Photon*, 6(11):737–748, Nov. 2012.

[12] C. Pai-Yen, A. Christos, and A. Andrea. Enhanced nonlinearities using plasmonic nanoantennas, 2012.

[13] D. F. P. Pile and D. K. Gramotnev. Channel plasmon-polariton in atriangular groove on a metal surface. *Opt. Lett.*, 29(10):1069–1071, May 2004.

[14] S. I. Bozhevolnyi, V. S. Volkov, E. Devaux, and T. W. Ebbesen. Channel plasmon-polariton guiding by subwavelength metal grooves. *Phys. Rev. Lett.*, 95:046802, Jul 2005.

[15] S. I. Bozhevolnyi. Effective-index modeling of channel plasmon polaritons. *Opt. Express*, 14(20):9467–9476, Oct 2006.

[16] I. min Lee, J. Jung, J. Park, H. Kim, and B. Lee. Dispersion characteristics of channel plasmon polariton waveguides with step-trench-type grooves. *Opt. Express*, 15(25):16596–16603, Dec 2007.

[17] R. F. Oulton, V. J. Sorger, D. A. Genov, D. F. P. Pile, and X. Zhang. A hybrid plasmonic waveguide for subwavelength confinement and long-range propagation. *Nat Photon*, 2(8):496–500, Aug. 2008.

[18] T. Holmgaard, J. Gosciniak, and S. I. Bozhevolnyi. Long-range dielectric-loaded surface plasmon-polariton waveguides. *Opt. Express*, 18(22):23009–23015, Oct 2010.

[19] D. Sarid. Long-range surface-plasma waves on very thin metal films. *Phys. Rev. Lett.*, 47:1927–1930, Dec 1981.

[20] G. I. Stegeman, J. J. Burke, and D. G. Hall. Nonlinear optics of long range surface plasmons. *Appl. Phys. Lett.*, 41(10):906–908, 1982.

[21] J. C. Quail, J. G. Rako, H. J. Simon, and R. T. Deck. Optical second-harmonic generation with long-range surface plasmons. *Phys. Rev. Lett.*, 50:1987–1989, Jun 1983.

[22] J. J. Burke, G. I. Stegeman, and T. Tamir. Surface-polariton-like waves guided by thin, lossy metal films. *Phys. Rev. B*, 33:5186–5201, Apr 1986.

[23] R. Charbonneau, P. Berini, E. Berolo, and E. Lisicka-Shrzek. Experimental observation of plasmon polariton waves supported by a thin metal film of finite width. *Opt. Lett.*, 25(11):844–846, Jun 2000.

[24] J.-C. Weeber, Y. Lacroute, and A. Dereux. Optical near-field distributions of surface plasmon waveguide modes. *Phys. Rev. B*, 68:115401, Sep 2003.

[25] J. A. Dionne, L. A. Sweatlock, H. A. Atwater, and A. Polman. Plasmon slot waveguides: Towards chip-scale propagation with subwavelength-scale localization. *Phys. Rev. B*, 73:035407, Jan 2006.

[26] L. Liu, Z. Han, and S. He. Novel surface plasmon waveguide for high integration. *Opt. Express*, 13(17):6645–6650, Aug 2005.

[27] E. Feigenbaum and M. Orenstein. Nano plasmon polariton modes of a wedge cross section metal waveguide. *Opt. Express*, 14(19):8779–8784, Sep 2006.

[28] Y. Kou, F. Ye, and X. Chen. Low-loss hybrid plasmonic waveguide for compact and high-efficient photonic integration. *Opt. Express*, 19(12):11746–11752, Jun 2011.

[29] S. Belan, S. Vergeles, and P. Vorobev. Adjustable subwavelength localization in a hybrid plasmonic waveguide. *Opt. Express*, 21(6):7427–7438, Mar 2013.

[30] Y. Bian, Z. Zheng, X. Zhao, L. Liu, Y. Su, J. Liu, J. Zhu, and T. Zhou. Nanoscale light guiding in a silicon-based hybrid plasmonic waveguide that incorporates an inverse metal ridge. *physica status solidi (a)*, 210(7):1424–1428, 2013.

[31] H. Ditlbacher, N. Galler, D. M. Koller, A. Hohenau, A. Leitner, F. R. Aussenegg, and J. R. Krenn. Coupling dielectric waveguide modes to surface plasmon polaritons. *Opt. Express*, 16(14):10455–10464, Jul 2008.

[32] E. Verhagen, M. Spasenović, A. Polman, and L. K. Kuipers. Nanowire plasmon excitation by adiabatic mode transformation. *Phys. Rev. Lett.*, 102:203904, May 2009.

[33] J. Wen, S. Romanov, and U. Peschel. Excitation of plasmonic gap waveguides by nanoantennas. *Opt. Express*, 17(8):5925–5932, Apr 2009.

[34] Z. Fang, L. Fan, C. Lin, D. Zhang, A. J. Meixner, and X. Zhu. Plasmonic coupling of bow tie antennas with ag nanowire. *Nano Lett.*, 11(4):1676–1680, 2011.

[35] H. Noh, Y. Chong, A. D. Stone, and H. Cao. Perfect coupling of light to surface plasmons by coherent absorption. *Phys. Rev. Lett.*, 108:186805, May 2012.

[36] A. Kriesch, S. P. Burgos, D. Ploss, H. Pfeifer, H. A. Atwater, and U. Peschel. Functional plasmonic nanocircuits with low insertion and propagation losses. *Nano Lett.*, 13(9):4539–4545, 2013.

[37] F. Obelleiro, J. M. Taboada, D. M. Solís, and L. Bote. Directive antenna nanocoupler to plasmonic gap waveguides. *Opt. Lett.*, 38(10):1630–1632, May 2013.

[38] Q. Li, Y. Song, Y. Chen, M. Yan, and M. Qiu. Efficient directional coupler based on plasmonic waveguide for photonic integrated circuits. In *Optical Communications and Networks (ICOCN 2010), 9th International Conference on*, pages 366–368, 2010.

[39] D. Gramotnev, K. Vernon, and D. Pile. Directional coupler using gap plasmon waveguides. *Appl. Phys. B*, 93(1):99–106, 2008.

[40] Y. Song, J. Wang, M. Yan, and M. Qiu. Efficient coupling between dielectric and hybrid plasmonic waveguides by multimode interference power splitter. *J. Opt.*, 13(7):075002, 2011.

[41] V. A. Zenin, Z. Han, V. S. Volkov, K. Leosson, I. P. Radko, and S. I. Bozhevolnyi. Directional coupling in long-range dielectric-loaded plasmonic waveguides. *Opt. Express*, 21(7):8799–8807, Apr 2013.

[42] M. I. Stockman. Nanofocusing of optical energy in tapered plasmonic waveguides. *Phys. Rev. Lett.*, 93:137404, Sep 2004.

[43] E. Verhagen, A. Polman, and L. K. Kuipers. Nanofocusing in laterally tapered plasmonic waveguides. *Opt. Express*, 16(1):45–57, Jan 2008.

[44] V. S. Volkov, S. I. Bozhevolnyi, S. G. Rodrigo, L. Martín-Moreno, F. J. García-Vidal, E. Devaux, and T. W. Ebbesen. Nanofocusing with channel plasmon polaritons. *Nano Lett.*, 9(3):1278–1282, 2009.

[45] X. He, L. Yang, and T. Yang. Optical nanofocusing by tapering coupled photonic-plasmonic waveguides. *Opt. Express*, 19(14):12865–12872, Jul 2011.

[46] H. Choo, M.-K. Kim, M. Staffaroni, T. J. Seok, J. Bokor, S. Cabrini, P. J. Schuck, M. C. Wu, and E. Yablonovitch. Nanofocusing in a metal-insulator-metal gap plasmon waveguide with a three-dimensional linear taper. *Nat Photon*, 6(12):838–844, Dec. 2012.

[47] H. Shin and S. Fan. All-angle negative refraction for surface plasmon waves using a metal-dielectric-metal structure. *Phys. Rev. Lett.*, 96:073907, Feb 2006.

[48] H. J. Lezec, J. A. Dionne, and H. A. Atwater. Negative refraction at visible frequencies. *Science*, 316(5823):430–432, 2007.

[49] J. A. Dionne, E. Verhagen, A. Polman, and H. A. Atwater. Are negative index materials achievable with surface plasmon waveguides? a case study of three plasmonic geometries. *Opt. Express*, 16(23):19001–19017, Nov 2008.

[50] E. Feigenbaum, N. Kaminski, and M. Orenstein. Negative dispersion: a backward wave or fast light? nanoplasmonic examples. *Opt. Express*, 17(21):18934–18939, Oct 2009.

[51] R. de Waele, S. P. Burgos, H. A. Atwater, and A. Polman. Negative refractive index in coaxial plasmon waveguides. *Opt. Express*, 18(12):12770–12778, Jun 2010.

[52] P. Nordlander, C. Oubre, E. Prodan, K. Li, and M. I. Stockman. Plasmon hybridization in nanoparticle dimers. *Nano Lett.*, 4(5):899–903, 2004.

[53] S.-C. Yang, H. Kobori, C.-L. He, M.-H. Lin, H.-Y. Chen, C. Li, M. Kanehara, T. Teranishi, and S. Gwo. Plasmon hybridization in individual gold nanocrystal dimers: Direct observation of bright and dark modes. *Nano Lett.*, 10(2):632–637, 2010. PMID: 20058898.

[54] D. W. Brandl, N. A. Mirin, and P. Nordlander. Plasmon modes of nanosphere trimers and quadrumers. *J. Phys. Chem. B*, 110(25):12302–12310, 2006. PMID: 16800552.

[55] T. Shegai, Z. Li, T. Dadosh, Z. Zhang, H. Xu, and G. Haran. Managing light polarization via plasmon-molecule interactions within an asymmetric metal nanoparticle trimer. *Proc. Natl. Acad. Sci. USA*, 105(43):16448–16453, 2008.

[56] H. Wang, D. W. Brandl, P. Nordlander, and N. J. Halas. Plasmonic nanostructures: Artificial molecules. *Acc. Chem. Res.*, 40(1):53–62, 2007. PMID: 17226945.

[57] J. A. Fan, C. Wu, K. Bao, J. Bao, R. Bardhan, N. J. Halas, V. N. Manoharan, P. Nordlander, G. Shvets, and F. Capasso. Self-assembled plasmonic nanoparticle clusters. *Science*, 328(5982):1135–1138, 2010.

[58] P. Mühlschlegel, H.-J. Eisler, O. J. F. Martin, B. Hecht, and D. W. Pohl. Resonant optical antennas. *Science*, 308(5728):1607–1609, 2005.

[59] L. Novotny. Effective wavelength scaling for optical antennas. *Phys. Rev. Lett.*, 98:266802, Jun 2007.

[60] J. Dorfmüller, R. Vogelgesang, W. Khunsin, C. Rockstuhl, C. Etrich, and

K. Kern. Plasmonic nanowire antennas: Experiment, simulation, and theory. *Nano Lett.*, 10(9):3596–3603, 2010.

[61] D. M. Pozar. *Microwave Engineering.* Wile, 2011.

[62] T. W. Ebbesen, H. J. Lezec, H. F. Ghaemi, T. Thio, and P. A. Wolff. Extraordinary optical transmission through sub-wavelength hole arrays. *Nature*, 391(6668):667–669, Feb. 1998.

[63] L. Martín-Moreno, F. J. Garc'iia-Vidal, H. J. Lezec, K. M. Pellerin, T. Thio, J. B. Pendry, and T. W. Ebbesen. Theory of extraordinary optical transmission through subwavelength hole arrays. *Phys. Rev. Lett.*, 86:1114–1117, Feb 2001.

[64] H. Liu and P. Lalanne. Microscopic theory of the extraordinary optical transmission. *Nature*, 452(7188):728–731, Apr. 2008.

[65] R. Gordon, D. Sinton, K. L. Kavanagh, and A. G. Brolo. A new generation of sensors based on extraordinary optical transmission. *Acc. Chem. Res.*, 41(8):1049–1057, 2008.

[66] J. Pendry, A. J. Holden, D. J. Robbins, and W. J. Stewart. Magnetism from conductors and enhanced nonlinear phenomena. *IEEE Transactions on Microwave Theory and Techniques*, 47(11):2075–2084, 1999.

[67] S. Linden, C. Enkrich, M. Wegener, J. Zhou, T. Koschny, and C. M. Soukoulis. Magnetic response of metamaterials at 100 terahertz. *Science*, 306(5700):1351–1353, 2004.

[68] G. Dolling, C. Enkrich, M. Wegener, J. F. Zhou, C. M. Soukoulis, and S. Linden. Cut-wire pairs and plate pairs as magnetic atoms for optical metamaterials. *Opt. Lett.*, 30(23):3198–3200, Dec 2005.

[69] N. Katsarakis, G. Konstantinidis, A. Kostopoulos, R. S. Penciu, T. F. Gundogdu, M. Kafesaki, E. N. Economou, T. Koschny, and C. M. Soukoulis. Magnetic response of split-ring resonators in the far-infrared frequency regime. *Opt. Lett.*, 30(11):1348–1350, Jun 2005.

[70] C. Rockstuhl, F. Lederer, C. Etrich, T. Zentgraf, J. Kuhl, and H. Giessen. On the reinterpretation of resonances in split-ring-resonators at normal incidence. *Opt. Express*, 14(19):8827–8836, Sep 2006.

[71] E. Plum, J. Zhou, J. Dong, V. A. Fedotov, T. Koschny, C. M. Soukoulis, and

N. I. Zheludev. Metamaterial with negative index due to chirality. *Phys. Rev. B*, 79:035407, Jan 2009.

[72] A. S. Schwanecke, V. A. Fedotov, V. V. Khardikov, S. L. Prosvirnin, Y. Chen, and N. I. Zheludev. Nanostructured metal film with asymmetric optical transmission. *Nano Lett.*, 8(9):2940–2943, 2008. PMID: 18720979.

[73] E. Plum, X.-X. Liu, V. A. Fedotov, Y. Chen, D. P. Tsai, and N. I. Zheludev. Metamaterials: Optical activity without chirality. *Phys. Rev. Lett.*, 102:113902, Mar 2009.

[74] C. Menzel, C. Helgert, C. Rockstuhl, E.-B. Kley, A. Tünnermann, T. Pertsch, and F. Lederer. Asymmetric transmission of linearly polarized light at optical metamaterials. *Phys. Rev. Lett.*, 104:253902, Jun 2010.

[75] M. Kang, J. Chen, H.-X. Cui, Y. Li, and H.-T. Wang. Asymmetric transmission for linearly polarized electromagnetic radiation. *Opt. Express*, 19(9):8347–8356, Apr 2011.

[76] S. Zhang, D. A. Genov, Y. Wang, M. Liu, and X. Zhang. Plasmon-induced transparency in metamaterials. *Phys. Rev. Lett.*, 101:047401, Jul 2008.

[77] N. Liu, L. Langguth, T. Weiss, J. Kastel, M. Fleischhauer, T. Pfau, and H. Giessen. Plasmonic analogue of electromagnetically induced transparency at the drude damping limit. *Nat Mater*, 8(9):758–762, Sept. 2009.

[78] R. D. Kekatpure, E. S. Barnard, W. Cai, and M. L. Brongersma. Phase-coupled plasmon-induced transparency. *Phys. Rev. Lett.*, 104:243902, Jun 2010.

[79] Z. Han and S. I. Bozhevolnyi. Plasmon-induced transparency with detuned ultracompact fabry-perot resonators in integrated plasmonic devices. *Opt. Express*, 19(4):3251–3257, Feb 2011.

[80] C. Hu, Z. Zhao, X. Chen, and X. Luo. Realizing near-perfect absorption at visible frequencies. *Opt. Express*, 17(13):11039–11044, Jun 2009.

[81] Y. Avitzour, Y. A. Urzhumov, and G. Shvets. Wide-angle infrared absorber based on a negative-index plasmonic metamaterial. *Phys. Rev. B*, 79:045131, Jan 2009.

[82] J. Hao, J. Wang, X. Liu, W. J. Padilla, L. Zhou, and M. Qiu. High performance optical absorber based on a plasmonic metamaterial. *Appl. Phys. Lett.*, 96(25):–, 2010.

[83] K. Thyagarajan, S. Rivier, A. Lovera, and O. J. Martin. Enhanced second-harmonic generation from double resonant plasmonic antennae. *Opt. Express*, 20(12):12860–12865, Jun 2012.

[84] A. Hänsel, O. A. Egorov, S. B. Hasan, C. Rockstuhl, and F. Lederer. Optical bistability in a doubly resonant $\chi^{(2)}$-nonlinear plasmonic nanocavity. *Phys. Rev. A*, 85:053843, May 2012.

[85] U. K. Chettiar and N. Engheta. Optical frequency mixing through nanoantenna enhanced difference frequency generation: Metatronic mixer. *Phys. Rev. B*, 86:075405, Aug 2012.

[86] H. Aouani, M. Navarro-Cia, M. Rahmani, T. P. H. Sidiropoulos, M. Hong, R. F. Oulton, and S. A. Maier. Multiresonant broadband optical antennas as efficient tunable nanosources of second harmonic light. *Nano Lett.*, 12(9):4997–5002, 2012.

[87] R. W. Boyd. *Nonlinear Optics*. Academic Press, 3rd edition, 2008.

[88] J. D. Jackson. *Classical Electrodynamics*. Wiley, 3rd edition, 1998.

[89] A. S. W. Alan V. Oppenheim and S. Hamid. *Signals and Systems*. Prentice Hall, 1996.

[90] R. J. Potton. Reciprocity in optics. *Rep. Prog. Phys.*, 67(5):717, 2004.

[91] A. W. Snyder and J. Love. *Optical Waveguide Theory*. Springer, 1984.

[92] J. Petschulat, A. Chipouline, A. Tünnermann, T. Pertsch, C. Menzel, C. Rockstuhl, T. Paul, and F. Lederer. Simple and versatile analytical approach for planar metamaterials. *Phys. Rev. B*, 82:075102, Aug 2010.

[93] G. Lecamp, J. P. Hugonin, and P. Lalanne. Theoretical and computational concepts for periodic optical waveguides. *Opt. Express*, 15(18):11042–11060, Sep 2007.

[94] T. Paul, C. Menzel, W. Śmigaj, C. Rockstuhl, P. Lalanne, and F. Lederer. Reflection and transmission of light at periodic layered metamaterial films. *Phys. Rev. B*, 84:115142, Sep 2011.

[95] S. Boscolo, C. Conti, M. Midrio, and C. Someda. Numerical analysis of propagation and impedance matching in 2d photonic crystal waveguides with finite length. *IEEE/OSA Journal of Lightwave Technology*, 20(2):304–310, 2002.

[96] R. Biswas, Z. Y. Li, and K. M. Ho. Impedance of photonic crystals and photonic crystal waveguides. *Appl. Phys. Lett.*, 84(8):1254–1256, 2004.

[97] B. Momeni, A. A. Eftekhar, and A. Adibi. Effective impedance model for analysis of reflection at the interfaces of photonic crystals. *Opt. Lett.*, 32(7):778–780, Apr 2007.

[98] Z. Lu and D. W. Prather. Calculation of effective permittivity, permeability, and surface impedance of negative-refraction photonic crystals. *Opt. Express*, 15(13):8340–8345, Jun 2007.

[99] W. Śmigaj and B. Gralak. Validity of the effective-medium approximation of photonic crystals. *Phys. Rev. B*, 77:235445, Jun 2008.

[100] T. Kaiser, S. B. Hasan, T. Paul, T. Pertsch, and C. Rockstuhl. Impedance generalization for plasmonic waveguides beyond the lumped circuit model. *Phys. Rev. B*, 88:035117, Jul 2013.

[101] R. Iliew, C. Etrich, T. Pertsch, F. Lederer, and Y. S. Kivshar. Huge enhancement of backward second-harmonic generation with slow light in photonic crystals. *Phys. Rev. A*, 81:023820, Feb 2010.

[102] N. Bloembergen. Conservation laws in nonlinear optics. *J. Opt. Soc. Am.*, 70(12):1429–1436, Dec 1980.

[103] J. A. Armstrong, N. Bloembergen, J. Ducuing, and P. S. Pershan. Interactions between light waves in a nonlinear dielectric. *Phys. Rev.*, 127:1918–1939, Sep 1962.

[104] B. E. A. Saleh and M. C. Teich. *Fundamentals of Photonics.* Wiley Series in Pure and Applied Optics. Wiley-Interscience, 2nd edition, 2007.

[105] P. B. Johnson and R. W. Christy. Optical constants of the noble metals. *Phys. Rev. B*, 6:4370–4379, Dec 1972.

[106] D. J. Griffiths. *Introduction to Electrodynamics.* Addison-Wesley, 4th edition, 2012.

[107] F. Wang and Y. R. Shen. General Properties of Local Plasmons in Metal Nanostructures. *Phys. Rev. Lett.*, 97(20):206806, Nov. 2006.

[108] E. Feigenbaum and M. Orenstein. Ultrasmall volume plasmons, yet with complete retardation effects. *Phys. Rev. Lett.*, 101:163902, Oct 2008.

[109] J. Dorfmüller, R. Vogelgesang, R. T. Weitz, C. Rockstuhl, C. Etrich, T. Pertsch, F. Lederer, and K. Kern. Fabry-pérot resonances in one-dimensional plasmonic nanostructures. *Nano Lett.*, 9(6):2372–2377, 2009. PMID: 19472987.

[110] A. Sommerfeld. Üeber die fortpflanzung elektrodynamischer wellenlängen eines drahtes. *Annalen der Physik*, 303(2):233–290, 1899.

[111] K. Wang and D. M. Mittleman. Metal wires for terahertz wave guiding. *Nature*, 432(7015):376–379, Nov. 2004.

[112] M. Wächter, M. Nagel, and H. Kurz. Frequency-dependent characterization of thz sommerfeld wave propagation on single-wires. *Opt. Express*, 13(26):10815–10822, Dec 2005.

[113] H. Wang, D. W. Brandl, F. Le, P. Nordlander, and N. J. Halas. Nanorice: A hybrid plasmonic nanostructure. *Nano Lett.*, 6(4):827–832, 2006. PMID: 16608292.

[114] D. E. Chang, A. S. Sørensen, P. R. Hemmer, and M. D. Lukin. Strong coupling of single emitters to surface plasmons. *Phys. Rev. B*, 76:035420, Jul 2007.

[115] R. Gordon. Reflection of cylindrical surface waves. *Opt. Express*, 17(21):18621–18629, Oct 2009.

[116] S. Oldenburg, R. Averitt, S. Westcott, and N. Halas. Nanoengineering of optical resonances. *Chem. Phys. Lett.*, 288(2-4):243 – 247, 1998.

[117] E. Prodan, C. Radloff, N. J. Halas, and P. Nordlander. A hybridization model for the plasmon response of complex nanostructures. *Science*, 302(5644):419–422, 2003.

[118] S. J. Al-Bader and M. Imtaar. Optical fiber hybrid-surface plasmon polaritons. *J. Opt. Soc. Am. B*, 10(1):83–88, Jan 1993.

[119] H. Wei, A. Reyes-Coronado, P. Nordlander, J. Aizpurua, and H. Xu. Multipolar plasmon resonances in individual ag nanorice. *ACS Nano*, 4(5):2649–2654, 2010. PMID: 20397629.

[120] S. B. Hasan, R. Filter, A. Ahmed, R. Vogelgesang, R. Gordon, C. Rockstuhl, and F. Lederer. Relating localized nanoparticle resonances to an associated antenna problem. *Phys. Rev. B*, 84:195405, Nov 2011.

[121] J. Yang, C. Sauvan, A. Jouanin, S. Collin, J.-L. Pelouard, and P. Lalanne. Ultrasmall metal-insulator-metal nanoresonators: impact of slow-wave effects on the quality factor. *Opt. Express*, 20(15):16880–16891, Jul 2012.

[122] T. Kosako, Y. Kadoya, and H. F. Hofmann. Directional control of light by a nano-optical yagi-uda antenna. *Nat Photon*, 4(5):312–315, May 2010.

[123] N. Liu, M. L. Tang, M. Hentschel, H. Giessen, and A. P. Alivisatos. Nanoantenna-enhanced gas sensing in a single tailored nanofocus. *Nat Mater*, 10(8):631–636, Aug. 2011.

[124] T. T. H., S. F. D., S. F. B., and van Hulst N. F. Optical antennas direct single-molecule emission. *Nat Photon*, 2(4):234–237, Apr. 2008.

[125] J. I. Dadap, J. Shan, and T. F. Heinz. Theory of optical second-harmonic generation from a sphere of centrosymmetric material: small-particle limit. *J. Opt. Soc. Am. B*, 21(7):1328–1347, Jul 2004.

[126] J. Rudnick and E. A. Stern. Second-harmonic radiation from metal surfaces. *Phys. Rev. B*, 4:4274–4290, Dec 1971.

[127] J. E. Sipe, V. C. Y. So, M. Fukui, and G. I. Stegeman. Analysis of second-harmonic generation at metal surfaces. *Phys. Rev. B*, 21:4389–4402, May 1980.

[128] H. J. Simon, D. E. Mitchell, and J. G. Watson. Optical second-harmonic generation with surface plasmons in silver films. *Phys. Rev. Lett.*, 33:1531–1534, Dec 1974.

[129] M. W. Klein, C. Enkrich, M. Wegener, and S. Linden. Second-harmonic generation from magnetic metamaterials. *Science*, 313(5786):502–504, 2006.

[130] B. K. Canfield, H. Husu, J. Laukkanen, B. Bai, M. Kuittinen, J. Turunen, and M. Kauranen. Local field asymmetry drives second-harmonic generation in noncentrosymmetric nanodimers. *Nano Lett.*, 7(5):1251–1255, 2007.

[131] S. Linden, F. B. P. Niesler, J. Förstner, Y. Grynko, T. Meier, and M. Wegener. Collective effects in second-harmonic generation from split-ring-resonator arrays. *Phys. Rev. Lett.*, 109:015502, Jul 2012.

[132] C. Cirací, E. Poutrina, M. Scalora, and D. R. Smith. Origin of second-harmonic generation enhancement in optical split-ring resonators. *Phys. Rev. B*, 85:201403, May 2012.

[133] H. Husu, R. Siikanen, J. Mäkitalo, J. Lehtolahti, J. Laukkanen, M. Kuittinen, and M. Kauranen. Metamaterials with tailored nonlinear optical response. *Nano Lett.*, 12(2):673–677, 2012.

[134] T. Utikal, T. Zentgraf, T. Paul, C. Rockstuhl, F. Lederer, M. Lippitz, and H. Giessen. Towards the origin of the nonlinear response in hybrid plasmonic systems. *Phys. Rev. Lett.*, 106:133901, Mar 2011.

[135] J. Reinhold, M. R. Shcherbakov, A. Chipouline, V. I. Panov, C. Helgert, T. Paul, C. Rockstuhl, F. Lederer, E.-B. Kley, A. Tünnermann, A. A. Fedyanin, and T. Pertsch. Contribution of the magnetic resonance to the third harmonic generation from a fishnet metamaterial. *Phys. Rev. B*, 86:115401, Sep 2012.

[136] M. Hentschel, T. Utikal, H. Giessen, and M. Lippitz. Quantitative modeling of the third harmonic emission spectrum of plasmonic nanoantennas. *Nano Lett.*, 12(7):3778–3782, 2012.

[137] A. Slablab, L. L. Xuan, M. Zielinski, Y. de Wilde, V. Jacques, D. Chauvat, and J.-F. Roch. Second-harmonic generation from coupled plasmon modes in a single dimer of gold nanospheres. *Opt. Express*, 20(1):220–227, Jan 2012.

[138] J. Butet, I. Russier-Antoine, C. Jonin, N. Lascoux, E. Benichou, and P.-F. Brevet. Nonlinear mie theory for the second harmonic generation in metallic nanoshells. *J. Opt. Soc. Am. B*, 29(8):2213–2221, Aug 2012.

[139] C. Cirací, E. Poutrina, M. Scalora, and D. R. Smith. Second-harmonic generation in metallic nanoparticles: Clarification of the role of the surface. *Phys. Rev. B*, 86:115451, Sep 2012.

[140] P. Ginzburg, A. Krasavin, Y. Sonnefraud, A. Murphy, R. J. Pollard, S. A. Maier, and A. V. Zayats. Nonlinearly coupled localized plasmon resonances: Resonant second-harmonic generation. *Phys. Rev. B*, 86:085422, Aug 2012.

[141] P.-Y. Chen and A. Alú. Subwavelength imaging using phase-conjugating nonlinear nanoantenna arrays. *Nano Lett.*, 11(12):5514–5518, 2011.

[142] C. Argyropoulos, P.-Y. Chen, G. D'Aguanno, N. Engheta, and A. Alú. Boosting optical nonlinearities in ϵ-near-zero plasmonic channels. *Phys. Rev. B*, 85:045129, Jan 2012.

[143] H. Ditlbacher, A. Hohenau, D. Wagner, U. Kreibig, M. Rogers, F. Hofer,

F. R. Aussenegg, and J. R. Krenn. Silver nanowires as surface plasmon resonators. *Phys. Rev. Lett.*, 95:257403, Dec 2005.

[144] `http://www.lambdaphoto.co.uk/pdfs/Inrad_datasheet_LNB.pdf`.

[145] C. Hafner and J. Smajic. Eigenvalue analysis of lossy dispersive waveguides. *J. Mod. Opt.*, 58(5-6):467–479, 2011.

[146] A. Rodriguez, M. Soljacic, J. D. Joannopoulos, and S. G. Johnson. $\chi^{(2)}$ and $\chi^{(3)}$ harmonic generation at a critical power in inhomogeneous doublyresonant cavities. *Opt. Express*, 15(12):7303–7318, Jun 2007.

[147] A. Taflove and S. C. Hagness. *Computational Electrodynamics: The Finite-Difference Time-Domain Method.* Artech House, 3rd edition, 2005.

[148] J. Richter, A. Steinbrück, T. Pertsch, A. TÃŒnnermann, and R. Grange. Plasmonic core - shell nanowires for enhanced second-harmonic generation. *Plasmonics*, 8(1):115–120, 2013.

[149] S. B. Hasan, C. Etrich, R. Filter, C. Rockstuhl, and F. Lederer. Enhancing the nonlinear response of plasmonic nanowire antennas by engineering their terminations. *Phys. Rev. B*, 88:205125, Nov 2013.

[150] P. Mühlschlegel, H.-J. Eisler, O. J. F. Martin, B. Hecht, and D. W. Pohl. Resonant optical antennas. *Science*, 308(5728):1607–1609, June 2005.

[151] S. Kim, J. Jin, Y.-J. Kim, I.-Y. Park, Y. Kim, and S.-W. Kim. High-harmonic generation by resonant plasmon field enhancement. *Nature*, 453(7196):757–760, June 2008.

[152] N. Talebi, M. Shahabadi, W. Khunsin, and R. Vogelgesang. Plasmonic grating as a nonlinear converter-coupler. *Opt. Express*, 20(2):1392–1405, Jan 2012.

[153] W. Fan, S. Zhang, K. J. Malloy, S. R. J. Brueck, N. C. Panoiu, and R. M. Osgood. Second harmonic generation from patterned gaas inside a subwavelength metallic hole array. *Opt. Express*, 14(21):9570–9575, Oct 2006.

[154] H. Y. Lin and Y. F. Chen. Giant enhancement of luminescence induced by second-harmonic surface plasmon resonance. *Appl. Phys. Lett.*, 88(10):–, 2006.

[155] K. Chen, C. Durak, J. R. Heflin, and H. D. Robinson. Plasmon-enhanced

second-harmonic generation from ionic self-assembled multilayer films. *Nano Lett.*, 7(2):254–258, 2007.

[156] N. J. Borys, M. J. Walter, and J. M. Lupton. Intermittency in second-harmonic radiation from plasmonic hot spots on rough silver films. *Phys. Rev. B*, 80(16):161407, Oct 2009.

[157] T. Schumacher, K. Kratzer, D. Molnar, M. Hentschel, H. Giessen, and M. Lippitz. Nanoantenna-enhanced ultrafast nonlinear spectroscopy of a single gold nanoparticle. *Nat Commun*, 2:333–, May 2011.

[158] J. Mäkitalo, S. Suuriniemi, and M. Kauranen. Boundary element method for surface nonlinear optics of nanoparticles. *Opt. Express*, 19(23):23386–23399, Nov. 2011.

[159] F. B. P. Niesler, N. Feth, S. Linden, and M. Wegener. Second-harmonic optical spectroscopy on split-ring-resonator arrays. *Opt. Lett.*, 36(9):1533–1535, May 2011.

[160] E. Feigenbaum and M. Orenstein. Plasmon-soliton. *Opt. Lett.*, 32(6):674–676, Mar 2007.

[161] A. Marini, D. V. Skryabin, and B. Malomed. Stable spatial plasmon solitons in a dielectric-metal-dielectric geometry with gain and loss. *Opt. Express*, 19(7):6616–6622, Mar 2011.

[162] A. R. Davoyan, I. V. Shadrivov, and Y. S. Kivshar. Self-focusing and spatial plasmon-polariton solitons. *Opt. Express*, 17(24):21732–21737, Nov 2009.

[163] Z.-j. Wu, X.-k. Hu, Z.-y. Yu, W. Hu, F. Xu, and Y.-q. Lu. Nonlinear plasmonic frequency conversion through quasiphase matching. *Phys. Rev. B*, 82(15):155107, Oct 2010.

[164] A. Fiore, V. Berger, E. Rosencher, P. Bravetti, and J. Nagle. Phase matching using an isotropic nonlinear optical material. *Nature*, 391(6666):463–466, Jan. 1998.

[165] A. D. Falco, C. Conti, and G. Assanto. Quadratic phase matching in slot waveguides. *Opt. Lett.*, 31(21):3146–3148, Nov 2006.

[166] A. S. Solntsev, A. A. Sukhorukov, D. N. Neshev, R. Iliew, R. Geiss, T. Pertsch, and Y. S. Kivshar. Cascaded third harmonic generation in lithium niobate nanowaveguides. *Appl. Phys. Lett.*, 98(23):231110, 2011.

[167] J. long Kou, Q. Wang, Z. yan Yu, F. Xu, and Y. qing Lu. Broadband and highly efficient quadratic interactions in double-slot lithium niobate waveguides through phase matching. *Opt. Lett.*, 36(13):2533–2535, Jul 2011.

[168] A. R. Davoyan, I. V. Shadrivov, and Y. S. Kivshar. Quadratic phase matching in nonlinearplasmonic nanoscale waveguides. *Opt. Express*, 17(22):20063–20068, Oct 2009.

[169] F. F. Lu, T. Li, J. Xu, Z. D. Xie, L. Li, S. N. Zhu, and Y. Y. Zhu. Surface plasmon polariton enhanced by optical parametric amplification in nonlinear hybrid waveguide. *Opt. Express*, 19(4):2858–2865, Feb 2011.

[170] Z. Ruan, G. Veronis, K. L. Vodopyanov, M. M. Fejer, and S. Fan. Enhancement of optics-to-thz conversion efficiency by metallic slot waveguides. *Opt. Express*, 17(16):13502–13515, Aug 2009.

[171] V. G. Dmitriev, G. G. Gurzadyan, and D. N. Nikogosyan. *Handbook of Nonlinear Optical Crystals.* Springer; 3rd edition, 1999.

[172] S. B. Hasan, C. Rockstuhl, T. Pertsch, and F. Lederer. Second-order nonlinear frequency conversion processes in plasmonic slot waveguides. *J. Opt. Soc. Am. B*, 29(7):1606–1611, Jul 2012.

[173] J. Zhang, E. Cassan, D. Gao, and X. Zhang. Highly efficient phase-matched second harmonic generation using an asymmetric plasmonic slot waveguide configuration in hybrid polymer-silicon photonics. *Opt. Express*, 21(12):14876–14887, Jun 2013.

Acknowledgments

It is quite an impossible task to truly acknowledge in a few scattered thoughts all those individuals who have invaluably contributed towards the completion of this thesis in one way or the other. The principal note naturally goes to Prof. Dr. Falk Lederer and Prof. Dr. Carsten Rockstuhl for accommodating me in the group and providing a wonderful academic and social environment to work in. Thanks to both of them for all the guidance, encouragement, and patience with me while I took my time toiling with the simplest of problems. In particular, I would like to mention the role of Carsten for his meticulous help in converting my amorphous thoughts into a crystalline manuscript which could be appreciable to readers.

Among scientific colleagues, it would actually become a very long list given how frequently I have enjoyed support from everyone of them. To begin with, I would like to mention Christoph Menzel, Stephan Fahr and Stefan Mühleg - the people with whom I fortunately got to share my office at the very beginning. Thanks to all of them for their priceless support, jokes and discussions despite the fact that I never joined their fellowship! I can not think of a better way to have commenced my work in the group.

Next I would like to pay my gratitude to Robert Filter for fruitful collaborations, stimulating discussions, translations, and, above all, being my partner in grumbling pessimistically about anything under the sun. The social landscape would have been radically different without him.

Special mention is due to Mohamed Farhat for filling up my solitude and making sure that I did not turn anti-social during the two years we shared together. I shall fondly cherish the memories of our trips together to Erfurt and Rostock, the field-day that we could not join, Saturday visits to Mensa and all the discussions we used to have about the future prospects of our professional and personal lives!

I also need to acknowledge Rasoul Alaee for always bringing his unending optimism to work and wonderful discussions at lunch. In the same vein, thanks to Samuel Wiesendanger for the wonderful company he provided at work. In particular, his ever-readiness to help me whenever I would be loosing my way with Deutsch was invaluable.

Apart from scientific colleagues, I can not go without mentioning the support of Szilvia Mammel. It is impossible to thank her enough for always going way out of her way to help me with the most menial of problems. My stay in Jena could never have been so pleasant and smooth without her generous support.

I would also gratefully acknowledge the careful reading and evaluation of this thesis by all referees.

Lastly, this section will remain incomplete without a note of heart-felt appreciation to my parents, wife, sisters and friends. It is incredible how patiently they bore year after year in hope that it would all end soon enough. I am truly blessed to share my life with them.

Short Curriculum Vitae

Personal Data

Name	Shakeeb Bin Hasan
Data of Birth	August 4, 1983
Place of Birth	Karachi, Pakistan

Academic Career

02/2013	Submitted doctoral thesis entitled "Waveguide approach to plasmonic antennas"
10/2009 - present	Scientic assistant and PhD candidate at the IFTO at Friedrich-Schiller-Universität Jena, Germany

Lectures Conducted

Summer term 2013	Nonlinear optics (1 SWS)
Summer term 2013	Waveguide thoery (1 SWS)
Winter term 2013	Fundamentals of modern optics (2 SWS)

Education

07/2006	Bachelor of Science in Engineering Sciences from G.I.K. Institute, Pakistan
09/2009	Master of Science in Applied Physics from Delft University of Technology, The Netherlands
09/2009	Master in Automatics and Robotics from Warsaw University of Technology, Poland

Ehrenwörtliche Erklärung

Hiermit erkläre ich ehrenwörtlich, dass ich die vorliegende Arbeit selbständig, ohne unzulässige Hilfe Dritter und ohne Benutzung anderer als der angegebenen Hilfsmittel und Literatur angefertigt habe. Die aus anderen Quellen direkt oder indirekt übernommenen Daten und Konzepte sind unter Angabe der Quelle gekennzeichnet.

Weitere Personen waren an der inhaltlich-materiellen Erstellung der vorliegenden Arbeit nicht beteiligt. Insbesondere habe ich hierfür nicht die entgeltliche Hilfe von Vermittlungs bzw. Beratungsdiensten (Promotionsberater oder andere Personen) in Anspruch genommen.

Niemand hat von mir unmittelbar oder mittelbar geldwerte Leistungen für Arbeiten erhalten, die im Zusammenhang mit dem Inhalt der vorgelegten Dissertation stehen.

Die Arbeit wurde bisher weder im In- noch im Ausland in gleicher oder ähnlicher Form einer anderen Prüfungsbehörde vorgelegt.

Die geltende Promotionsordnung der Physikalisch-Astronomischen Fakultät ist mir bekannt.

Ich versichere ehrenwörtlich, dass ich nach bestem Wissen die reine Wahrheit gesagt und nichts verschwiegen habe.

Jena, Unterschrift